UNIVERSITAT POLITÈCNICA DE VALÈNCIA

DEPARTAMENT DE COMUNICACIONS

Advanced Arrayed Waveguide Gratings: Models, design strategies and experimental demonstration

Ph.D. THESIS

by
Bernardo Andrés Gargallo Jaquotot

Ph.D. Supervisor:
Dr. Pascual Muñoz Muñoz

Valencia, July 2016

UNIVERSITAT POLITÈCNICA DE VALÈNCIA

DEPARTAMENT DE COMUNICACIONS

Advanced Arrayed Waveguide Gratings: Models, design strategies and experimental demonstration

Bernardo Andrés Gargallo Jaquotot
Optical and Quantum Communications Group
iTEAM Research Institute
Universitat Politècnica de València
Camí de Vera s/n, 46022 Valencia, SPAIN
bergarja@iteam.upv.es

Ph.D. Supervisor:
Dr. Pascual Muñoz Muñoz

Valencia, July 2016

A mi familia...

The important thing is not to stop questioning.
Curiosity has its own reason for existing.
Albert Einstein

Agradecimientos

Una de las partes más difíciles de escribir de esta tesis ha sido la de agradecimientos y es que ¡tengo tanta gente a la que agradecer tanto!

En primer lugar al director de esta tesis, Dr. Pascual Muñoz, por introducirme en el mundo de las comunicaciones ópticas cuando no tenía claro hacia dónde enfocar mi carrera. Él ha sido mi director en el Proyecto Final de Carrera, en el Trabajo Final de Máster y, finalmente, en esta tesis. En cualquier caso, debo agradecerle no sólo por la parte laboral, que ha sido inmejorable, sino además por la parte personal, ya que después de tantos años y vivencias he pasado a considerarlo un amigo.

También debo agradecer a toda la gente del Grupo de Comunicaciones Ópticas y Cuánticas del iTEAM en el que se ha realizado esta tesis, y en especial al Dr. Daniel Pastor por su inestimable ayuda con el sistema de medida de OFDR.

En cuanto a mis compañeros, agradecerles a todos el tiempo que hemos pasado juntos compartiendo fatigas pero también muy buenos momentos, especialmente a la hora de la comida. Mención especial a David Doménech, el cual ha tenido la infinita paciencia de ser el "padre" que nos ha instruido a todos en el laboratorio midiendo chips, y también a Luís, por las largas horas de laboratorio que hemos pasado juntos en los últimos tiempos y en las que hemos pasado muy buenos ratos. Es necesario dar las gracias al grupo que forman Rocío, Francisco y Manuel, el cual ha conseguido que cada día de trabajo fuera una experiencia única. Algún día conseguiremos nuestro sueño de ver la gran barrera de coral. Finalmente, debo agradecer a Alejandro, compañero durante la carrera y amigo siempre, las terapias con cerveza de por medio.

Agradecer también a toda la gente del Photonic Integration group de la Technische Universiteit Eindhoven (TUe) donde realicé mi estancia, y en especial al Dr. Xaveer Leijtens por hacer que me sintiera como en casa y enseñarme cómo trabaja un gran grupo como el suyo. Dicha estancia fue una de las mejores experiencias de mi vida, de la cual volví con un grupo de amigos para siempre. Gracias a la

gente de Marconilaan 57 (Dani, Sergio, Mikel, Ander, Agustín y Joel) no hay ni una sola de las largas noches holandesas de la que no se tenga una anécdota que contar. Sois los mejores.

Finalmente agradecer a mi padre, a mi madre y a mis hermanos el haber estado ahí no sólo durante los cuatro años de esta tesis sino durante toda mi vida. Han sido un pilar fundamental siempre. También a Marta, por haber estado a mi lado (cuando las guardias lo permitían) y por haber conseguido que me olvidara de los problemas y siempre viera el lado bueno de las cosas. Y, cómo no, al pequeño José, ya que parte de esta tesis se ha escrito (o por lo menos se intentó) con él en brazos.

Y a ti que al final ves que, aunque el camino ha sido difícil, lo he conseguido.

A todos vosotros, ¡gracias!

Abstract

The present PhD thesis deals on the model, design and experimental demonstration of Arrayed Waveguide Grating (AWG) with advanced features. Firstly, building upon existing AWG formulations, design equations are provided, libraries developed and all this is experimentally validated with devices in Indium Phosphide (InP) and Silicon-on-insulator (SOI) technologies. Next, a model and experimental validation is reported for an Interleave-Chirped Arrayed Waveguide Grating (IC-AWG), which is able to process optical signals as WDM demultiplexer, polarization splitter and phase diversity component all in a single device. This device was fabricated and tested in InP technology. The second innovative AWG demonstrated in this thesis, a Reflective type (R-AWG), whose layout allows for tailoring the pass-band shape and to change the spectral resolution. A demonstration of design and fabrication for this device is provided in SOI technology. The last AWG with innovative concepts is one driven by Surface Acoustic Waves (AWG-SAW), where the spectral channels can be tuned by means of acousto-optic effect. The device was fabricated in Aluminium Gallium Arsenide (AlGaAs) technology, and measurements are provided to validate the concept and design flow. In parallel this thesis has resulted in the development of different AWG layouts for a wide number of (generic) technologies and foundries, coded into design libraries, of use in a de-facto standard software employed for the design of photonic integrated circuits. These design libraries have been licensed to the UPV spin-off company VLC Photonics S.L.

Resumen

La presente tesis se ha centrado en el modelado, diseño y demostración experimental del dispositivo Arrayed Waveguide Grating (AWG) con funcionalidades avanzadas. Primero, usando la formulación existente sobre AWGs se aportan ecuaciones y librerías de diseño, y se validan experimentalmente por medio de dispositivos fabricados en tecnologías de Indium Phosphide (InP) y Silicon-on-insulator (SOI). Después, se reporta un modelo y demostración experimental para un Interleave-Chirped Arrayed Waveguide Grating (IC-AWG), el cual es capaz de procesar señales ópticas como demultiplexor WDM, divisor de polarización y componente de diversidad de fase en un único dispositivo. Este dispositivo fue fabricado y probado en tecnología de InP. El segundo AWG innovador demostrado en esta tesis es de tipo Reflectante (R-AWG), cuyo diseño permite modificar la forma espectral del canal y cambiar su resolución espectral, incluyendo una demostración de diseño y fabricación de este dispositivo en tecnología de SOI. El último AWG que incluye conceptos innovadores es uno sintonizable por Acoustic Waves (AWG-SAW), donde los canales espectrales pueden ser sintonizados por medio del efecto acusto-óptico. Dicho dispositivo fue fabricado en tecnología de Aluminium Gallium Arsenide (AlGaAs), y se han incluido medidas experimentales para validad el concepto y el flujo de diseño. En paralelo junto con esta tesis se han desarrollado diferentes diseños para el AWG en un amplio número de tecnologías (genéricas) y plataformas de fabricación, implementadas en unas librerías de diseño para uno de los softwares más utilizados para el diseño de circuitos integrados ópticos, siendo actualmente el estándar de facto. Dichas librerías de diseño han sido licenciadas a la compañía VLC Photonics S.L., spin-off de la UPV.

Resum

La present tesi ha estat centrada en el modelatge, disseny i demostració experimental del dispositiu Arrayed Waveguide Grating (AWG) amb funcionalitats avançades. Primer, usant la formulació existent sobre AWGs s'aporten equacions i llibreries de disseny, i es validen experimentalment per mitjà de dispositius fabricats en tecnologies de Indium Phosphide (InP) i Silicon-on-insulator (SOI). Després, es reporta un model i demostració experimental per a un Interleave-Chirped Arrayed Waveguide Grating (IC-AWG), el qual és capaç de processar senyals òptiques com demultiplexor WDM, divisor de polarització i component de diversitat de fase en un únic dispositiu. Aquest dispositiu va ser fabricat i provat en tecnologia de InP. El segon AWG innovador demostrat en aquesta tesi és de tipus Reflector (R-AWG), amb un disseny que permet modificar la forma espectral del canal i canviar la seua resolució espectral, incloent una demostració de disseny i fabricació d'aquest dispositiu en tecnologia de SOI. L'últim AWG que inclou conceptes innovadors és un sintonitzable per Acoustic Waves (AWG-SAW), on els canals espectrals poden ser sintonitzats per mitjà de l'efecte acusto-òptic. Aquest dispositiu va ser fabricat en tecnologia de Aluminium Gallium Arsenide (AlGaAs), i s'han inclòs mesures experimentals per validar el concepte i el flux de disseny. En paral·lel juntament amb aquesta tesi s'han desenvolupat diferents dissenys per al AWG en un ampli nombre de tecnologies (genèriques) i plataformes de fabricació, implementades en unes llibreries de disseny per a un dels programaris més utilitzats per al disseny de circuits integrats òptics, sent actualment l'estàndard de facto. Aquestes llibreries de disseny han estat llicenciades a la companyia VLC Photonics S.L., spin-off de la UPV.

Contents

List of Figures

List of Tables

Chapter 1
Introduction

The word *photonics* is derived from the Greek word φωτὸς (phōtos), which means *light*. In the broad sense of the word, photonics is the discipline dealing with the applications of light over the whole spectrum, from ultraviolet, over visible through the near, mid and far infrared (0.4-12 μm in wavelength). Photonics exploits the properties of photons, and it addresses the generation, emission, transmission, modulation, signal processing, switching, amplification and detection/sensing of light to obtain a functionality, being the most typical applications those related with communications.

Since the advent of the optical fiber in the 60s, replacing the traditional copper wires due to the low transmission losses and high capacity, a lot of effort has been put in the development of components and systems taking advantage of the electromagnetic nature of light. For this reason, photonic integration is envised as very promising since it allows combining multiple functionalities into a single optical chip. Traditionally the development of devices in photonic integration followed a vertical aggregation model from a single device manufacturer, where a custom process is defined for producing a single particular device (i.e. a process for a modulator, not suited to make a laser). However, following the evolution path of the semiconductor industry in the United States, making the fabrication processes generic allows vertical specialization through the value chain, by several specialized partners at different stages of an optical system development. In photonics, the seed for generic integration appeared in Europe by 2007 [1]. Subsequent technical and organizational developments lead to the current generic foundry processes and have been mainly driven by Europe since 2004, heavily subsidized by the European Commission, followed by the US in 2010. Generic processes, which will be explained in more detail in Section 1.1, are openly available to research on Photonic Integrated Circuits (PICs) for multiple applications [2].

PICs enable myriad of applications, owing to small size and stability, compared to the assembly of systems with discrete optical components [3]. These applications are in general the manipulation of photonic and/or electronic signals

by means of other photonic and/or electronic control signals. Furthermore, PICs are of great importance in market and job opportunities as identified by several reports, since they allow to bring miniaturized electronic+photonic equipment in various markets like healthcare (endoscopes), safety (lightweight sensor readout systems in airplanes, cars), communication (energy reduction and interconnects) and personalized wearable equipment.

For all these applications, one of the most important functionalities when talking about optical devices is wavelength filtering. There are several well-known devices in the literature to obtain such functionality, as for example the Mach-Zehnder Interferometer (MZI) [4], the Ring Resonator [5], the Echelle Grating [6] or the Arrayed Waveguide Grating (AWG) [7]. This thesis is focused on the latter device, since it has been widely used since its invention at the end of the 90s. However, its versatility and the wide range of possibilities that it provides, make this device perfect to exploit it in new and emerging applications as can be seen in the high number of papers still published more than 25 years after its invention. Some examples of applications using AWGs as key blocks are wavelength routing [8], spectrometry [9,10], optical coherence tomography (OCT) systems [11] or Raman spectroscopy systems [12].

1.1 Fabrication technologies

Multiple material technologies are available to fabricate photonic integrated circuits (PICs), each of them suitable for one or more applications, as for example Lithium-Niobate [13], Silica [14], Indium Phosphide (InP) [15], Silicon Nitride (SiNx) [16], Silicon-on-insulator (SOI) [17] or Silicon-Germanium [18].

The choice of a technology depends on many aspects. One of the most determining factors is the wavelength range of the application pursued. For example, for telecom applications wavelengths are in the range of 900-1700 nm, where optical fibers exhibit moderate and low transmission losses. Conversely, for biological sensing applications it is usual to work in the visible wavelength range (around 400-700 nm), where the light does not harm matter through their interaction. Figure 1.1 shows the most representative integration technologies and materials, and their corresponding working wavelength range.

At the moment of writing this thesis, three different platforms have arised as the most demanded by the users due to a trade-off between advantages and cost, resulting in stable fabrication processes and also offering multi-project wafer (MPW) runs.

Silicon-on-insulator technology is a high contrast technology, where the optical field is strongly confined in the waveguide [19]. For this reason, the optical waveguides can be designed to have a narrow core and small bending radius, resulting in very small structures. It is also compatible with electronics, since the fabrication processes and materials in SOI are approximately the same. As a drawbacks, the high index contrast in the waveguides results in phase errors due to the sidewall roughness and the strong confinement. Moreover, no active (i.e. electrically

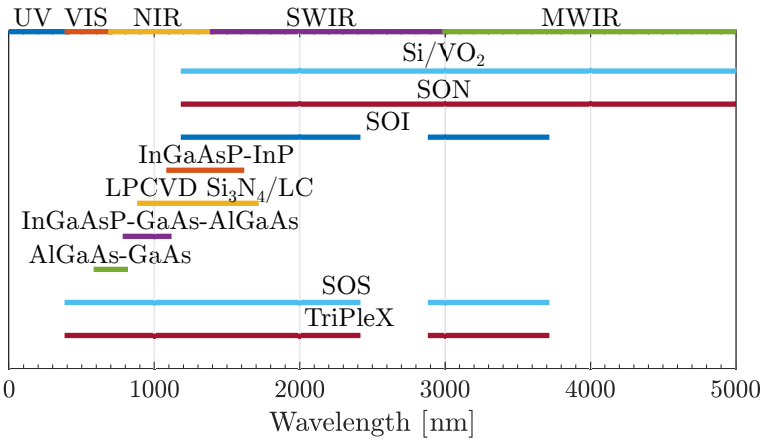

Figure 1.1: Comparison between materials and technologies in terms of wavelength and different spectral bands. Abbreviations: UV ultraviolet, VIS visible, NIR near-infrared, SWIR short-wavelength infrared, MWIR mid-wavelength infrared, Si/VO_2 vanadium dioxide on silicon, SON silicon-on-nitride, SOI silicon-on-insulator, InGaAsP indium gallium arsenide phosphide, InP indium phosphide, LPCVD Si_3N_4 low pressure chemical vapor deposition silicon nitride, GaAs gallium arsenide, AlGaAs aluminum gallium arsenide, SOS silicon-on-sapphire.

pumped efficient light emitters) devices can be fabricated in Si materials, and the use of modulators and photodetectors implies additional fabrication steps.

Indium Phosphide (InP) technology offers active devices as lasers, amplifiers or photodetectors for the telecom band [20]. Because it is a medium index contrast technology, the bending radius that can be obtained is around 20 times higher than for SOI technology, which gives a vision about the lower integration density that can be achieved with this technology. However, it is the only technology capable of monolithic integration of optical amplification and passive photonic components.

Finally, Silicon Nitride (SiNx) technology can be used in a very wide wavelength range (from 500 nm up to 3500 nm) [21, 22]. This characteristic permits its application not only in the communications bands, but also in the visible and mid-infrared bands. For this reason, it is very interesting for fields like biosensing or spectrometry. Moreover, this technology offers very low propagation losses. As SOI technology, its main problem is the no possibility of integrate monolithically active devices as lasers or amplifiers.

1.2 Generic integration technologies

Although photonic integration offers several advantages when comparing with electronics, the cost of the fabrication facilities are unaffordable for research entities or small businesses. Hence, the access would be restricted to a very small part

of the possible users. For this reason, generic integration platforms have been shown as the solution for research and development, as they separate manufacturing from design. These platforms provide a low cost access to a small volume production and offer a generic integration technology where the fabrication process is standardized.

Generic integration technologies offer a fabrication process that is fixed and standardized, thus offering reproducibility in a process that can be used for many designs and applications. Generic fabrication platforms also offer a set of predefined components (building blocks, BBs) that have been fabricated and tested previously in the platform, and which information is provided to the users by means of statistical information collected through the course of runs along time. Besides the fundamental straight and bent waveguides, generic integration platforms usually provide with more complex BBs as for example multi-mode interference (MMI) couplers or modulators. The group of BBs offered by each platform together with the information about the fabrication process and the design rules for designers forms what is called Process Design Kit (PDK). With this PDK, one user can obtain high functionalities interconnecting the different BBs without taking care of all the physics underlying each component.

To reduce the cost, the access to these platforms is usually through multi-project wafer (MPW) runs, where the cost of the total fabrication process is shared between all the users in a wafer. To illustrate the concept of a MPW run, Fig. 1.2 shows one wafer map planned following this concept. The wafer is divided in 9 (identical) dies, called CX where X is a number, and 4 test dies (called TX). Then, each different die is divided into sub-dies, obtaining two different sizes: MX and LX. Finally, each user can access to one or more of these sub-dies, obtaining 9 copies of their design.

At the moment of writing this thesis, five different brokers offer access to MPW runs in the three main technologies: europractice-IC [23], IME [24], JePPIX [25], VLC Photonics [26] and VTT [27]. A summary of the current different platforms offering MPW runs and the different building blocks available is shown in Fig. 1.3. However, the eco-system has been and is rapidly evolving, so new brokers and MPW fabs are expected in the coming years.

On the other hand, in a dedicated run one or more designs from one user are replicated over the full wafer(s). Then, the cost of the fabrication process is assumed by the (single) user, making it unaffordable for prototyping or research. However, this type of access to the platforms results in an elevated number of dies with the same design, which is desired for volume manufacturing.

1.3 Generic design libraries

The aforementioned set of BBs offered by each platform is usually very similar in functionality. However, even for the same technology material, devices with the same functionality will be different between fabrication platforms, as the fabrication process is different for each of them. Owing to this reason, it is very important

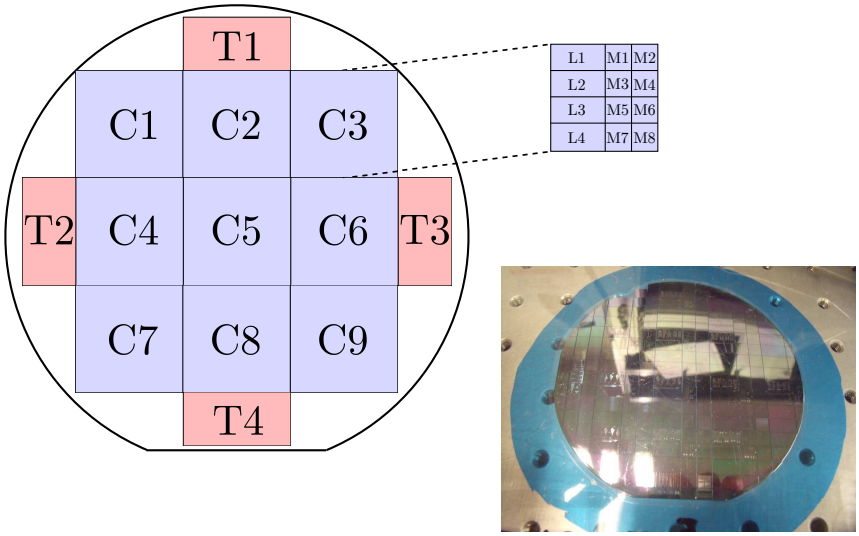

Figure 1.2: Schematic of a MPW run. Different fabrication dies are named CX and test dies with TX. The inset in the right upper part shows how the different dies are divided into sub-dies, obtaining two different sizes (MX and LX). The inset in the right bottom part shows one of the fabricated wafers.

to have a set of BBs that can be used for the different generic fabrication platforms, and these BBs will be adapted taking into account the technology and platform where they will be designed and fabricated, resulting in logic blocks (LBs).

Moreover, building blocks for high level functionalities are not usually available in the PDK, and it is the task of the designer to develope the required design libraries. In any case, the designer does not necessarily have to start from scratch when designing new BBs or LBs, because hierarchical methods can be used to generate design libraries for advance functionalities using the available BBs. As an example, a basic 2x2 MMI which consists of a rectangular body, and 4 access waveguides, can be seen as 5 straight waveguides of different widths. Therefore, by properly combining different instances of fundamental BBs (waveguides of different widths in this case) a new BB can be defined (the MMI) in a hierarchical way. This new BB in turn, can be part of a more complex BB, such as a MZI, combining two MMIs and several straight and bent waveguides, resulting into a new BB composed once more by aggregation of some other.

For a PIC designer, to have a set of different BBs for different technologies is desired, including high level functionalities as for example filtering. For this reason, one of the purposes of this thesis will be to develop and test the AWG design libraries for every technology/platform.

Broker	europractice-IC			IME	VTT	JePPiX				VLC Photonics
Foundry	IMEC	CEA-LETI	IHP	IME	VTT	HHI	Oclaro	SmartPhotonics	LioniX	IMB-CNM
Technology	SOI	SOI	SOI	SOI	Thick SOI	InP	InP	InP	SiNx	SiNx
Location	Belgium	France	Germany	Singapore	Finland	Germany	United Kingdom	Netherlands	Netherlands	Spain
Features										
Wide wavelength range										
Low losses										
Coupling to fiber										
Electro-optic effect										
Thermo-optic effect										
Electro-absortion effect										
Footprint										
Compatible with electronics										
Building blocks										
Waveguide										
MMI coupler										
Grating coupler										
Electro-optic modulator										
Thermo-optic modulator										
Semiconductor optical amplifier										
Distributted Bragg reflector										
Laser										
Photo-detector										
Packaging										

Figure 1.3: Generic foundries providing multi-project wafer (MPW) shared access. Color code for features: Green = Advantageous, Grey = Disadvantageous. Color code for building blocks: Green = Available/Possible, Grey = Not Available/Not Possible.

1.4 Objectives

This thesis has three fundamental objectives:

1. To develop the theory describing the operation and the procedure to design AWG-based devices with different functionalities and layouts:
   1.1. Interleave-chirped AWG (IC-AWG).
   1.2. Reflective AWG (R-AWG).
   1.3. AWG driven by surface acoustic waves (AWG-SAW).
2. To develop:
   2.1. the libraries required to design the aforementioned devices.
   2.2. the design procedures and layout routines for the main MPW integration technologies.
3. To fabricate and demonstrate experimentally the devices as a mean to validate the developed theory and check the design libraries.

1.5 Thesis outline

This thesis is structured in the following chapters:

- **Chapter 2** provides the framework and the theoretical model for regular AWGs demonstrated in this thesis. This theoretical model will be the base for the development of the design libraries, which can be used in multiple technologies. Examples of AWGs designed and fabricated using these libraries in two of the most important technologies (InP and SOI) are provided.
- **Chapter 3** includes the fundamental theory describing the Interleave-Chirped AWG (IC-AWG) building upon the previous chapter. The IC-AWG device can be found in the literature acting as a BB in coherent receivers, but no theory explaining its functionality or design rules providing the required equations for its development were published before this thesis. In this chapter an example of design and fabrication for InP technology is also reported as validation of the theory, design rules and libraries.
- **Chapter 4** discusses the Reflective AWG (R-AWG). This particular AWG configuration is usually employed to reduce the footprint of the device, obtaining a more compact device. For this purpose, the AWG is cut in two halves and a reflector is used to terminate each arrayed waveguide independently. However in this thesis we explore novel aspects such as the modification of the output pass-band shape. Using a combination of Sagnac loops

and Mach-Zehnder Interferometers as reflectors, it is possible to introduce a phase shift and tune the reflected amplitude. The adapted theory including in each arm a phase shifter and a tunable coupler is provided in this chapter. As validation, R-AWGs in SOI technology using reflectors were designed and experimentally demonstrated.

- **Chapter 5** provides a new configuration using an AWG driven by surface acoustic waves (AWG-SAW). This device was fabricated in AlGaAs technology and enables to tune dynamically the output channels in the different output waveguides.
- Finally, in **Chapter 6** the conclusions and considerations for future work are presented.

Chapter 2
Arrayed waveguide grating (AWG)

The general objective of this chapter is to demonstrate the regular Arrayed Waveguide Grating (AWG) in different manufacturing technologies. The supporting theory, design procedure and layout are reported. The chapter is structured as follows. The background and motivation are provided in Section 2.1. Next, the operation of the AWG is summarized in Section 2.2.

In this chapter, AWGs were fabricated in InP and SOI, and are reported in Sections 2.3 and 2.4. The design and experimental outcomes from these activities in these two most widespread integration technologies are incorporated into an AWG design library. This library of regular AWGs will be the basis upon which the advanced AWG devices of next chapters will be built.

Finally, the chapter conclusions are presented in Section 2.5.

2.1 Background and motivation

Wavelength multi/demultiplexers are key components in optical communication networks. During the last two decades, they have been subject of intense research, since they are central devices for wavelength-division multiplexing (WDM) systems [28]. The deployment of WDM systems, requires large number of components, subject to very demanding specifications, among them reproducibility and stable operation. Naturally, most of these components are built using photonic integration.

Among the different multi/demultiplexer implementations, the Arrayed Waveguide Grating (AWG) is one accomplishing all these requirements [7, 29]. This is a very well known mux/demux integrated optics device, which can be manufactured in almost all the relevant material platforms as Silica [30], InP [31], SOI [32] or SiNx [16].

The AWG is composed of several sets of waveguides and couplers [7, 33]. In the most common shape, the couplers are slab couplers, also termed as free prop-

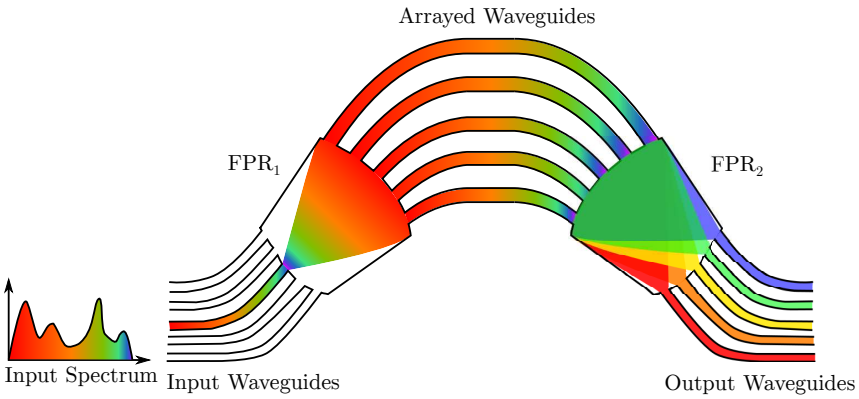

Figure 2.1: Schematic for the regular AWG, where different wavelengths are represented by different colors. FPR stands for free propagation region.

agation regions, and they are connected by a group of waveguides called arrayed waveguides. The light fed into the first coupler reaches the set of arrayed waveguides. The length of consecutive waveguides in the array is set in such a way that the light is guided and fed to the second coupler having a phase shift that depends linearly on the optical frequency. Hence, the combined effect of this frequency linear phase shift, and the second coupler, is the spatial separation of the different optical frequencies (or wavelengths) at the end of the coupler [7, 34].

Although the AWG is a very well-known device for wavelength multi/demultiplexing operation [7], new applications are emerging more than 25 years after its invention. For example, it has been used as a wavelength router [8] obtaining that with a N×N, AWG one wavelength can be routed from any input port to any output port. One of the most important applications is spectrometry, where it can provide high spectral resolution and compactness [9, 10]. Thus, it has been used as the key part for optical coherence tomography (OCT) systems [11] and Raman spectroscopy systems [12]. On the other hand, it is possible to apply different phase shifts in the arrayed waveguides to obtain new functionalities, as for example the use as coherent receiver [15].

Due to its versatility not only as a multi/demultiplexer device, but also as central element in other applications, the AWG has been chosen to be studied in this thesis and included as the first step to develop more complex functionalities.

2.2 AWG operation description

In this section, the Arrayed Waveguide Grating (AWG) operation will be described briefly for completeness, using Fig. 2.1 as a reference, where the schematic for the AWG in its most simple form has been represented. The AWG is composed by a group of input waveguides used to introduce the light into the device.

Consider first the field in an input waveguide, placed at the center input side of the slab coupler. The field in this waveguide can be approximated by a power normalized Gaussian function [34]:

$$b_i\left(x_0\right) = \sqrt[4]{\frac{2}{\pi\omega_i^2}} e^{-\left(\frac{x_0}{\omega_i}\right)^2} \tag{2.1}$$

with ω_i is the mode field radius and x_0 the spatial coordinate at the input plane. When the field from this waveguide arrives to the first slab coupler (FPR_1), it is no longer confined and it will be radiated to the side where the AWs are placed. The diffracted light spatial distribution can be obtained using the spatial Fourier transform of the input profile, using the paraxial approximation [35]:

$$B_i\left(x_1\right) = \mathcal{F}\left\{b_i\left(x_0\right)\right\}|_{u=\frac{x_1}{\alpha}} = \sqrt[4]{2\pi\frac{\omega_i^2}{\alpha^2}} e^{-\left(\pi\omega_i\left(\frac{x_1}{\alpha}\right)\right)^2} \tag{2.2}$$

being u the spatial frequency domain variable of the Fourier transform, x_1 is the spatial coordinate at the AWs plane and α is the equivalent to the wavelength focal length product in Fourier optics propagation. This α will be expressed as $\alpha = cL_f/(n_s\nu)$, with L_f being the slab length, n_s the effective index of the slab coupler mode, ν the frequency and c the speed of light in vacuum.

The model makes use of the analytical approximation of Eq. (2.1) for the waveguide mode. However, in the numerical implementation of the model, any field may be employed, as for instance the results from a mode solver. Moreover, it can be used for any polarization since only the field profile and the effective index will be required to simulate the total response.

Then, the field distribution calculated as the summation of the field coupled in each one of the N AWs placed at the x_1 plane will be [34]:

$$f_1\left(x_1\right) = \sqrt[4]{2\pi\omega_g^2}\left[\prod\left(\frac{x_1}{Nd_\omega}\right) B_i\left(x_1\right) \sum_{r=-\infty}^{+\infty} \delta\left(x_1 - rd_\omega\right)\right] \otimes b_g\left(x_1\right) \tag{2.3}$$

where r is the AW number, d_ω is the spacing, ω_g is the mode field radius, $b_g\left(x\right)$ is the field profile of the AWs, $\otimes$ the convolution and $\prod\left(x_1/Nd_\omega\right)$ being a truncation function.

Then, the length of the waveguide number r will be given by $l_r = l_0 + \Delta l\left(r + N/2\right)$, where l_0 is the base length of the shortest waveguide in the array. As is previously discussed, the incremental length between AWs will be set to an integer multiple m of times 2π when using the central wavelength λ_0, resulting in $\Delta l = m\lambda_0/n_c$ where n_c is the effective index from the AWs. Thus, the phase shift due to the waveguide will be $\Delta\phi_r = \beta l_r = 2\pi n_c\nu l_r/c$, where β is the propagation constant of the mode in the waveguide. The field from the AWs at the plane x_2, that is the beginning of the second slab coupler (FPR_2) will be:

$$f_2(x_2,\nu)=\sqrt[4]{2\pi\omega_g^2}\left[\prod\left(\frac{x_2}{Nd_\omega}\right)B_i(x_2)\,\phi(x_2,\nu)\sum_{r=-\infty}^{+\infty}\delta(x_2-rd_\omega)\right]\otimes b_g(x_2) \tag{2.4}$$

where the phase term $\phi(x_2,\nu)$ is given by:

$$\phi(x_2,\nu)=\psi(\nu)\,e^{-j2\pi m\frac{\nu}{\nu_0}\frac{x_2}{d_\omega}} \tag{2.5}$$

$$\psi(\nu)=e^{-j2\pi\nu\left(\frac{n_c l_0}{c}+\frac{mN}{2\nu_0}\right)} \tag{2.6}$$

Finally, to obtain the field at the plane x_3 the spatial Fourier transform will be used to the field coming from each AW. This result into:

$$f_3(x_3,\nu)=\sqrt[4]{2\pi\omega_g^2}B_g(x_3)\left[\operatorname{sinc}\left(Nd_\omega\frac{x_3}{\alpha}\right)\otimes b_i(x_3)\otimes\Phi(x_3,\nu)\otimes\Delta_\omega(x_3)\right] \tag{2.7}$$

with,

$$\Phi(x_3)=\mathcal{F}\left\{\phi(x_2,\nu)\right\}|_{u=\frac{x_3}{\alpha}}=\psi_k(\nu)\,\delta\left(x_3+\frac{\alpha m}{d_\omega\nu_0}\nu\right) \tag{2.8}$$

$$\Delta_\omega(x_3)=\mathcal{F}\left\{\delta(x_2-rd_\omega)\right\}|_{u=\frac{x_3}{\alpha}}=\sum_{r=-\infty}^{+\infty}\delta\left(x_3-r\frac{\alpha}{d_\omega}\right) \tag{2.9}$$

which after some manipulation results in:

$$f_3(x_3,\nu)=\sqrt[4]{2\pi\frac{\omega_g^2}{\alpha^2}}B_g(x_3)\,\psi(\nu)\sum_{r=-\infty}^{+\infty}f_M\left(x_3-r\frac{\alpha}{d_\omega}+m\frac{\alpha}{d_\omega}\right) \tag{2.10}$$

with,

$$f_M(x_3)=\operatorname{sinc}\left(Nd_\omega\frac{x_3}{\alpha}\right)\otimes b_i(x_3) \tag{2.11}$$

The argument of f_M in Eq. (2.10) shows that the field at the output of the second FPR has its focusing point positions determined by the grating order m. Position x_3 and wavelength $\lambda=c/\nu$ are related through the frequency spatial dispersion parameter (FSDP) given by:

$$\gamma=\frac{cMd_\omega}{n_c\Delta l'\alpha}=\frac{\nu_0 d_\omega}{\alpha m} \tag{2.12}$$

2.2.1 Field at the output waveguides

At the output waveguides, the field can be obtained through the following overlap integral:

$$t_{0,q}(\nu) = \int_{-\infty}^{+\infty} f_3(x_3, \nu)\, b_0(x_3 - qd_0)\, \partial x_3 \tag{2.13}$$

where b_0 is the fundamental mode profile at the output waveguide (OW), q is the OW number and d_0 is the OW spacing.

2.2.2 Arbitrary IW position

All this formulation can be easily extended to the case with more than one input waveguide (IW), not only for the case with one input placed at the central position of the first FPR. The field at the IW can be expressed then as

$$b_{i,p}(x_0) = \sqrt[4]{\frac{2}{\pi\omega_i^2}} e^{-\left(\frac{x_0 - pd_i}{\omega_i}\right)^2} = b_{i,p}(x_0 - pd_i) \tag{2.14}$$

where p is the IW number and d_i is the IW spacing. At the output plane the field will be

$$f_3(x_3, \nu) = \sqrt[4]{2\pi\frac{\omega_g^2}{\alpha^2}} B_g(x_3)\, \psi(\nu) \sum_{r=-\infty}^{+\infty} f_M\left(x_3 - r\frac{\alpha}{d_\omega} + m\frac{\alpha}{d_\omega} + pd_i\right) \tag{2.15}$$

and the field in the output waveguides is

$$t_{p,q}(\nu) = \int_{-\infty}^{+\infty} f_{3,p}(x_3, \nu)\, b_0(x_3 - qd_0)\, \partial x_3 \tag{2.16}$$

As a summary, if one or more wavelengths are introduced using one input waveguide, these different wavelengths will be separated to different output waveguides, obtaining a multi/demultiplexer functionality. A thorough development of this model can be found in [36].

2.3 Indium Phosphide AWGs

2.3.1 Overview

The AWGs in this section were designed for and fabbed in the Indium Phosphide technology of the Fraunhofer Heinrich Hertz Institute in Berlin, Germany. The fabrication of the devices was done using standard 3-inch semi-insulating InP wafers with a thickness of 600 μm. Then, three different dry-etching processes were used to generate the three different cross-sections available (Fig. 2.2): E200, E600 and E1700, with etchings of 0.2, 0.6 and 1.7 μm, respectively [37].

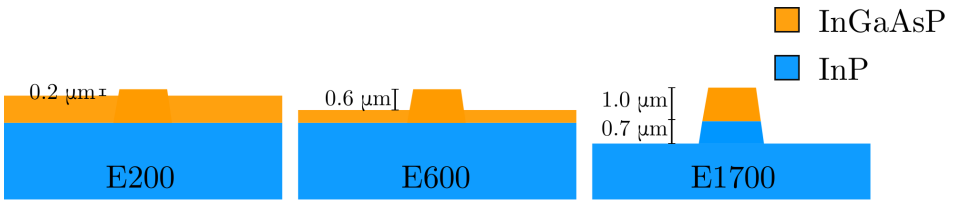

Figure 2.2: Available cross-sections in the HHI platform.

Although the less etching level (E200) implies lower propagation losses, the bending radius has to be very large (>1500 μm) to reduce the losses due to the low confinement in the waveguide. For this reason, all the waveguide routing along the chip was done using the cross-section E1700, where the radius can be smaller (>100 μm for polarization independence).

The generic integration platform at HHI also offers different building blocks in the MPW runs, as for example passive devices: straight waveguides, MMI couplers, directional couplers, polarization splitters or Spot Size Converters (SSCs). It also provides with active elements, such as Distributed Feedback (DFB) lasers, Distributed Bragg Reflector (DBR) lasers, Semiconductor Optical Amplifiers (SOAs), tunable gratings, photodiodes or modulators.

2.3.2 Design, fabrication and characterization

Two chips containing AWGs with different parameters were designed and fabricated. The first chip contained regular AWGs, with different channel spacing. The second chip incorporated MMIs at the input of the AWG, designed to broaden the channel spectral response [38].

Regular AWGs chip

The two devices in this chip were designed to include deep and shallow waveguides in the arms (double-etched design [39]). They correspond to the E200 and E1700 cross-sections shown in Fig 2.2. Doubled-etched AWG layouts employ shallowly etched waveguides to interface the slab couplers, and deeply etched waveguides to connect one slab coupler to the other. The former allows for reducing the insertion losses, while the latter allows for sharper bends and smaller footprint [39]. A width of 2 μm was employed both for the shallow and deeply etched waveguides, to ensure only the propagation of the fundamental mode. The bends in the array, performed with deeply etched waveguides, had a radius of 250 μm. The reason of using this large bend radius is to reduce the losses and avoid possible polarization rotation [40]. The latter phenomena will be explained in more detail in Chapter 3. For both AWGs, the selected central wavelength was 1.55 μm, the gap between arrayed waveguides was 1.2 μm, the number of input/output waveguides was 5, and the focal length L_f was 329.8 μm. For the AWG with a channel spacing of 100 GHz, the free spectral range was 8 nm, the grating order m was 174 and

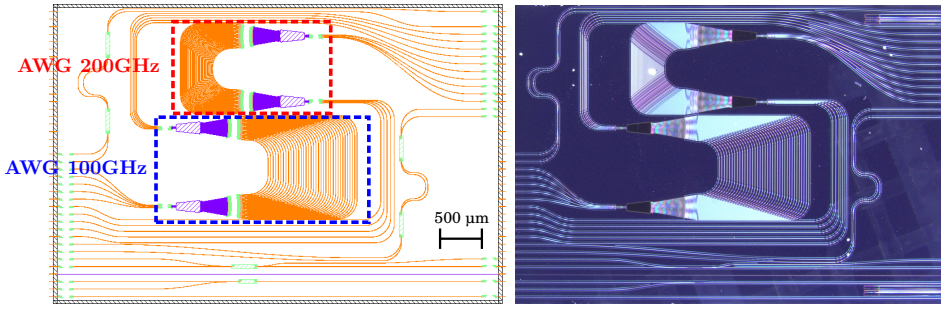

(a) (b)

Figure 2.3: AWG regular design for the HHI MPW run: (a) mask layout and (b) microscope picture from the fabricated devices.

the incremental length ΔL was 84.43 μm, while for the 200 GHz channel spacing AWG were 16 nm, 87 and 42.22 μm, respectively. The design layout is shown in Fig. 2.3-(a), alongside several test structures such as straight waveguides, MMIs and MZIs. A microscope picture of the fabricated devices is shown in Fig. 2.3-(b).

The measurements of the transmission spectra for both devices are provided in Figs. 2.4-(a) and (b), for the 100 GHz and 200 GHz AWGs, respectively. These measurements were performed using a broadband source (C&L Band ASE source, NP Photonics) and input/output polarizers to set at the input, and select at the output, the polarization. To record the spectrum, an optical spectrum analyzer (OSA YOKOGAWA AQ6370C) with 10 pm resolution was used. All the transmission spectra were normalized to the transmission spectrum recorded through a (test) straight waveguide. The chip was placed then on top of a copper submount whose temperature is kept to a reference of 25°C using a Thermoelectric cooler (TEC)[1].

For the 100 GHz AWG, the insertion losses are approximately 5 dB. The central wavelength is 1554.77 nm for TE polarization and 1553.97 nm for TM polarization, and the channel spacing is around 0.8 nm. Adjacent cross-talk between channels (following the typical adjacent cross-talk definition in a 3 dB clear window, see Appendix D for more information) is 16.11 dB and the noise floor around 20 dB below the channel peak maximum. The FSR is 8.1 nm. From simulations, the effective indices for each polarization at the central wavelength ($\lambda_{0,TE} = 1.55\ \mu m$) are $n_{eff,TE} = 3.194$ and $n_{eff,TM} = 3.191$ for TE and TM polarizations, respectively. Thus, the calculated central wavelength for TM polarization should be

[1]Thermoelectric coolers (TEC) are commonly used in optical systems, since the optical component/system behavior is temperature-dependent. The basic temperature feedback control system requires an active heating/cooling element, a temperature sensor and a TEC controller. The active heating/cooling element, known as a Peltier, is an electrical element that will heat or cool depending on the current flow injected. On the other hand, temperature sensors are typically thermistors, where the measured resistance is related with the temperature. Both elements are actively controlled by a TEC controller, which constantly reads the temperature from the thermistor and drives the Peltier to obtain the desired temperature on the chip.

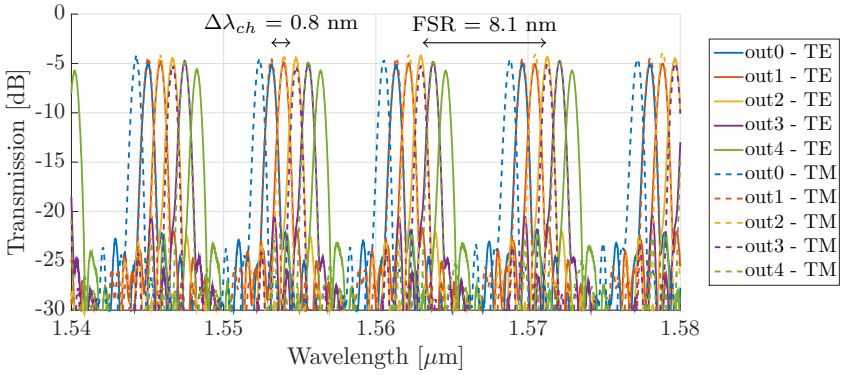

(a)

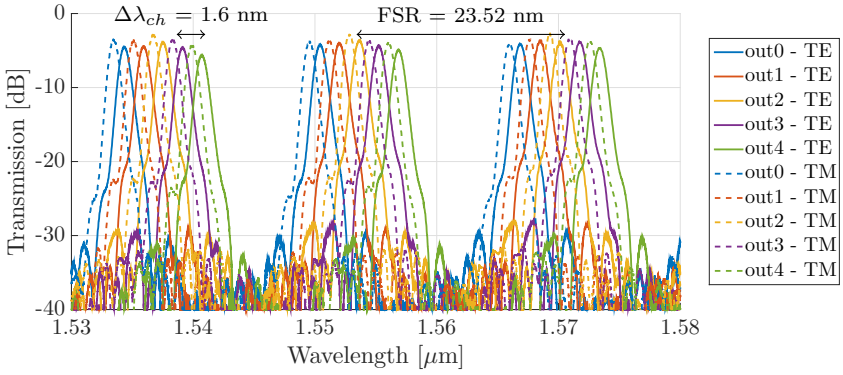

(b)

Figure 2.4: Measurements for TE polarization from the regular AWGs fabricated in the HHI MPW: (a) 100 GHz and (b) 200 GHz channel spacing.

$\lambda_{0,TM} = 1.5485\ \mu m$, obtaining a difference of approximately 1.5 nm. However, measurements show a difference of approximately one channel (0.8 nm). The big difference between simulations and measurements is due to the calculation of the effective index in the waveguide, which is not always as accurate as necessary. Even when the trend in the effective index calculation in terms of wavelength (i.e. group index, n_g) is usually correctly calculated as channel spacing and free spectral range fit with the design values, the deviation in the effective index makes necessary to perform different iterations in the simulation and fabrication steps to polish the obtained results. This is specially important when designing devices where the calculated effective index has to be very accurate, as for example in the case of polarization-independent AWGs [41].

For the 200 GHz AWG, the central wavelengths are 1553.66 nm and 1552.87 nm for TE and TM polarizations, respectively. The losses per channel are around 4 dB.

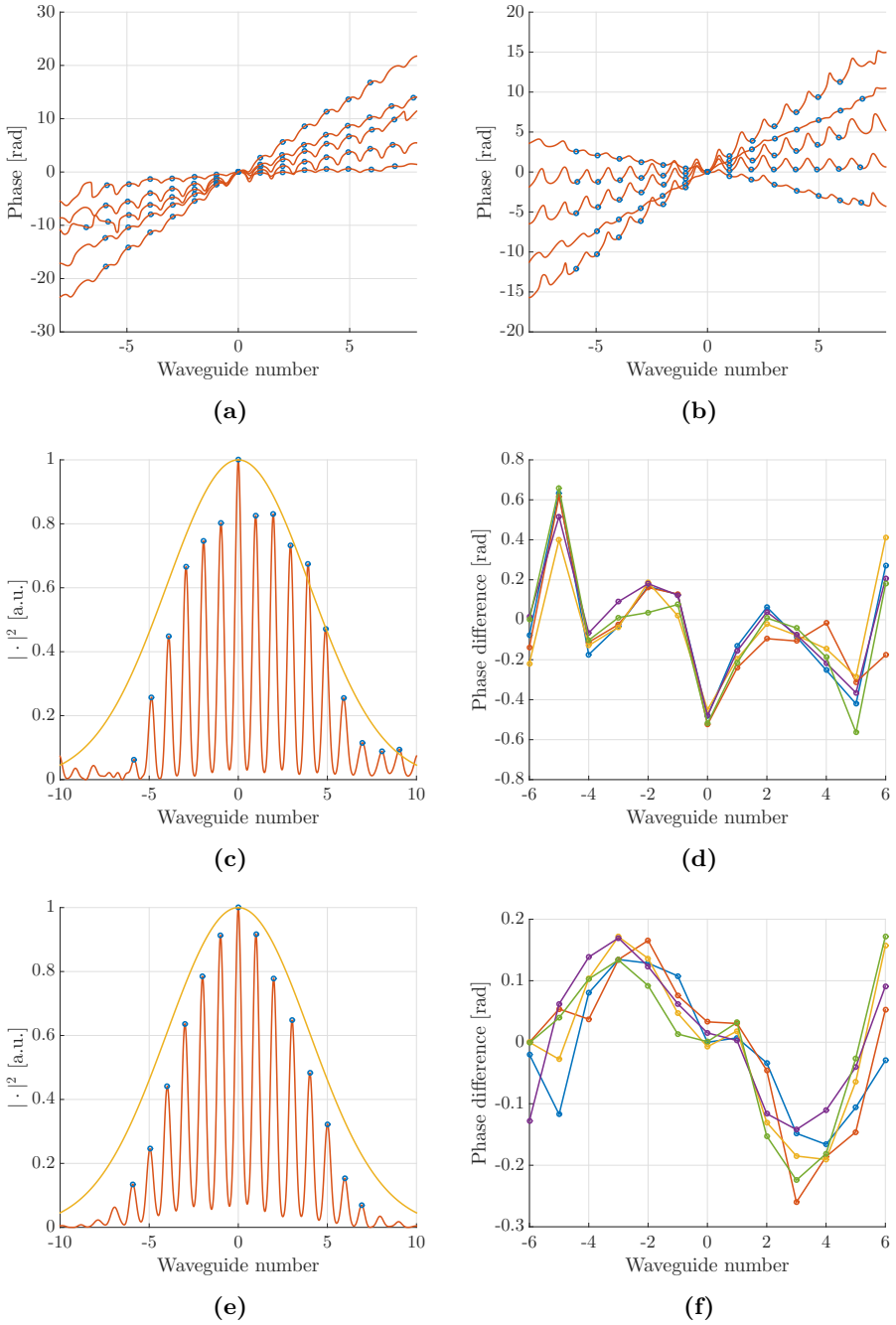

Figure 2.5: OFDR measurements for the regular AWGs in the HHI platform: phase in the different AWs from one input to the five different output waveguides for the (a) 100 GHz and (b) 200 GHz; (c) power and (d) phase error in the AWs for the 100 GHz AWG and (e) power and (f) phase error in the AWs for the 200 GHz AWG.

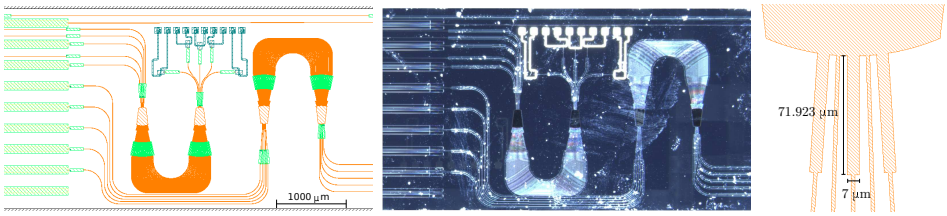

(a) **(b)** **(c)**

Figure 2.6: AWG flat-top design for the HHI MPW run: (a) mask layout, (b) microscope picture from the fabricated devices, and (c) detail of the MMIs at the input side of the slab coupler.

The separation between channels is 1.6 nm and the FSR is 16.46 nm. Cross-talk between channels is around 16.8 dB and the noise floor around 30 dB below the channel peak maximum.

The information retrieved by means of power transmission spectra measurements does not provide insight on the internal structure of the AWG response. Therefore, other interferometric techniques can be employed to extract the actual impulse response (amplitude and phase) of the device, such as low coherence interference [42] and optical frequency-domain reflectometry (OFDR) [43]. For our AWGs, we employed OFDR due to the requirement of mechanical translation stages in low coherence interference, as translation stages are usually more difficult to control and require long measurement times. On the other hand, the OFDR technique is also based on interferometry between the different arrayed waveguides, but using tunable lasers to obtain the different interferometric measurements. More information about the technique and the setup used to measure the devices can be found in Appendix E.

The OFDR technique was used to measure the internal structure of the AWG, that is, the amplitude and phase for each of the waveguides in the array. For these particular devices, the measurements were performed from the center input to the output waveguides. The design and layout of these regular AWGs result in a Gaussian field amplitude distribution in the array (see Eq. (2.4)) for every combination of input/output waveguides. For the phase, in this particular case from center input and center output, all the waveguides in the array are set by design to have the same phase (the relative phase is 2π as in Section 2.2). For the center input waveguides, and any other output waveguides, a linear phase distribution is expected in the array (see Eq. (2.5)).

Results from the OFDR measurements are presented in Fig. 2.5. Panels (a) and (b) show the phase measurement from the central input waveguide to the five different output waveguides (red line). Different arrayed waveguide positions determined by its temporal response are also included as blue circles. From these measurements, it is clear that the phase shift introduced between consecutive arrayed waveguides follows a linear trend, as is explained in Section 2.2. Panels (c) and (e) show the power in the arrayed waveguides when the central input and

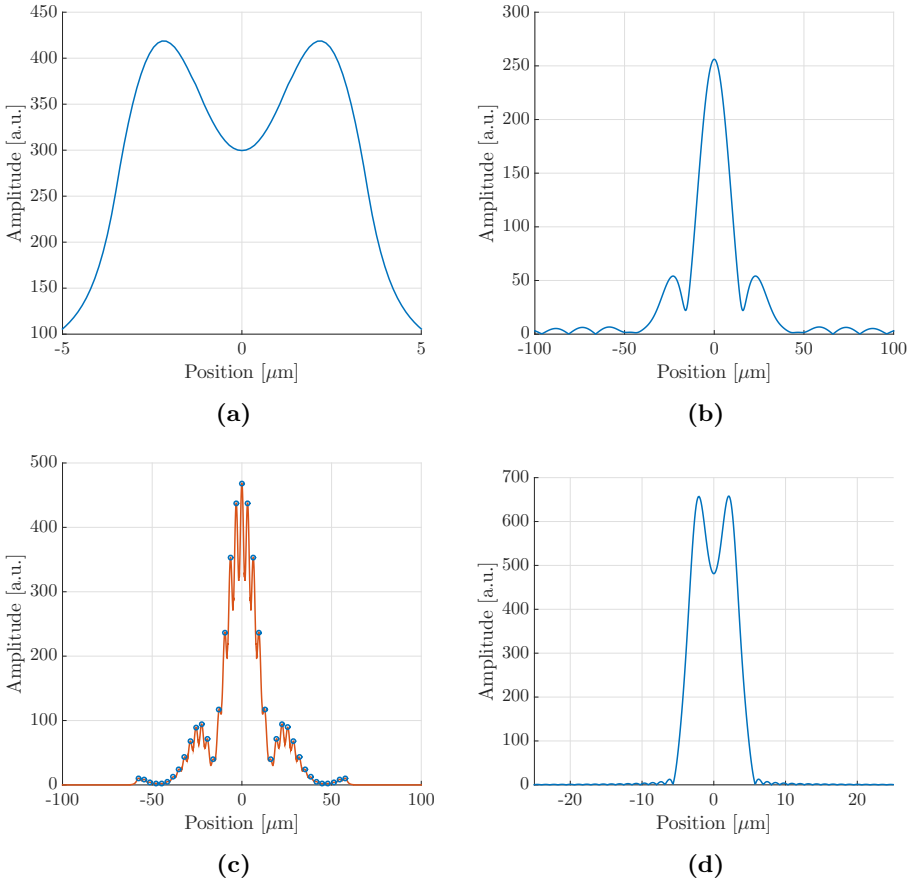

Figure 2.7: Simulations for the design of the flat-top AWG: (a) field at the end of the MMI, (b) field at the end of the first slab coupler, (c) coupled field at the arrayed waveguides, and (d) field at the output plane.

central output waveguides are used for the 100 GHz and the 200 GHz AWGs, respectively. As can be seen, the envelope is approximately a Gaussian function as is discussed in the previous section. The far-field Gaussian envelope obtained from simulations has been added to the figures (yellow line) for comparison, obtaining a good agreement between simulations and measurements. Panels (d) and (f) show the phase errors in each one of the five output waveguides using the central input waveguide to illuminate the AWG. Here, the phase errors are estimated to be less than 0.6 radians for the case of the 100 GHz AWG and less than 0.2 radians for the 200 GHz AWG. These results agree with the measured spectrums in Figs. 2.4-(a) and (b), where for the 200 GHz AWG the noise level is more than 5 dB lower than for the 100 GHz AWG, where the phase errors are higher.

Flat-top AWG

For this platform, one flat-top AWG using multi-mode interference couplers (MMIs) as input waveguides was also fabricated. The detailed description of flat top AWG designs is well documented in the literature [38, 44]. The design was done using a single waveguide cross-section in the array (single-etched), E1700 in the present technology (see Fig. 2.2), with a waveguide width of 2 μm and bend radius of 250 μm, analog to the regular AWGs described previously. The design parameters were: 5 input/output waveguides, central wavelength $\lambda_0 = 1597.615$ nm, channel spacing $\Delta\lambda_{ch} = 5.1$ nm and FSR 24 nm. Typically, AWGs are designed to have a FSR that is at least the number of channels times the separation between channels (cyclic AWG), or higher. However, the flat-top AWG designed in this section has a FSR lower than this number. This is then a special design case where the outer channels will be slightly overlapped between them.

The device layout and microscope picture are shown in Fig. 2.6-(a) and (b) respectively. In the same figure, panel (c) shows an enlarged view of the layout, at the input side of the device, where regular straight waveguides (width 2 μm) and MMIs are interleaved. The MMI dimensions are 7.0 μm width per 71.923 μm length in the E1700 cross-section, to transform the Gaussian-like mode shape from the input waveguide to a camel-like mode shape at the end of the MMI. This, as developed and detailed in [38, 44], results ideally into a flattened pass band shape for the AWG.

The AWG was simulated using the MMI as input waveguide, and the results are presented in Fig. 2.7. Panel (a) shows the field at the end of the MMI (i.e. at the beginning of the first slab coupler). In a typical monomode waveguide, the field shape is Gaussian, and then the transfer function (i.e. the channel pass-band shape) of the AWG will have a Gaussian shape (see Eq. (2.2) in Section 2.2). When a properly designed MMI is used as input to the AWG, the field is no longer Gaussian. Instead, it can be approximated by two shifted and overlapped Gaussians (at a distance of $\Delta x_m = W_m/2$, being W_m the width of the MMI) [38]. Then, panels (b) and (c) show the expanded field at the end of the slab coupler (as per Eq. (2.4)), and its sampled version corresponding to the array (Eq. (2.7)), respectively. Provided the array is properly designed, so it does not severely truncate the far field from the input waveguide, the AWG is a one to one imaging device. Therefore the camel-like input field will be imaged to the output, as is shown in panel (d). Its overlap with the Gaussian field of a regular output waveguide will result in a flattened pass band response.

The measurement setup and procedure employed was the same than for the regular AWGs in the previous section. In this case, measurements were performed injecting light either in the MMI equipped inputs, or in the regular waveguide inputs.

When using the MMI input, a flat-top response was obtained at the output channels, as is shown in Fig. 2.8-(a). In these measurements, the central wavelength λ_0 is approximately 1555.38 nm for TE polarization and 1554.37 nm for TM polarization. The losses per channel are between 4 and 10 dB for both po-

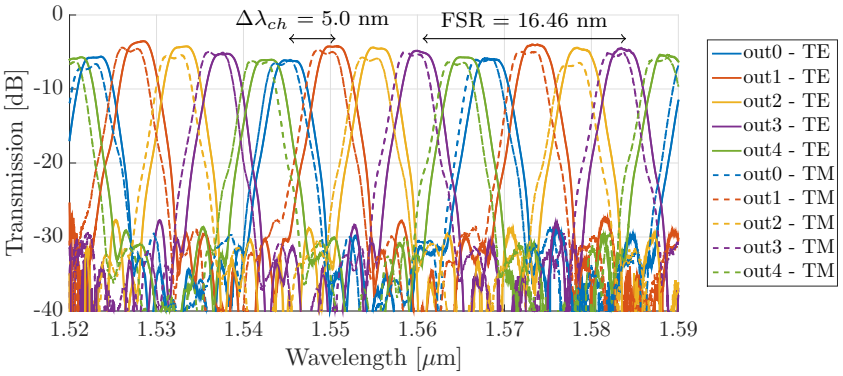

(a)

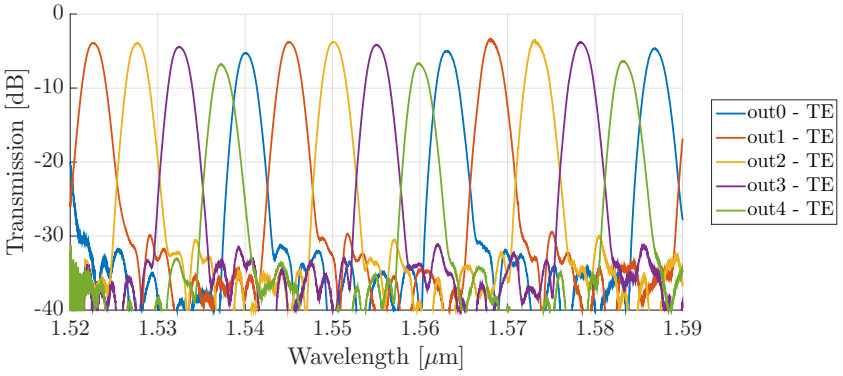

(b)

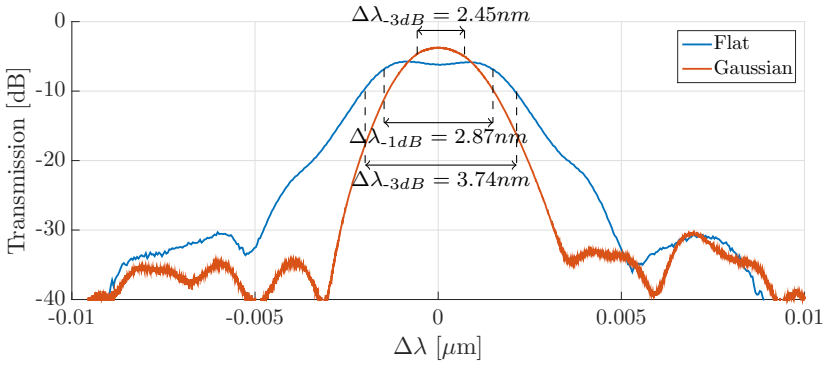

(c)

Figure 2.8: Flat-top AWG spectra, using (a) a MMI equipped input and (b) a regular waveguide input, respectively. (c) Comparison of both responses for a single channel.

larizations. This big asymmetry between losses is attributed to the big separation between the output waveguides, that will cause higher losses to the outer waveguides due to the focusing aberrations. From measurements, the separation between channels is 4.96 nm for both polarizations and the FSR 23.21 nm for both polarizations. The 1 dB, 3 dB and 20 dB channel widths are around 2.87, 3.74 and 8.81 nm, respectively. In this case, no side-lobes are present in the response of the AWG, and then the cross-talk will be measured referred to the noise-floor level, being approximately 28.7 dB.

For the case where a regular waveguide is used, the typical Gaussian spectrum is expected at the output waveguides. Figure 2.8-(b) shows the measurements when only TE polarization is used. The central wavelength is 1550.15 nm. The losses per channel are 3.7 for the best case and 6.7 dB for the worst case. The separation between channels remains the same (around 5 nm) and also the FSR (23.21 nm). The measured cross-talk is 29.33 dB, and the 1 dB, 3 dB and 20 dB channel widths are 1.24, 2.45 and 5.10 nm, respectively.

Figure 2.8-(c) shows a comparison between the central channel for the flat-top and Gaussian responses, centered to the same wavelength. This figure illustrates the difference between a channel using the MMI as input waveguide, where the 1 dB and 3 dB channel widths are clearly higher than in the case when a regular straight waveguide is used at the input.

Finally, the OFDR technique was used to measure the amplitude and phase in the AWs for the flat-top AWG. Figure 2.9 shows the measurements when the central input waveguide with MMI is used. Then, panel (a) shows the power distribution for the AWs. As has been commented before, the input field is no longer Gaussian and the field in the AWs will follow a sinc-like distribution. These results correspond for the main lobe very well with the simulations shown in Figs. 2.7-(b) and (c), plotted in the figure in yellow color. For the secondary lobes, results and simulations does not totally fit, and this can be attributed to the lack of dynamic range for the OFDR measurements in the lateral AWs. Please note that simulation results (yellow line) has been plotted in terms of power, while in Fig. 2.7 the results are presented in amplitude units. In panel (b), the phase errors measured as the difference in phase between consecutive waveguides are shown. From measurements, phase errors are lower than 0.6 radians, which agrees with previous measurements of regular AWGs in the same technology.

2.4 Silicon on Insulator AWGs

2.4.1 Overview

Amongst the different integration technologies, the smallest footprint devices are usually attained in Silicon on Insulator (SOI), due to its high index contrast, that allows bend radius down to 5 μm. For this reason, this technology is appropriated to fabricate AWGs since the total size of the device can be dramatically reduced. The fabrication of the devices in this section was performed in SOI by AMO GmbH

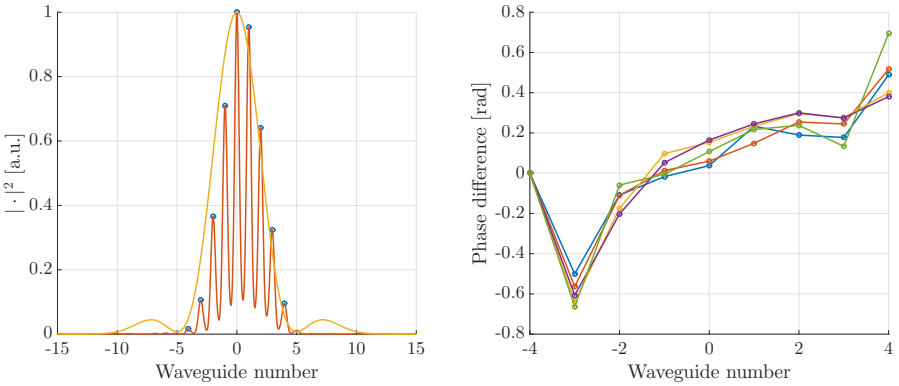

Figure 2.9: OFDR measurements for the flat-top AWGs in the HHI platform: (a) power and (b) phase in the AWs.

in Germany, using Electron Beam Lithography (EBL) and dry etching in a two-step process. First, using a negative resist in combination with a high contrast development process, all the waveguides were defined and fully etched to the buried oxide using a reactive-ion etching (RIE) process. Then, a positive resist mask was aligned to the waveguides defined in the first step, and it was used to define the shallow etched parts using a dry etching process. For both processes a multi-pass exposure approach was used to reduce the sidewall roughness and hence minimizing scattering losses and phase errors. Special care was taken to guarantee accurate critical dimensions of all parts of the device applying a very accurate proximity effect correction [45]. Although these devices were fabricated using EBL, there are multiple examples of AWGs [46] and other devices [47] fabricated using 193 nm and 248 nm UV-lithography in SOI.

Two different waveguide cross-sections (deeply and shallowly etched) were employed in the fabrication of these AWGs. A schematic for both is shown in Fig. 2.10, where the waveguides are composed of a 220-nm-thick Si guiding layer on a SiO_2 substrate with no cladding. These are commonplace in SOI photonics [23, 24].

2.4.2 Design and simulation

The libraries developed in this chapter were then used to design, simulate and perform the layout of the AWG, similar to previously validated models [48, 49]. The input/output waveguides were designed to use a 2.0 μm width shallowly etched cross-section. For the AWs, 0.8 μm width deep waveguides were used to minimize phase errors [47]. The effective index for these cross-section n_c was 2.67 for TE polarization and a central wavelength $\lambda_0 = 1.55$ μm, obtained from simulations using a commercial software [50]. Then, straight sections of the AWs were tapered

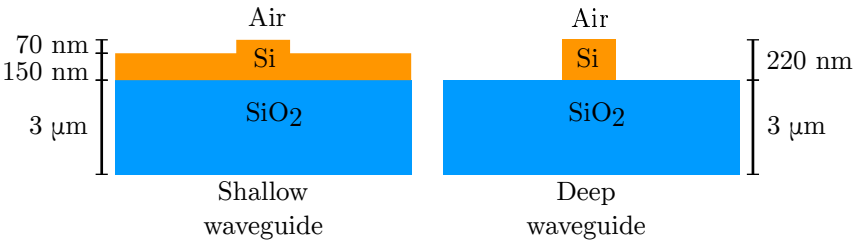

Figure 2.10: Waveguide cross-sections employed in the design and fabrication of the SOI AWGs.

down to 0.45 μm width in the bent sections, where a radius of 5 μm was used. Finally, an effective index n_s of 2.83 was obtained in the slab coupler also for TE polarization. The SOI chips designed employed grating couplers to insert/collect light into/from the chip. The grating coupler designs were for TE polarization, hence the AWG designs were for TE as well [51, 52]. 2D grating couplers have been reported as well in the literature [53], however both fiber polarizations are coupled to TE polarization in the chip plane.

The typical layout employed in SOI is the orthogonal layout (see Appendix B). This layout is very simple from a design point of view, since the bend radius is the same for all array arms [54]. Then, it is appropriate for technologies where the bend radius is very small, as is the case of SOI technology, since the size of the final layout will be small compared with other layouts.

For the design of the AWG, the design libraries introduced in Section 1.3 were developed for SOI technology and the orthogonal layout. These libraries enable to design AWGs from the high level parameters (i.e. channel spacing, FSR, number of channels...) and the obtained physical parameters are exported for simulation.

As AWG parameters, the number of channels was 7, the channel spacing was set to 1.6 nm (200 GHz) and the FSR was chosen to be 22.4 nm. With these parameters, the calculated focal length was 187.31 μm, the incremental length between AWs was 27.31 μm and the number of AWs was 49. The seven input/output waveguides were placed symmetrically around the center of the slab, with the fourth waveguide placed exactly in the center. Their positions were set according to the angular dispersion of the AWG and the angular positions given in [7]. Despite optimization procedures to minimize optical aberrations exist [55], they were not implemented in our devices.

For the AWG simulations, it is desired to be as accurate as possible. For this purpose, the AWG design libraries export all the physical parameters (waveguide length, bending radius, effective index for each wavelength...) and the simulation routines use the exported data. This method of simulation ensures that what is drawn in the mask layout is what is simulated, reducing the possibility of design errors. More information regarding the design libraries and simulation routines can be found in Appendix C. The SOI AWGs designed have been simulated using this procedure, obtaining the results in Fig. 2.11. From simulations, the insertion

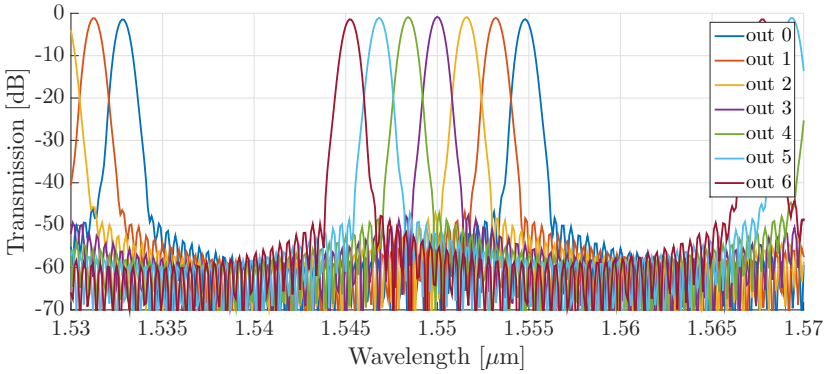

Figure 2.11: Orthogonal AWG transmission response simulation from the central input waveguide to the output waveguides.

losses are approximately 1 dB for the central channel and less than 1.5 dB for the outer channels. Note that this simulation shows the ideal response of the AWG, since propagation losses and other detrimental effects as fabrication imperfections were not included. As comparison, the typical insertion losses per channel of a regular SOI AWG are around 4-5 dB. From the simulation the 1-dB, 3-dB and 20-dB bandwidths are 0.39 nm, 0.65 nm and 1.58 nm, respectively.

2.4.3 Device fabrication and characterization

Following the analytical model presented in Section 2.2, an AWG with the aforementioned parameters was fabricated on the SOI substrate presented before. A microscope image of the fabricated device can be seen in Fig. 2.12-(a), and an enlarged view is presented in Figs. 2.12-(b) and (c). From the mask layout, the footprint for the orthogonal AWG is approximately 400×800 μm^2 (width×height). Several structures are on the chip area: test structures, regular AWGs (presented in this section) and reflective AWGs (presented in Chapter 4).

For the experiments, the chip was placed then on top of a copper submount whose temperature is kept to a reference of 25°C using a TEC. A broadband optical source (C&L Band ASE source, NP Photonics) was used at the input waveguide, and measurements were recorded using an Optical Spectrum Analyzer (OSA YOKOGAWA AQ6370C) with 10 pm resolution. To estimate the insertion losses in the AWG, all the traces were normalized with respect to a 0.8 μm width deep straight waveguide. The normalized spectra, from the center input to all the outputs, are shown in Fig. 2.12. Panel (a) shows the best case obtained from all the AWG measurements, where the peak insertion loss is approximately 3 dB (with ± 0.4 dB due to differences in the in/out coupling performance of the grating couplers) and the cross-talk level is 14 dB in the worst case channel.

Panel (b) shows the case where the higher cross-talk is obtained, as later on

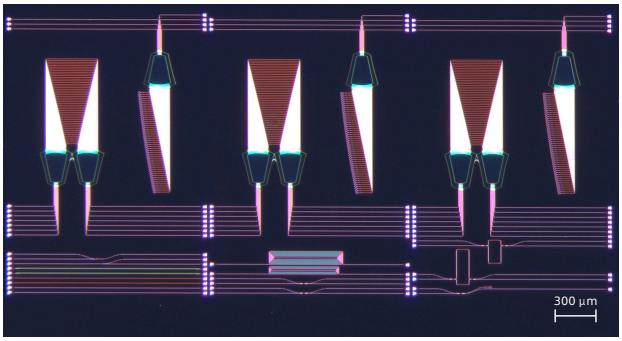

(a)

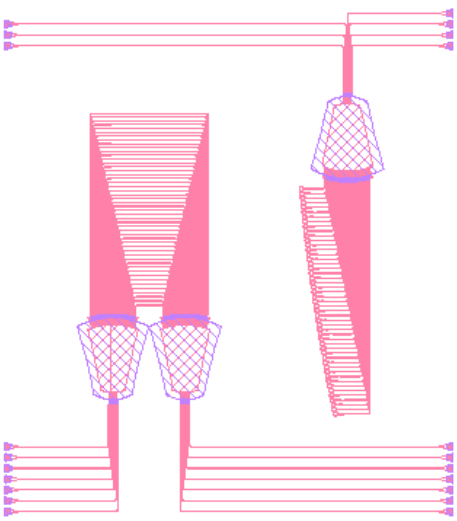

(b)

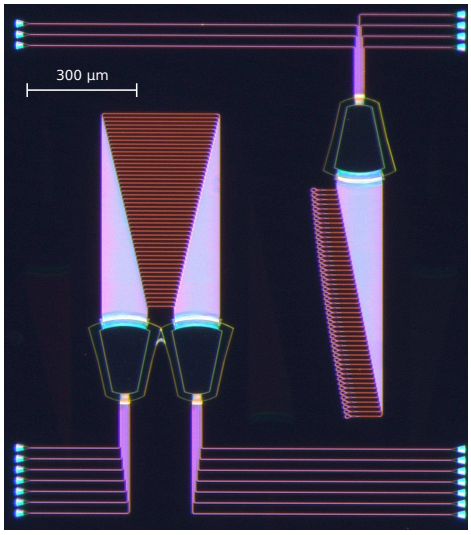

(c)

Figure 2.12: Orthogonal AWG fabricated in SOI: (a) Optical microscope image of the fabricated devices, (b) layout detail for one AWG and (c) microscope image.

this chapter the cross-talk will be tried to be reduced. From these measurements, the peak insertion loss is approximately 5 dB. The cross-talk, measured as the difference between the highest side lobe level and the channel level in a 3 dB clear window (see Appendix D), is as high as 7.4 dB. The relatively high side lobes in the response of the AWG can be attributed in part to the multi-mode nature of the 0.8 μm width straight sections used in the AWs. Besides, other detrimental effect may be the polarization rotation in the bent sections, as will be discussed in Chapter 3.3.2. Despite some simulation studies [56] state that polarization rotation is negligible for this waveguide width (0.45 μm in the bent sections) and the radius employed (5 μm), the slanted waveguide walls are not taken into account [40]. Moreover, discretization effects due to the grid snapping, could introduce a phase front distortion [57], since the EBL tool used a 5 nm grid snapping. This path length variation is in the order of $\pm$15 nm for the orthogonal layout, and through the effective index, this variation leads to a phase error of $\pm\pi/19$. Simulations accounting this random error are performed, showing the best achievable noise floor around -30 dB.

It must be remarked as well that even when taking into account the critical dimensions imposed by the foundry, fabrication is not always as good as can be expected. As an example to illustrate this, Fig. 2.14 shows scanning electron microscope images of the interface between shallow and deep waveguides. As can be seen, the etching is not correctly done when waveguide density is high, as is the case for the AWs. This phenomena may introduce amplitude and phase errors in the AWs, which will be translated to an increased noise floor or a distortion in the pass-band shape above the -30 dB level mentioned before.

2.4.4 Phase error measurements

As in Section 2.3, the OFDR technique was used to estimate the phase errors in the arrayed waveguides due to the fabrication process. As a first step, it was used with the SOI orthogonal AWG presented in this section, with the cross-section in Fig. 2.10. However, as shown in Fig. 2.13-(b), the cross-talk level is high. For this reason, a SiO_2 cladding layer of 700 nm height was deposited on top of the Si waveguide using plasma-enhanced chemical vapor deposition (PECVD), and then the AWG was measured again. The deposition of cladding reduces the index contrast in the waveguide, thus reducing the multi-mode behavior of the cross-section and the sensibility of the phase errors. Both effects should turn into a reduction of the cross-talk and the side-lobe level together with a shift in the central wavelength of the AWG.

Figure 2.15 shows a comparison of the measurements for both cases. Panel (a) shows the obtained power measurement in the AWs when using the central input and central output waveguides. As can be seen, the power profile in the AWs follows the typical Gaussian distribution, corresponding with the theoretical Gaussian profile obtained from simulations (yellow line). To complement the amplitude measurement, Fig. 2.15-(b) illustrates the phase error measurement for the case when no cladding has been applied (upper part) and when the cladding is on top of

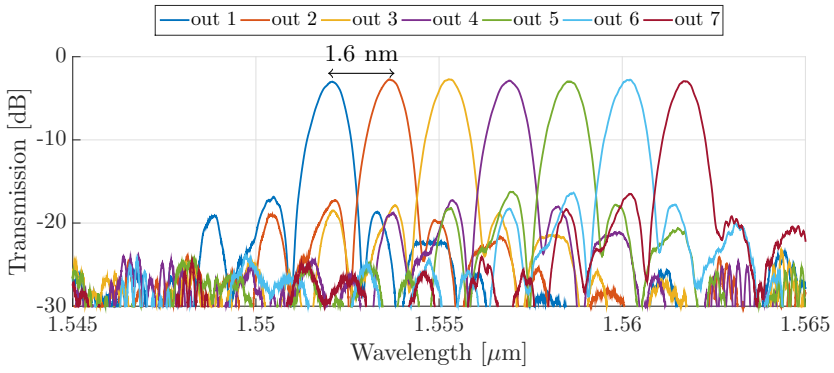

(a)

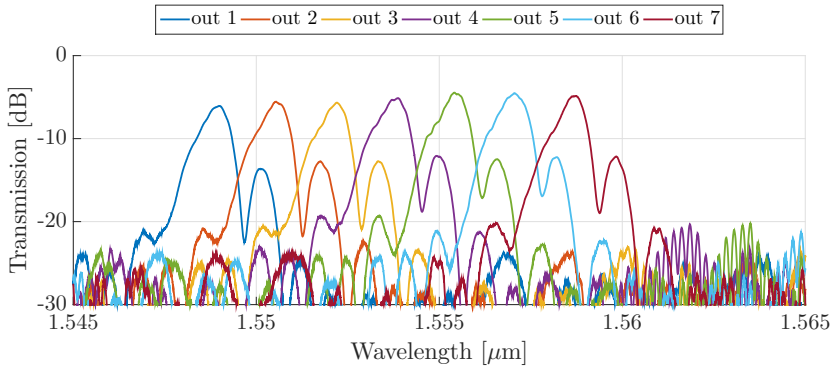

(b)

Figure 2.13: Measured spectral traces: (a) best AWG case and (b) higher side-lobe.

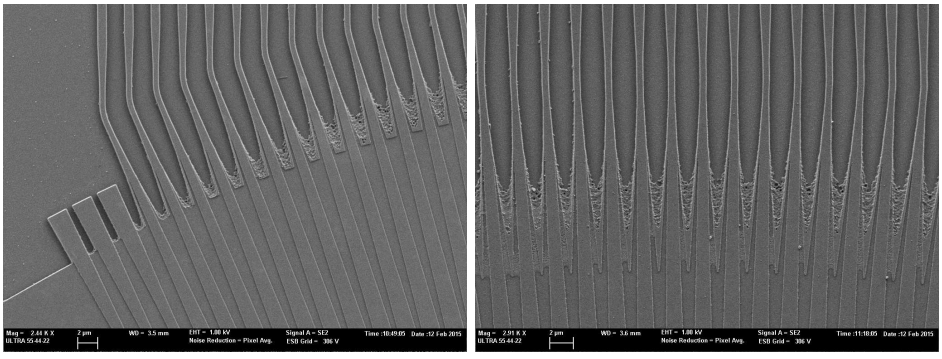

(a) **(b)**

Figure 2.14: Scanning electron microscope (SEM) images from the arrayed waveguides in the fabricated devices.

the chip (lower part). In the latter the measurements with no cladding have been also included in light grey color to make easier the comparison between both cases. When no cladding is on the chip surface, the maximum phase error is estimated to be around 1 radian. Then, the deposition of the cladding will reduce the index contrast and thus reduces the phase errors obtained due to the fabrication and the multimode behaviour of the waveguide. The maximum phase error when the cladding is deposited is 0.5 radians, and it is clearly visible how the phase errors are minimized in all the AWs.

Although the phase error reduction is not as high as expected looking at the phase measurements (almost 50% of phase error reduction), the overall response of the device is clearly improved. To illustrate this improvement, Fig. 2.15-(c) shows the spectral traces from the device with (dashed line) and without (solid line) cladding recorded using an optical spectrum analyzer and a broadband source. As a quality measurement, the difference between the peak maximum and the second peak of every channel was measured obtaining 6.72 dB in the case when no cladding was used and 11.62 dB when the cladding was applied. To illustrate these results, Fig. 2.15-(d) shows the spectrum for the output central channel in both cases centered at the same wavelength, where the side-lobe and the noise level are clearly improved.

2.5 Conclusions

In this chapter a review of the AWG has been presented. The AWG is a very well known device, and it is probably one of the most important components in optical communication networks where mux/demux devices are required. Since it is a passive device and can be integrated in almost any fabrication technology, its versatility is very high.

This chapter has served as the basis to develop the design libraries for the typical software used for photonic chip simulation and design [50]. The libraries can be used to design AWGs following an orthogonal layout for technologies as InP, thin SOI, thick SOI, TriPleX, SiNx or AlGaAs, and also can be easily modified to include any other technology. Other type of layouts, like the Smit or S layouts are still under development (see Appendix A for Si_3N_4 designs, and Appendices B and C for more information about the AWG layouts and the design libraries).

Two fabrication technologies (InP and SOI) were chosen to design, simulate and fabricate AWGs. However, more AWGs and its variants in different technologies will be shown during this thesis.

As a result, the InP AWGs show performances with side-lobe level ratios better than 16 dB for the 100 GHz and 200 GHz channels spacing regular AWGs. This technology shows a very good balance between phase errors due to fabrication and size of the final device, obtaining the best results when typical AWGs are designed. For the design where MMIs are employed to flatten the spectral response, noise-to-signal ratios better than 28 dB are obtained when a 5.1 nm channel spacing is used. OFDR measurements for both devices in this technology are shown to

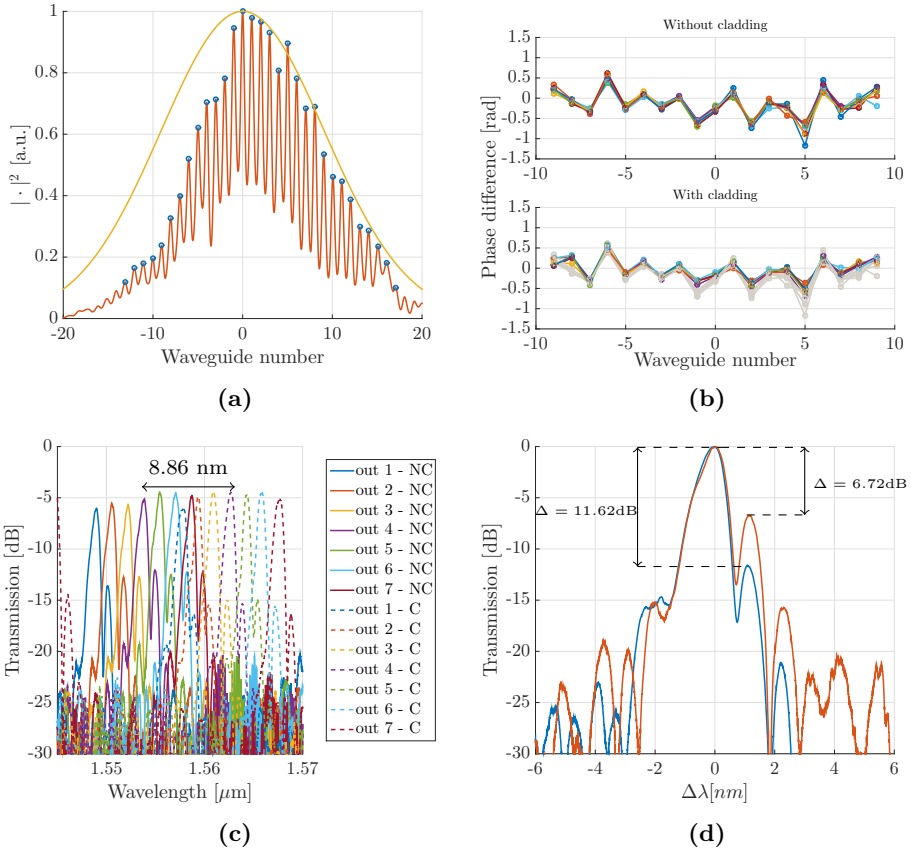

Figure 2.15: Measurement of the AWG without and with cladding: (a) power and (b) phase errors in the arrayed waveguides measured with the OFDR technique. Spectrum traces (c) recorded using an optical spectrum analyzer and (d) comparison of the central channel without (blue line) and with (red line) cladding.

compare the effect of the index contrast for the different technologies and illustrate the different fields profiles obtained depending on the input waveguide used.

For the AWGs fabricated in SOI, this technology has arose as the one obtaining the most reduced dimensions. The main reason is the high confinement due to the high index contrast that enables to use the smallest bending radius. As a drawback, this technology is the most sensitive in terms of phase errors, obtaining responses with side-lobe levels around 7 dB. As a solution, the introduction of a cladding can reduce the high index contrast, maintaining the same dimensions but reducing the side-lobe levels to 11 dB. This reduction of the phase errors when the index contrast is reduces has been checked and validate by means of the measurement with the OFDR technique, where it is possible to obtain the amplitude and phase in each AW independently.

In terms of phase errors, it may not be valid to attempt a direct comparison between the different technologies. Despite the AWGs presented in this chapter have the same or comparable design parameters (channel spacing, FSR, number of inputs and outputs), and all make use of an orthogonal layout, the fabrication processes are different. The phase errors are due mainly to the causes detailed in Section 2.3. All these structural effects depend not only on the materials and waveguide cross-section (index contrast) but also on the diverse process steps, and chemical recipes, employed during the lithography. Hence, it is possible to compare phase errors among devices in the same fab run, better at a die level (lithography variations happen among dies as extensively reported in the literature, e.g. for ring resonators in SOI). In Section 2.3 the comparison was established for AWGs of 100 and 200 GHz channel spacing in the same die. As said, despite one may be tempted to compare technologies in terms of phase errors, too many differences exist to attribute the dissimilar performance to a given factor.

The AWG design libraries developed in this chapter have been licensed to the UPV spin-off company VLC Photonics. Also, the results obtained through this chapter have been reported in the following publications:

- B. Gargallo, P. Muñoz, R. Baños, A.L. Giesecke, J. Bolten, T. Wahlbrink, and H. Kleinjans, "Reflective arrayed waveguide gratings based on Sagnac loop reflectors with custom spectral response," *Optics Express*, vol. 22, no. 12, pp. 14348–14362, 2014.

- B. Gargallo, P. Muñoz, R. Baños, A.L. Giesecke, J. Bolten, T. Wahlbrink, and H. Kleinjans, "Reflective Arrayed Waveguide Grating with Sagnac Loop Reflectors in Silicon-on-Insulator with Gaussian Pass-band," in *Proceedings of the 17th European Conference on Integrated Optics (ECIO)*, Nice, France, 2014.

- B. Gargallo, P. Muñoz, R. Baños, A.L. Giesecke, J. Bolten, T. Wahlbrink, and H. Kleinjans, "Silicon-on-insulator reflective arrayed waveguide grating with sagnac loop reflectors," in *Proceedings of the 40th European Conference on Optical Communication (ECOC)*, Cannes, France, 2014.

- B. Gargallo, P. Muñoz, and R. Baños, "Reflective Arrayed Waveguide Grating in Silicon-on-Insulator with flattened spectral response," in *Proceedings of the 19th Annual Symposium of the IEEE Photonics Benelux Chapter*, Enschede, The Netherlands, 2014.
- B. Gargallo, D. Doménech, R. Baños, D. Pastor, C. Domínguez, and P. Muñoz, "Design of Arrayed Waveguide Gratings in Silicon Nitride," in *Proceedings of the 20th Annual Symposium of the IEEE Photonics Benelux Chapter*, Brussels, Belgium, 2015.
- L.A. Bru, B. Gargallo, R. Baños, D. Pastor, J.D. Doménech, A.M. Sánchez, R. Mas, E. Pardo, P. Muñoz, "Optical frequency domain reflectometry applied to photonic integrated circuits," in *Proceedings of the 18th European Conference on Integrated Optics (ECIO)*, Warsaw, Poland, 2016.

Chapter 3
Interleave-chirped arrayed waveguide grating (IC-AWG)

In this chapter, a special configuration of an Arrayed Waveguide Grating is presented, termed Interleave-Chirped AWG (IC-AWG). This device is able to process optical signals, acting as WDM demux and polarization and phase diversity component. It may find use in receivers for coherent optical communications. The chapter is structured as follows: firstly, the formulation of a regular AWG in [34] is taken as the basis to derive the analytical equations. Secondly, a design procedure taking into account the selected technology and cross-section is provided. Finally, an example of design and fabrication of the IC-AWG is presented. The device has been fabricated in InP technology using the COBRA/SMART Photonics MPW platform, and it operates as a wavelength multi/demultiplexer unfolding the operation in each wavelength channel to four different phases and two polarizations.

3.1 Background and motivation

Coherent optical communications have regained interest in the last years [58], giving as a result photonic integrated circuits with aggregate speeds of up to 500 Gb/s [59]. Currently, the main block of integrated optics based coherent receivers is the Multi-Mode Interference (MMI) coupler, which can be designed to operate as the 90° hybrid necessary in every coherent detector. The combination of this element with wavelength multi/demultiplexers as the Arrayed Waveguide Grating (AWG) has been demonstrated [59], obtaining the advantages of Wavelength Division Multiplexing (WDM) systems merged with the ones derived from coherent optical communication technologies.

By this time, a lot of effort has been put in colorless configurations where no mux/demux devices are nedeed. The main idea of these systems is to reduce the

number of components (thus reducing the size of the resulting chip) obtaining the same operation but with less than 1-dB penalty [60, 61] in comparison with the case where mux/demux are used. However, these configurations require broadband tunable lasers, as for example the sample grating distributed Bragg reflector (SG-DBR) laser, which is big and not rapidly designed. Then, the use of demux devices can be used to reduce a broadband to smaller spectrum portions, where the use of distributed feedback (DFB) lasers will be enough.

For this reason, the IC-AWG reported in [15] is seen as the most compact solution for these systems, since it enables a three fold operation: the two aforementioned demultiplexing and 90° hybrid operations but also polarization splitting on-chip attained through the use of birefringent waveguides in the IC-AWG arms.

3.2 Model and design procedure

The following section describes a full field model for Interleave-Chirped Arrayed Waveguide Gratings. It was previously published in a peer reviewed journal, and is reprinted here with permission: B. Gargallo and P. Muñoz, "Full field model for interleave-chirped arrayed waveguide gratings," *Optics Express*, vol. 21, no. 6, pp. 6928–6942, © 2013 OSA, `dx.doi.org/10.1364/OE.21.006928`.

3.2.1 AWG layout

A schematic of a 2xN Arrayed Waveguide Grating (AWG) is shown in Fig. 3.1-(a). It consists of two input waveguides, followed by a free propagation region (FPR). At the end of this FPR, the field is coupled in the arrayed waveguides. In a conventional AWG design, the length of consecutive waveguides in the array differ by a constant value, Δl, which is an integer (m) multiple of the design wavelength (λ_0) within the waveguide, as shown in Fig. 3.1-(b). The accumulated phase shift depends on wavelength/frequency, which combined with the second FPR, leads to light focusing at different output positions for each wavelength. Moreover, the field discretization imposed in the arms, causes diffraction in different orders $(\ldots, m-1, m, m+1, \ldots)$, resulting in different Brillouin Zones (BZs) [8]. In an Interleave-Chirped AWG (IC-AWG), the array is divided in M subsets. Within each subset, whose waveguides are spaced Md_ω at x_1 and x_2, an additional floor length (related to λ_0) is introduced [62]. The division of the array in M subsets reduce the original BZ size by a factor M, as will be formulated in detail in the following sections. Besides, introducing different floor length in each subset, results in out of phase interference at x_3, for the fields diffracted by each subset. This can be seen in Fig. 3.1-(c), where the width of the focusing zones has been reduced by a factor M compared to Fig. 3.1-(b). Each group of these arrayed waveguides with the same incremental length is called subarray. Hence, if for example a $M = 4$ chirp pattern is used, the first subarray will be composed of the arrayed waveguides number $\{1, 5, 9, \ldots, N-3\}$, the second by $\{2, 6, 10, \ldots, N-2\}$ ... In this section, the model of the IC-AWG extending the Fourier optics AWG model presented

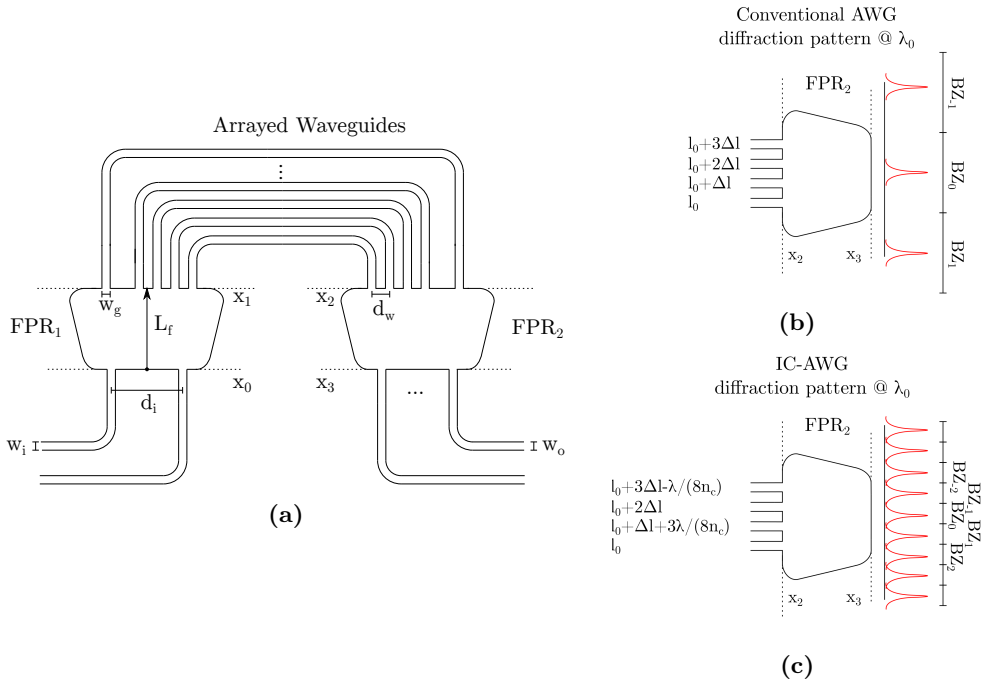

Figure 3.1: (a) IC-AWG layout. (b) Field focusing points without and (c) with chirp. Abbreviations: subscripts i, w and o stand for input, arrayed and output waveguides, respectively; ω: waveguide width; d: waveguide spacing; L_f: focal length; FPR: free propagation region; l_0: shortest AW length; Δl: incremental length; λ: wavelength; n_c: AW effective index; BZ: Brillouin Zone.

in [34] is formulated, starting from Eq. (2.3) in Chapter 2.2 since the IC-AWG will differ in the AWs. Table 3.1 shows a summary of the variables used in the formulation.

3.2.2 Field at the arrayed waveguides

Let the length of waveguide number r in each subarray be given by,

$$l_{r,k} = l_{c,k} + \Delta l' \left(r + \frac{N}{2M} \right) \tag{3.1}$$

with $\Delta l'$ being the incremental length between one waveguide and the next in the same subarray, and $l_{c,k}$ being the length of the shortest waveguide in subarray number k, used to account for different base length in each subarray and to introduce the chirp pattern in the AWs. The conventional AWG has a path length increment

b_i, b_g, b_o	Power normalized Gaussian function
B_i, B_g, B_o	Spatial Fourier transform of b_x
$\omega_i, \omega_g, \omega_o$	Mode field radius
γ	Frequency spatial dispersion parameter
α	Wavelength focal length in Fourier optics
n_s	Slab effective index
n_c	Array waveguides effective index
n_g	Group index
r	Waveguide number in the array waveguides
m	Grating order
$l_{r,k}$	Length of the r waveguide in subarray k
$l_{c,k}$	Length of the shortest waveguide in subarray k
Δl	Incremental length between AWs
$\Delta l'$	Incremental length between AWs in a subarray
Δf_{ch}	Separation between channels in frequency
t	Field at the output waveguides
$\Delta \nu_{pol}$	Frequency separation between polarizations
Δx_{pol}	Spatial separation between polarizations
M	Number of sub-arrays
$x_0 - x_3$	AWG planes
d_i, d_w, d_o	Waveguide separation
L_f	Focal length
v	Frequency
N	Number of array waveguides
β	Propagation constant
c	Speed of light in vacuum
λ	Wavelength
L_u	Loss nonuniformity
$f_1 - f_3$	Total field distributions
q	Number of the output waveguide
Δv_{bw}	Frequency 3-dB bandwidth
Δx_{FSR}	Spatial FSR

Table 3.1: Summary of the variables used in the formulation. Subscripts i, g and o stand for input, arrayed and output waveguides, respectively.

$$\Delta l = \frac{m\lambda_0}{n_c} \tag{3.2}$$

In this equation, m is the grating order, n_c is the effective index in the waveguides and λ_0 is the design central wavelength. In order to keep similar focusing properties for all the M subarrays, $\Delta l' = M\Delta l$. The phase shift introduced by waveguide r can be expressed as

$$\phi_{r,k}(\nu) = e^{-j\beta l_{r,k}} = e^{-j\beta\left(l_{c,k}+\Delta l'\left(r+\frac{N}{2M}\right)\right)} \tag{3.3}$$

being β the propagation constant for the AW:

$$\beta = \frac{2\pi n_c \nu}{c} \tag{3.4}$$

Using Eqs. (2.3) and (3.3) the field distribution at x_2 is given by:

$$f_2(x_2,\nu) = \sqrt[4]{2\pi\omega_g^2}\sum_{k=0}^{M-1}\left\{\prod\left(\frac{x_2}{Nd_\omega}\right)B_i(x_2)\,\phi_k(x_2,\nu)\,\delta_{\omega,k}(x_2)\,e^{j\beta\Delta l'\frac{k}{M}}\right\}\otimes b_g(x_2) \tag{3.5}$$

with

$$\delta_{\omega,k}(x_2) = \sum_{r=-\infty}^{+\infty}\delta(x_2 - Mrd_\omega - kd_\omega) \tag{3.6}$$

$$\phi_k(x_2,\nu) = \psi_k(\nu)\,e^{-j\beta\Delta l'\frac{x_2}{Md_\omega}} \tag{3.7}$$

$$\psi_k(\nu) = e^{-j\beta\left(l_{c,k}+\Delta l'\frac{N}{2M}\right)} \tag{3.8}$$

3.2.3 Second Free Propagation Region

To obtain the spatial field distribution at the end of the second FPR, the spatial Fourier transform of Eq. (3.5) is calculated as follows:

$$f_3(x_3,\nu) = \sqrt[4]{2\pi\omega_g^2}B_g(x_3)\cdot \sum_{k=0}^{M-1}\left[\operatorname{sinc}\left(Nd_\omega\frac{x_3}{\alpha}\right)\otimes b_i(x_3)\otimes\Phi_k(x_3,\nu)\otimes\Delta_{\omega,k}(x_3)\,e^{j\beta\Delta l'\frac{k}{M}}\right] \tag{3.9}$$

with,

$$\Phi_k(x_3,\nu) = \mathcal{F}\left\{\psi_k(\nu)\,e^{-j\beta\Delta l'\frac{x_2}{Md_\omega}}\right\}\Big|_{u=\frac{x_3}{\alpha}} = \psi_k(\nu)\,\delta\left(x_3 + \frac{n_c\nu\Delta l'\alpha}{cMd_\omega}\right) \tag{3.10}$$

$$\Delta_{\omega,k}(x_3) = \mathcal{F}\left\{\sum_{r=-\infty}^{+\infty}\delta(x_2 - Mrd_\omega - kd_\omega)\right\}\Bigg|_{u=\frac{x_3}{\alpha}}$$
$$= \frac{1}{M}\sum_{r=-\infty}^{+\infty} e^{-j2\pi k d_\omega \frac{x_3}{\alpha}}\delta\left(x_3 - r\frac{\alpha}{Md_\omega}\right) \quad (3.11)$$

which after some manipulation results in:

$$f_3(x_3,\nu) = \sqrt[4]{2\pi\frac{\omega_g^2}{\alpha^2}}B_g(x_3)\frac{1}{M}\sum_{k=0}^{M-1}\Bigg[\psi_k(\nu)\, e^{j\beta\Delta l'\frac{k}{M}}\cdot$$
$$\sum_{r=-\infty}^{+\infty} e^{-j2\pi r\frac{k}{M}} f_M\left(x_3 - r\frac{\alpha}{Md_\omega} + \frac{n_c\nu\Delta l'\alpha}{cMd_\omega}\right)\Bigg] \quad (3.12)$$

with,

$$f_M(x_3) = \mathrm{sinc}\left(Nd_\omega\frac{x_3}{\alpha}\right) \otimes b_i(x_3) \quad (3.13)$$

The argument of f_M in Eq. (3.12) shows the field at the output of the second FPR has its focusing point position determined by the number of subarrays, M, and the incremental length, $\Delta l'$. Moreover, the term $e^{j\beta\Delta l'\frac{k}{M}}$, is a phase shift dependent of the subarray number, and the term $e^{-j2\pi r\frac{k}{M}}$ is a phase shift dependent of the focusing position. Position x_3 and wavelength $\lambda = c/\nu$ are related through the frequency spatial dispersion parameter (FSDP) given by:

$$\gamma = \frac{cMd_\omega}{n_c\Delta l'\alpha} = \frac{\nu_0 d_\omega}{\alpha m} \quad (3.14)$$

3.2.4 Field at the output waveguides

At the output waveguides, the field can be obtained through the following overlap integral:

$$t_{0,q}(\nu) = \int_{-\infty}^{+\infty} f_3(x_3,\nu)\, b_0(x_3 - qd_0)\, \partial x_3 \quad (3.15)$$

where b_0 is the fundamental mode profile at the output waveguide (OW), q is the OW number and d_0 is the OW spacing.

3.2.5 Arbitrary IW position

All this formulation can be easily extended to the case with more than one input waveguide (IW), not only for the case with one input placed at the central position of the first FPR. The field at the IW can be expressed then as

$$b_{i,p}(x_0) = \sqrt[4]{\frac{2}{\pi\omega_i^2}} e^{-\left(\frac{x_0 - pd_i}{\omega_i}\right)^2} = b_{i,p}(x_0 - pd_i) \tag{3.16}$$

where p is the IW number and d_i is the IW spacing. At the output plane the field will be

$$f_3(x_3,\nu) = \sqrt[4]{2\pi\frac{\omega_g^2}{\alpha^2}} B_g(x_3) \frac{1}{M} \sum_{k=0}^{M-1} \Bigg[\psi_k(\nu) e^{j\beta\Delta l' \frac{k}{M}} \cdot \sum_{r=-\infty}^{+\infty} e^{-j2\pi r\frac{k}{M}} f_M\left(x_3 - r\frac{\alpha}{Md_\omega} + \frac{n_c\nu\Delta l'\alpha}{cMd_\omega} + pd_i\right)\Bigg] \tag{3.17}$$

and the field in the output waveguides is

$$t_{p,q}(\nu) = \int_{-\infty}^{+\infty} f_{3,p}(x_3,\nu)\, b_0(x_3 - qd_0)\, \partial x_3 \tag{3.18}$$

3.2.6 Modeling polarization dependence

This model can also be extended to the case where two polarizations are supported by the waveguiding structures. Although polarization dependence is minimized in conventional AWG [41], in the IC-AWG is engineered for the device to act as a polarization diversity component. Through Eq. (3.17) the shift between polarizations is given by:

$$\Delta x_{pol} = \frac{m}{d_\omega}\left(\alpha_{TM}(\nu) - \frac{n_{c,TM}(\nu)\,\alpha_{TM}(\nu)\,\nu}{n_{c,TE}(\nu_0)\,\nu_0} - \alpha_{TE}(\nu) + \frac{n_{c,TE}(\nu)\,\alpha_{TE}(\nu)\,\nu}{n_{c,TE}(\nu_0)\,\nu_0}\right) \tag{3.19}$$

The equation indicates that at the output plane each polarization is going to be focused at different position. The distance between TE and TM polarization focusing points, at a given ν, depends on the spacing, length and effective index of the AWs and length of the FPR. The frequency shift corresponding to the aforementioned distances, which in the literature is known as Polarization Dependent Wavelength Shift (PDWS) [41], is given by:

$$\Delta\nu_{pol} = \frac{n_{c,TE}(\nu_o)\,\nu_o}{n_{c,TM}(\nu + \Delta\nu_{pol})} - \nu - \frac{\alpha_{TE}(\nu)\,n_{c,TE}(\nu_o)\,\nu_o}{n_{c,TM}(\nu + \Delta\nu_{pol})\,\alpha_{TM}(\nu + \Delta\nu_{pol})} + \frac{\alpha_{TE}(\nu)\,n_{c,TE}(\nu)\,\nu}{n_{c,TM}(\nu + \Delta\nu_{pol})\,\alpha_{TM}(\nu + \Delta\nu_{pol})} \tag{3.20}$$

Equation (3.20) shows the wavelength separation between both polarizations as a function of the effective index of the AWs and the FPRs length. For $\nu = \nu_0$ it reduces to:

$$\Delta\nu_{pol} = \frac{n_{c,TE}(\nu_0)\,\nu_0}{n_{c,TM}(\nu_0 + \Delta\nu_{pol})} - \nu_0 \tag{3.21}$$

Equation (3.21) is extremely important in the design of the IC-AWG, since it shows that the PDWS only depends on the effective index of each polarization, and ν_0. For the design of IC-AWGs, described in Section 3.3, it will restrict the number of channels and their frequency spacing.

3.2.7 Design procedure

Using the equations derived in this section, it is possible to obtain a design procedure for the IC-AWG. Once the design frequency ν_0 is selected, the following steps are used to obtain the physical parameters of the IC-AWG.

1. Select the number of channels and the separation between them, Δf_{ch}. This will fix the necessary polarization spacing $\Delta\nu_{pol}$ in Eq. (3.21), and then the geometry of the arrayed waveguides necessary to obtain the quotient between polarization effective indexes.

2. Set the spatial separation between polarizations in Eq. (3.19) as half free spectral range (FSR). The FSR is given by:

$$\Delta x_{FSR} = \frac{\alpha}{M d_\omega} \tag{3.22}$$

   This will set the grating order m through:

$$m = \frac{1}{2M}\frac{n_{s,TM}(\nu_0)}{n_{s,TE}(\nu_0)}\frac{n_{c,TE}(\nu_0)}{n_{c,TE}(\nu_0) - n_{c,TM}(\nu_0)} \tag{3.23}$$

   Note that this maximizes the spectral usage, as half of the spatial FSR is filled with TE, whereas the other half with TM channels/wavelenghts. Following [41], the array order m is not the order of the demultiplexer, because the waveguide and material dispersion must be taken into account through the group index n_g. It can be incorporated through the modified grating order $m' = (n_g/n_{c,TE})\,m$.

3. Use Eq. (3.2) to obtain the necessary incremental length between arrayed waveguides Δl. The used $\Delta l'$ for each subarray will be M times the calculated Δl.

4. Calculate the loss nonuniformity L_u due to $B_g(x_3)$ in Eq. (3.12) through:

$$L_u(dB) = 20\log_{10}\left(\frac{B_g(0)}{B_g(\Delta x_{Lu})}\right) \tag{3.24}$$

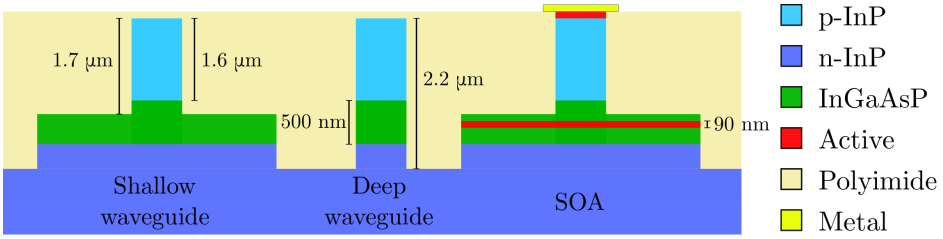

Figure 3.2: Available cross-sections in COBRA/SMART Photonics MPW.

where the worst case is considered an output waveguide located a distance Δx_{Lu} that corresponds to $M-1$ grating orders shift of the central grating order m, and a central input waveguide. This will allow to place the input waveguides in any point in the input plane. Hence, the loss nonuniformity will be:

$$L_u\,(dB) = 20\log_{10}\left(\frac{1}{e^{-\left(\pi\omega_g\frac{M-1}{Md_\omega}\right)^2}}\right) \tag{3.25}$$

From here it is possible to obtain the arrayed waveguides distance d_ω.

5. Obtain the frequency 3-dB bandwidth by using [34]:

$$\Delta\nu_{bw} = 2\gamma\omega_0\sqrt{2\ln\left(10^{3/20}\right)} \tag{3.26}$$

and derive the focal length L_f with Eq. (3.14). Note that the FSDP parameter γ has to take into account the dispersion through the modified grating order m'.

6. Calculate the output waveguide distance through:

$$L_f = \nu_0\frac{n_s}{n_g}\frac{d_0}{\Delta f_{ch}}\frac{d_\omega}{\Delta l} \tag{3.27}$$

where n_g is the group index of the arrayed waveguides [7].

7. Finally, the input waveguides will be positioned equidistant to the center of the input plane x_0 and separated a fraction M of the focusing zone. In the case of a 90° optical hybrid with 4 subarrays, the input waveguides will be at the positions $\pm\frac{1}{2}\alpha_{TE}\,(\nu_0)\,/\,(Md_\omega)$.

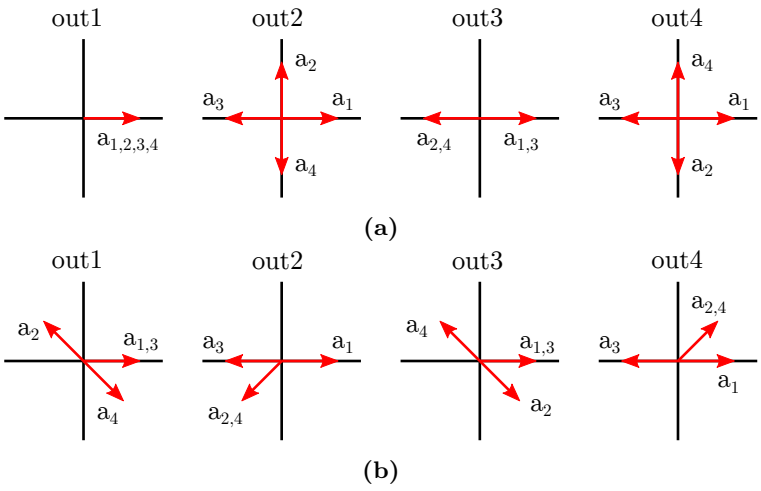

Figure 3.3: Vectorial representation of the field due to each of the 4 subsets at the output waveguides spaced a quarter of the spatial FSR when (a) the regular AWG and (b) the IC-AWG are analyzed.

3.3 Experimental validation

In this section, the experimental demonstration of an IC-AWG is provided. The device has been designed for the InP generic technology of COBRA Research Institute Eindhoven [63], the Netherlands[1], and it has been manufactured through a MPW run.

In this process, a three step epitaxial process is used to obtain the structures shown in Fig. 3.2. First, the active layer stack is grown epitaxially using a n-doped InP wafer as source [20]. Note that the active layer consists of one InGaAsP layer with a bandgap of 1.55 μm sandwiched between two InGaAsP layers with a bandgap of 1.25 μm. Then, the active material is selectively removed, and a new layer of InGaAsP transparent at 1.55 μm (bandgap 1.25 μm) is regrown up to the same level. In the last step, all the wafer is covered with p-doped InP material as cladding.

Once the layerstack is defined, the next step is to etch the waveguides. In this platform, the waveguides are defined by photolitography with a resolution down to 90 nm [20]. Then, using a double-etch process, shallow and deep cross-sections can be defined, as shown in Fig. 3.2.

This platform also offers a set of library of building blocks, as for example: tapers (including linear and parabolic tapers), multi-mode interference couplers and multi-mode interference reflectors, shallow to deep transitions, waveguide crossings, isolation sections, arrayed waveguide gratings, phase modulators, semicon-

[1] At the time of writing, this technology is currently provided by its spin-off company SMART Photonics.

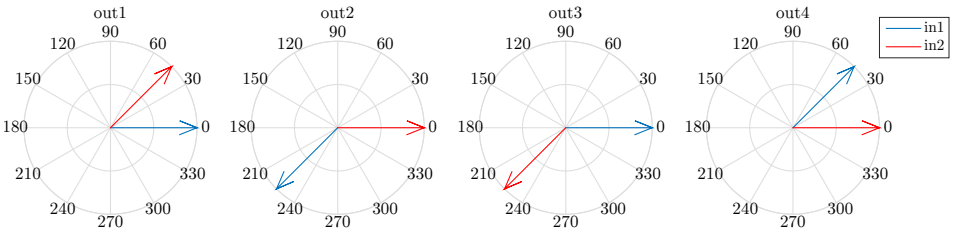

Figure 3.4: Vectorial representation of the field at the output waveguides using two input waveguides separated a spatial FSR (in1 and in2).

ductor optical amplifiers, PIN diodes and saturable absorbers. More information can be found in [25].

3.3.1 Design

The IC-AWG has been designed for the InP technology of JePPIX at the COBRA fab [20, 63], explained before and, for the design, the methodology described in Sec. 3.2 is followed.

In this case, the IC-AWG is thought to be designed operating with two channels per polarization and four different phase relations. For this reason, the number of outputs will be 16. The birefringence due to the 2.1 μm width deeply-etched waveguides used in the array is 1.6 nm between polarizations. Then, the channel spacing to provide the desired operation is 0.8 nm (100 GHz). The design free spectral range (FSR) has been set to 3.2 nm, to obtain a cyclic operation with both polarizations, and the central wavelength is 1550 nm. This results in a free propagation region length of 384.6 μm, and an incremental length between arrayed waveguides of 51 μm, with a grating order $m = 107$. The space between arrayed waveguides is set to the minimum allowed from the foundry (0.75 μm), and the curvature radius is 162 μm.

To enable the 90° optical hybrid operation, a chirp pattern $\{0, 3\pi/4, 0, -\pi/4\}$ is used, the same as [15]. Therefore, each subarray has a small base incremental length according to this chirp pattern and the central wavelength [64]. To illustrate the effect of the chirp pattern in the IC-AWG, the response of the regular AWG will be first analyzed. Figure 3.3-(a) shows the field in 4 output waveguides spaced a quarter of the spatial FSR, if the arrayed waveguides are divided in 4 subsets (a_1, a_2, a_3 and a_4). Then, if using one wavelength, the contribution of each subset will cause a constructive interference in one spatial position (out1) while in the other positions the interference will be destructive (outs 2, 3 and 4).

When the aforementioned chirp pattern ($\{0, 3\pi/4, 0, -\pi/4\}$) is introduced, the contribution of each subset will be modified, obtaining now the response in Fig. 3.3-(b). Here, the additional length introduced in the second and forth subsets causes a non-destructive interference in each of the four arms. Moreover, the resulting phases in each output waveguide due to the introduced chirp pattern can be used to obtain the 90° optical hybrid operation, since placing an input waveguide in

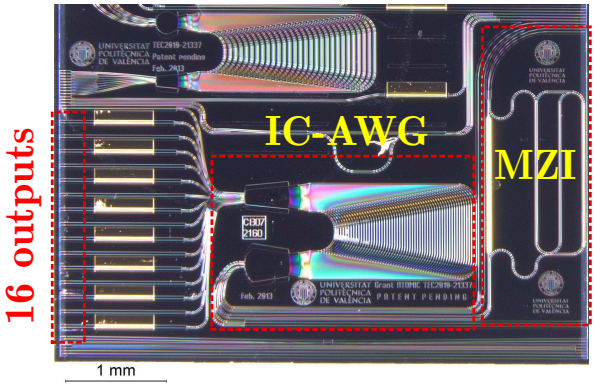

Figure 3.5: Optical microscope image of the fabricated device.

a distance that will be a quarter of the spatial FSR will cause a field pattern like the represented in Fig. 3.4. In this figure, the field due to the two input waveguides is plotted in each one of the four output waveguides when the chirp pattern has been introduced. As can be seen, the phase differences between the two input waveguides will be 45°, 135°, -135° and -45° for each output waveguide, respectively. Thus, these resulting phases are the necessaries to attain the optical hybrid functionality in the IC-AWG.

Note that there are multiple combinations of incremental lengths to ensure four outputs with the same power [62], but this is the only one to achieve the 90° hybrid operation [15]. For this design, no optimizations for the input/output waveguides regarding focusing aberrations are done.

In order to asses on the phase relations of the subarrays, an auxiliary 2x2 Mach-Zehnder interferometers has been connected to the input of the IC-AWG, similar to the metodology in [65] for MMI-based 90° optical hybrids. This MZI has a FSR of 80 pm, which results in an incremental length between arms of 8.124 nm. The two outputs of the MZI are to connected to input positions of the IC-AWG separated one spatial FSR.

3.3.2 Characterization

The fabricated device can be seen in the microscope picture in Fig. 3.5, where the IC-AWG and the auxiliary MZI are marked with a red box. The size of the chip is the one provided by the MPW run (4.1×4.7 mm^2), while the size of the IC-AWG is approximately 0.9×2.0 mm^2.

The chip is placed in a copper submount and fixed with a vacuum chuck. The temperature of the sample has been kept to 25°C during the experiments using a thermoelectric cooler (TEC). An optical broadband source (C&L Band ASE source, NP Photonics) is used at the input waveguides, and the measurements at the output waveguides are recorded using an Optical Spectrum Analyzer (OSA YOKOGAWA AQ6370C) with 10 pm resolution. In this case, all the spectral

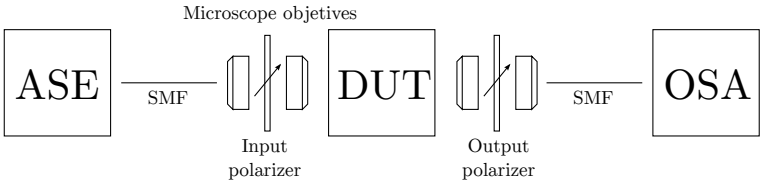

Figure 3.6: Measurement setup schematic including the polarizers.

traces shown are normalized to the maximum value of all traces in the same graph.

An important issue in practica AWG devices is the polarization rotation in bends [66]. A bent waveguide has slightly rotated polarization axis, with respect to a straight waveguide in the same cross-section. This is usually the case when the sidewalls are not perfectly vertical. Therefore, even ensuring a single polarization in the straight waveguide (which is hardly difficult in practice due to chip tilt on the chuck with respect to the in/out coupling objectives), in the interface between a straight and bent waveguide coupling between one of the linear polarizations in the straight to the two other in the bend happens. For this reason, two polarizers are included before and after the device under test (DUT), as can be seen in Fig. 3.6. The light is coupled then in and out the chip using edge coupling with microscope objectives. As a comparison to illustrate the issue of polarization rotation in the bent waveguides in this device, Fig. 3.7-(a) shows the measurement of one IC-AWG channel using the input polarizer, to ensure that mainly TE polarization is introduced in the device, and with/without the output polarizer. The blue trace shows the output without polarizer, whereas the red trace corresponds only to TE. Clearly, despite mostly TE is injected to the chip, a significant amount of TM is present when no filtering is applied at the output, and this is attributed to polarization rotation in bends as reported in [40] for AWG devices in the same InP technology.

Next, in order to asses on the FSR of the IC-AWG, four outputs with the same channel are measured. As can be seen in Figs. 3.7-(c) and (d), the chosen outputs are 0, 4, 8 and 12 for each polarization (TE and TM). As a result, the measured FSR of 3.2 nm matches very well with the simulated, which means that the group index (n_g) obtained from the waveguide cross-section simulations is approximately the real one, since the FSR in an IC-AWG depends on this group index (see Sec. 3.2).

Once the group index related figures (FSR an channel spacing) are checked, the waveguide birrefringence is investigated. For this purpose, one output waveguide is measured for each polarization, changing the input and output polarizers (Fig. 3.7-(a)) to ensure that mostly TE or TM polarization is entering to the chip and the possible polarization rotation is avoided with the output polarizer. The result can be seen in Fig. 3.7-(b), where the measured PDWS, related to the birrefringence through Eq. (3.21), is 2.6 nm. It is important to remark that the PDWS will be measure as the wavelength shift between polarizations for the same diffraction order. In this way, Eq. (3.2) can be used to estimate the central wavelength for

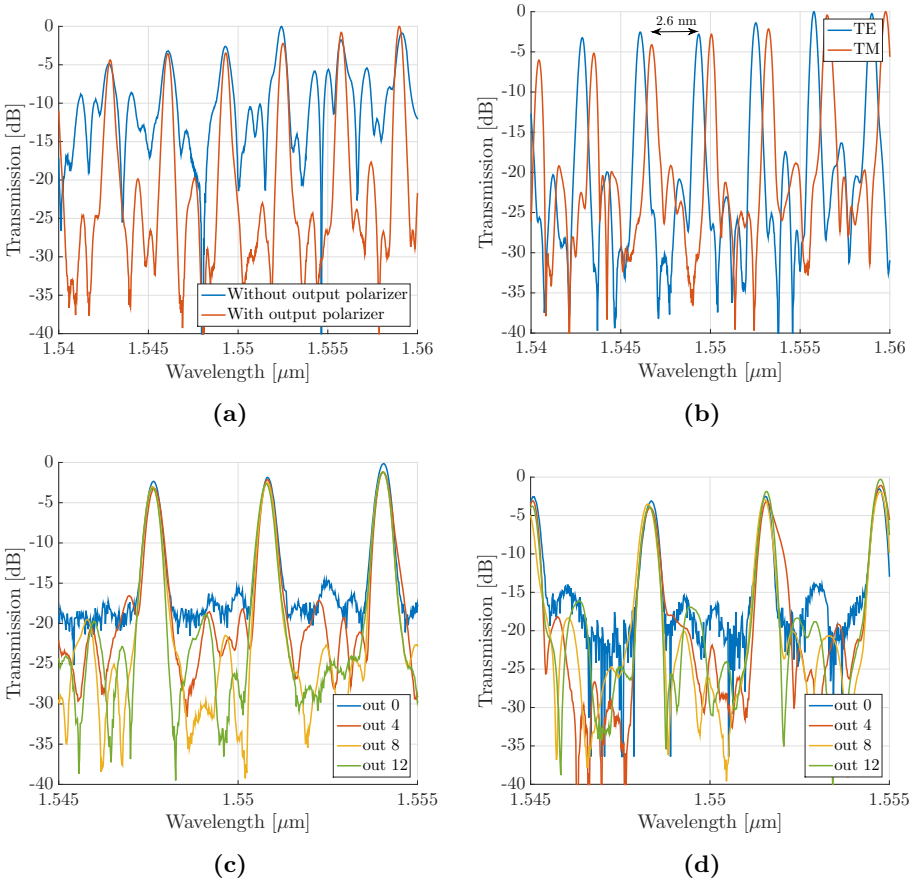

Figure 3.7: Measurements of the IC-AWG: (a) same AWG channel using an input polarizer and with (green) and without (blue) the output polarizer, (b) one channel for each polarization (TE and TM) to extract the PDWS, and spectra of four outputs with the same focused channel for (c) TE polarization and (d) TM polarization.

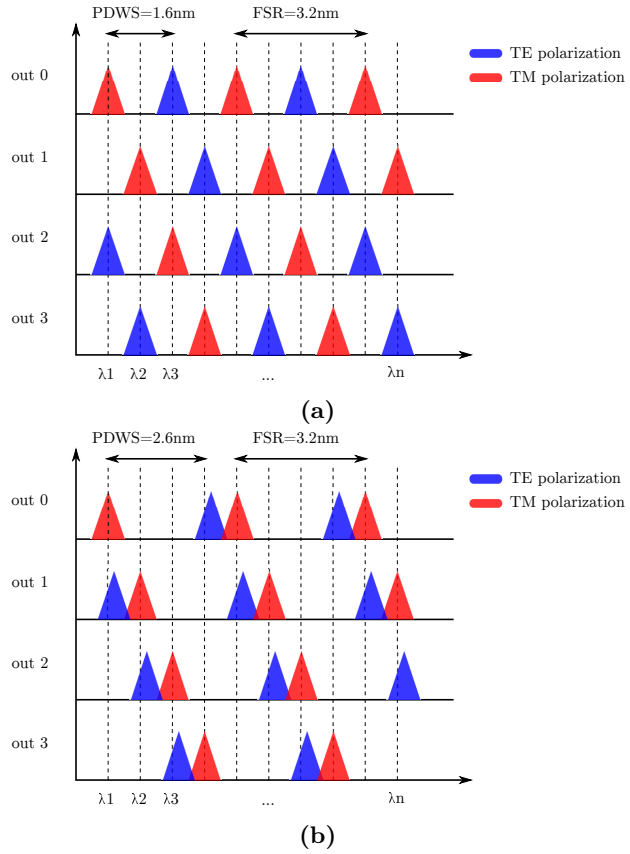

Figure 3.8: Wavelength map for four consecutive outputs: (a) designed and (b) measured.

each polarization. Since the effective index in one chosen cross-section will be lower for TM polarization compared with TE polarization at one wavelength when using this technology, then for the same output waveguides the wavelength channel will be in lower wavelengths for TM than for TE polarizations.

The measured PDWS is higher than the 1.6 nm obtained from simulations, and this will affect the wavelength map planned for this design. The wavelength map simulated for four channels distributed in two channels per polarization is shown in Fig. 3.8-(a). For the targeted FSR of 3.2 nm and PDWS of half this FSR (1.6 nm), wavelength λ_i is mapped to outputs out0 (TM) and out2 (TE) and λ_{i+1} is present in outputs out1 (TM) and out3 (TE). Since the measured PDWS does not corresponds to the simulated one, we will obtain an overlap in the channels for both polarizations, as is shown in Fig. 3.8-(b). Then, wavelength λ_i is mapped to output out0 for TM polarization, but is no longer present in out2 for TE polarization, whereas it is present but slightly shifted in out1 for TE

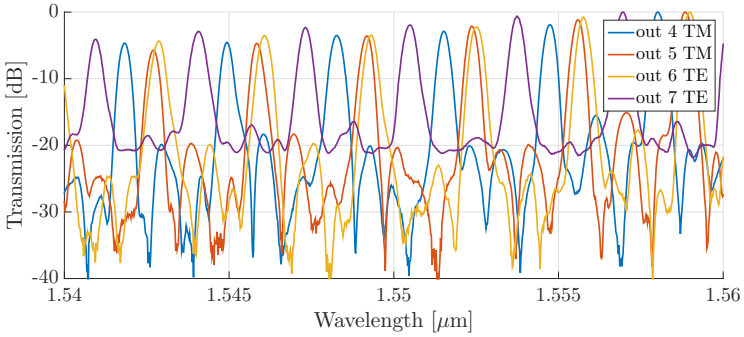

Figure 3.9: Measurement of four consecutive channels for TE and TM polarizations.

polarization. In the case of the wavelength λ_{i+1}, it is present in out1 for TM polarization and it is also present in out2 for TE polarization, with a slight shift. Thus, the measured wavelength map does not correspond with the simulated one. Because the PDWS only depends on the effective indexes for each polarization (see Eq. (3.21)), the effective index obtained from simulations for one or both polarizations is not correct.

The mismatch in PDWS can be appreciated in the measured spectra of Fig. 3.9. In this figure, it is shown the spectra corresponding to 4 consecutive outputs: 4, 5 for TM and 6, 7 for TE. As a result, the channels for the same polarization are correctly spaced 0.8 nm, as per design. Starting at channel 4 for TE polarization and looking to shorter wavelengths, channel 8 for TM polarization TM should be placed by design at 1.6 nm away, however it appeared at 2.6 nm, confirming the PDWS mismatch between design and fabrication.

Finally, the assesment on the phase diversity (90°) of the device is perfomed. For this purpose, the spectra of 4 outputs spaced the chirp interval P=4 is recorded, in this case the output waveguides numbers 2, 6, 10 and 14 for TE polarization and using the MZI as input. The results are shown in Fig. 3.10 where, as per design, the same wavelength channel is collected at all the outputs, as previously shown in Figs. 3.7-(c) and (d). Exceptionally, severe pass-band degradation is observed for channel 14. This degradation can be attributed to the very aggressive design, where a very narrow channel spacing of 0.8 nm is used, and also to the fact that no input/output position corrections were done to account for optical aberrations [55] for the present large slab coupler aperture obtained in the layout. Equivalent results are obtained for TM. The measured phase relations are not exactly the designed ones (90°,90°,90°,90°), but the value is very similar being (107.4°,93.9°,65.8°,92.9°) for the channel shown in Fig. 3.10-(b) and (92.5°,79°,102.6°,85.8°) for the channel in Fig. 3.10-(c). This difference can be attributed either to phase errors in the subarrays or to imprecisions during measurements due to the fact the small FSR MZI (80 pm) might drift between the time required to reposition the output lensed fiber, albeit the use of TEC.

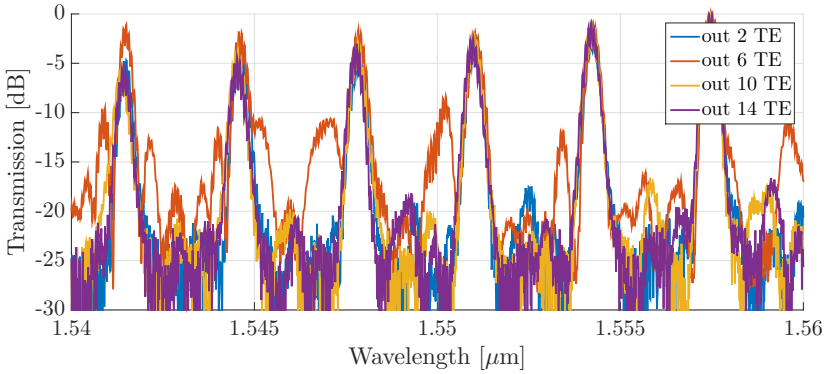

(a)

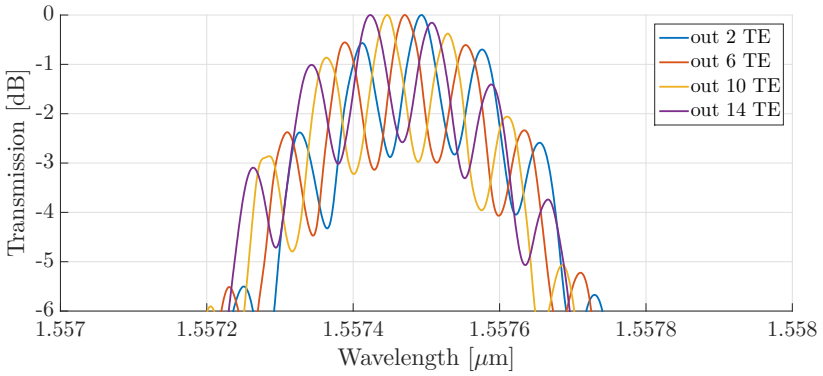

(b)

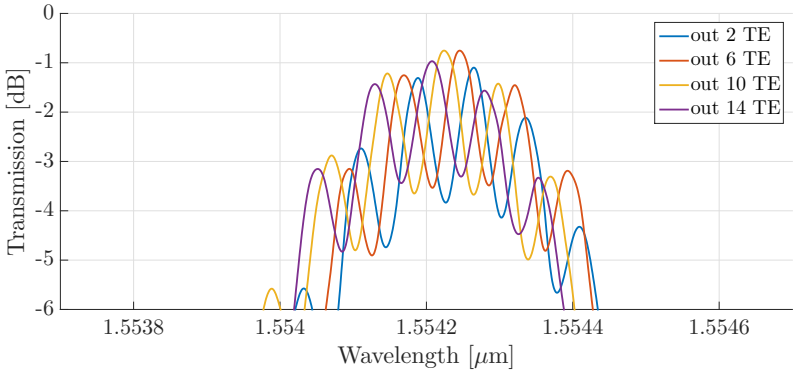

(c)

Figure 3.10: Measurement of four outputs with the same channel using the MZI at the input to test the relative phase. (a) General view and (b), (c), zooms of different channels.

3.4 Conclusions

Finally, as the chapter conclusions, a brief summary of the contents and goals attained follows. The general objective of this chapter, is to present the theoretical model and design procedure for the IC-AWG. This model is able to describe the three fold operation of the IC-AWG as channel demultiplexer, polarization splitter and 90° optical hybrid. The model has been used to provide a design procedure which is useful to obtain the necessary physical parameters of the device, from the targetted high level specifications or requirements, being possible obtain the response even in the case where two polarizations are supported by the waveguiding structures. Following the presented design procedure, an example of design and fabrication of an IC-AWG is reported. The device has been fabricated in the InP generic technology of the COBRA Research Institute through a MPW run. The IC-AWG features a chirp pattern P=4 with a targeted birefringence of 1.6 nm, therefore allowing to process simultaneously two optical channels with a channel spacing of 0.8 nm, the four different phase relations of a 90° optical hybrid and two polarizations each, obtaining 16 output waveguides.

From the measurements of the fabricated device, the birefringence obtained after fabrication does not correspond the simulated, having different focused channels at the output waveguides. Thus, the simulated wavelength map does not correspond with the one obtained from measurements. Moreover, some channels exhibit considerable pass-band degradation, that could be corrected using less aggressive layouts and input/output waveguide position corrections to minimize optical aberrations. The design of the device also includes a MZI in two inputs of the IC-AWG in order to check the different phases provided by each subarray. From the measurements of the transfer function of the joint MZI+IC-AWG, a good agreement with the necessary 90° optical hybrid operation is obtained.

The results in this chapter have been reported in different conferences and in one journal with the following publications:

- B. Gargallo and P. Muñoz, "Full field model for interleave-chirped arrayed waveguide gratings," *Optics Express*, vol. 21, no. 6, pp. 6928–6942, 2013.

- B. Gargallo and P. Muñoz, "Theoretical model of an interleave-chirped arrayed waveguide grating (IC-AWG)," in *Proc. SPIE 8767, Integrated Photonics: Materials, Devices, and Applications II*, paper 87670S, Grenoble, France, 2013.

- B. Gargallo and P. Muñoz, "Interleave-chirped arrayed waveguide grating theoretical model and design procedure," in *VIII Reunión Española de Optoelectrónica (OPTOEL)*, Alcalá de Henares, Madrid, 2013.

- B. Gargallo and P. Muñoz, "Interleave-chirp arrayed waveguide grating on InP generic technology," in *Proceedings of the 17th European Conference on Integrated Optics (ECIO)*, Nice, France, 2014.

Last but not least, the next intellectual property results have been registered related to the activities in this chapter:

- B. Gargallo, P. Muñoz, J. Capmany, and J.D. Doménech, "Espectrómetro óptico integrado en miniatura," OEPM P201331320 / ES2533610 - PCT/ES2014/070611, 2013.

Chapter 4
Reflective arrayed waveguide grating (R-AWG)

The present chapter is devoted to an Arrayed Waveguide Grating configuration which operates in reflective mode, and whose layout is amenable for tailoring the band pass shape. The chapter is sectioned as follows: first, the motivation of this device is introduced in Section 4.1. Then, in Section 4.2 the formulation of the regular AWG introduced in the previous chapters is used to explain the functionality of the R-AWG when different coupling constants and phase shifts are used in the arrayed waveguides. Next, in Section 4.3 an example of design, fabrication and characterization using the SOI technology presented in Chapter 2.4 is used as a proof of concept. In Section 4.4 new spectral responses using this configuration are explained as an outlook of the potential of the device. Finally, Section 4.5 is used to summarize and conclude the chapter.

4.1 Background and motivation

The fabrication cost of an integrated circuit is fundamentally related to its footprint [67, 68]. For integrated optics multiplexers, one of the most compact implementations is the Echelle Diffraction Grating (EDG) which achieves considerable size reduction in comparison with the AWG [69]. The EDG is composed of only one slab coupler (FPR in the AWG terminology of this thesis) with the input/output waveguides on one side, and a reflective grating and the end of the FPR. One of the crucial parts in the design of an EDG is the reflective grating, where maximum reflectivity is desired in order to avoid high losses in the device. Different approaches exist to increase the reflectivity of the grating as for example the deposition of metal layers at the edge of the grating [17] or the addition of Bragg reflectors [70]. However, additional fabrication processes are necessary, increasing the final cost.

Layouts for reflective AWGs exist as well. The functionality is the same than regular AWGs, but some extra design considerations are required [71]. Nonetheless, the reflectors can be implemented in multiple ways, as for example reflective coatings on the chip facet [14, 72], photonic crystals [73], external reflectors [74] and even Bragg reflectors [75] at the end of the arrayed waveguides. In [76] a R-AWG with a Sagnac Loop Reflectors (SLR) at the end of each arrayed waveguide is proposed. A SLR is composed of an optical coupler with two outputs, each connected to the other. When the coupler ratio is 50%, the device behaves as a folded Mach-Zehnder Interferometer, and all the light interferes constructively, but in reflection mode, rather than transmission.

In this chapter, the theoretical model for the analysis of the R-AWG, based on the model in [34], is presented. The model is then validated with the measurements obtained from a fabricated device. This device has been designed following the developed model and fabricated in a custom Silicon-On-Insulator (SOI) technology. Moreover, since the reflection of the SLR depends on the coupling constant of the coupler, a procedure to customize the spectral response of the R-AWG channels is provided. This customization of the field pattern in the arrayed waveguides allows to obtain different spectral shapes, as for example the flat-top response where every channel tends to be similar to a box-like transfer function [77]. Nonetheless, the tailoring of the spectral channels is not limited to the flat-top shape, and almost every shape could be obtained applying Fourier transform theory, as will be explained later on this chapter.

4.2 Operation principle

The schematic of a R-AWG is shown in Fig. 4.1. This figure will be used as reference for all the equations in this chapter. As in the case of the regular AWG, the R-AWG consists of a group of input/output waveguides, a free propagation region (FPR) and a group of arrayed waveguides, but now the arrayed waveguides are terminated with a reflector, implemented by means of a Sagnac Loop Reflector (SLR). Note that the schematic also includes a phase shifter (PS) in each arm, the purpose of which will be detailed later on.

The operation is similar to the case of the regular AWG, as described in detail in Chapter 2.2. The only difference in layout is the presence of the reflectors at midway in the arms of the AWG. Hence, each arrayed waveguide is terminated with a SLR where the amplitude and phase of the signal can be modified through the coupling constant of the coupler and the phase shifter, respectively. The overall phase and amplitude relations between the arrayed waveguides will determine the spectral shape and the behavior of the R-AWG, being the most simple case when only a constant phase difference is introduced between consecutive arrayed waveguides. Thus, the response is similar to the regular AWG where different wavelength channels will be focused to different output waveguides.

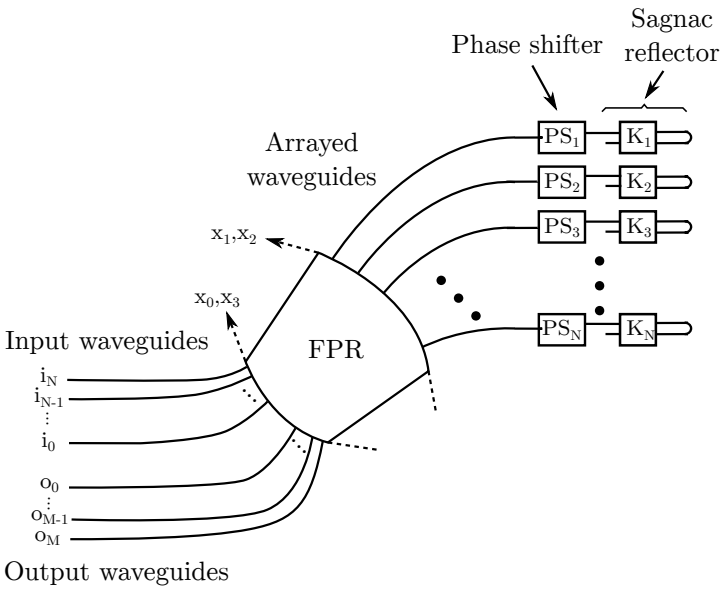

Figure 4.1: R-AWG schematic view. Abbreviations: FPR free propagation region, PS phase shifter, K coupling constant, x_i (i=0,1,2,3) are reference coordinates and i_j, o_j are input and output waveguides, respectively.

4.2.1 The Sagnac Loop Reflector (SLR)

The Sagnac Loop Reflector (SLR) is depicted schematically in Fig. 4.2-(a). Basically, it consists of a coupler with the output waveguides bypassed. The transfer matrix for the coupler can be expressed as:

$$\begin{pmatrix} o_0 \\ o_1 \end{pmatrix} = \begin{pmatrix} \sqrt{1-K} & j\sqrt{K} \\ j\sqrt{K} & \sqrt{1-K} \end{pmatrix} \begin{pmatrix} i_0 \\ i_1 \end{pmatrix} \tag{4.1}$$

where K is the coupling constant and i, o stand for input and output waveguides, respectively. Hence, it is possible to analyze the SLR as two couplers connected in a series, as in Fig. 4.2-(b). Then, the response of the SLR will be:

$$\begin{cases} o'_0 = 2j\sqrt{(1-K)\,K}e^{-j\beta L}i_0 + (1-2K)\,e^{-j\beta L}i_1 \\ o'_1 = (1-2K)\,e^{-j\beta L}i_0 + 2j\sqrt{(1-K)\,K}e^{-j\beta L}i_1 \end{cases} \tag{4.2}$$

and for the case where only the input i_0 is used, the transfer functions can be simplified as:

$$\begin{cases} o'_0 = 2j\sqrt{(1-K)\,K}e^{-j\beta L}i_0 \\ o'_1 = (1-2K)\,e^{-j\beta L}i_0 \end{cases} \tag{4.3}$$

being the β parameter the propagation constant of the waveguide mode, defined as $\beta = k_0 n_c = 2\pi n_c \nu / c$, where n_c is the waveguide effective index, k_0 is the wavenum-

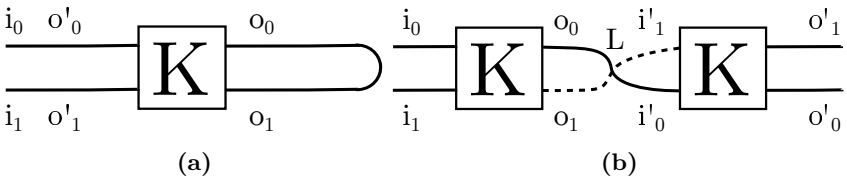

Figure 4.2: Sagnac Loop Reflector (a) and SLR analysis as two serial couplers (b). Abbreviations: i and o stand for input and output waveguides, respectively. K stands for coupling constant and L stands for loop length.

ber, ν is the frequency and c is the speed of light in vacuum. In these equations, the phase change due to the length of the loop L has been included. From these expressions, total reflection in port i_0 will be obtained when the coupling constant is set to $K = 0.5$. This coupling constant parameter is very important when tailoring the spectral response of the AWG, as will be analysed in Sec. 4.4, since coupling constants K other than 0.5 will be traduced in reflected power less than 100%.

In the SLR, the coupler could be implemented in multiple ways, as for example directional couplers [78], wavelength insensitive couplers [79] or multimode interference couplers (MMIs) [80]. Since the reflectors in the R-AWG are necessary to be broadband, with a K parameter constant over a wide range of wavelengths, and the footprint is critical, multimode interference couplers are envisaged as the ones fulfilling all the requirements. Moreover, MMIs can be designed with arbitrary couplings constants [81,82] or to be tunable [83]. However, different coupling constants will result in different MMI lenghts and phase shifts. This is the reason to include phase shifter (PS) sections in the arrayed waveguides of the R-AWG, where it is necessary to compensate the phase imbalances due to different coupling constants. In this way, one of the requirements of the PS is to be broadband as the coupler. Different implementations can be possible, being the most simple the use of regular straight waveguides or tapered waveguides as in [84].

4.2.2 Formulation

In a regular AWG, the phase shift ($\Delta\phi$) between consecutive waveguides in the array is an integer number m times 2π when the central wavelength is used. In the R-AWG of Fig. 4.1, the phase shift can be divided between the arrayed waveguide ($\phi_{w,i}$), the phase shifter ($\phi_{PS,i}$) and the Sagnac loop reflector ($\phi_{SLR,i}$), being i the number of the waveguide. Then, the total phase shift in each AW will be given by $\phi_i = \phi_{w,i} + \phi_{PS,i} + \phi_{SLR,i}$. Since the R-AWG has the same layout as the AWG, formulation introduced in Chapter 2.2 is taken as the basis to develop its equations. The first difference lies in the phase shift introduced by the AWs, so until Eq. (2.3) formulating the field in the plane x_1, all the formulation will be the same. Then, the length of the waveguide number r will be given by $l_r = l_0/2 + \Delta l/2\,(r + N/2)$, where $l_0/2$ is the base length of the shortest waveguide in

the array. As was previously discussed, the incremental length between AWs will be set to an integer multiple m of times 2π when using the central wavelength λ_0, resulting in $\Delta l = m\lambda_0/n_c$ where n_c is the effective index from the AWs. Thus, the phase shift due to the waveguide will be $\Delta\phi_r = \beta l_r = 2\pi n_c \nu l_r/c$, where β is the propagation constant of the mode in the waveguide. Both the PS and the SLR introduce an additional phase shift, and the SLR also an amplitude change. Along with all this, the reflected field from the AWs at the planse x_2, which is equivalent to the plane x_1 in the R-AWG (see Fig. 4.1), will be:

$$f_2(x_2,\nu) = \sqrt[4]{2\pi\omega_g^2}\left[\prod\left(\frac{x_2}{Nd_\omega}\right) B_i(x_2)\,\phi(x_2,\nu) \sum_{r=-\infty}^{+\infty} \delta(x_2 - rd_\omega)\, e^{-2j\psi_{PS,r}(\nu)} j a_r e^{-j\beta l_{SLR,r}}\right] \otimes b_g(x_2) \tag{4.4}$$

where a_r is the SLRs amplitude term given by $a_r = 2\sqrt{(1-K_r)\,K_r}$ obtained from Eq. (4.3), K_r is the SLR coupling constant, $\psi_{PS,r}(\nu)$ is the phase shift introduced by the PS and $l_{SLR,r}$ is the length of the loop waveguide within the SLR. The phase term $\phi(x_2,\nu)$ is:

$$\phi(x_2,\nu) = \psi(\nu)\, e^{-j2\pi m \frac{\nu}{\nu_0}\frac{x_2}{d_\omega}} \tag{4.5}$$

$$\psi(\nu) = e^{-j2\pi\nu\left(\frac{n_c l_0}{c} + \frac{m_N}{2\nu_0}\right)} \tag{4.6}$$

Finally, to obtain the field at the plane x_3 the spatial Fourier transform will be used to the field coming from each AW. This result in:

$$f_3(x_3,\nu) = \mathcal{F}\{f_2(x_2,\nu)\}\big|_{u=\frac{x_3}{\alpha}} \tag{4.7}$$

Contrary to the previous model in [34], no closed analytical solution is possible to be calculated in the general case, due to the arbitrary phase shift for each AW. Nonetheless, the previous equation is the basis for the particular cases derived in the next paragraphs. Independently, the frequency response at the output waveguide q can be calculated through the following overlap integral:

$$t_q(\nu) = \int_{-\infty}^{+\infty} f_3(x_3,\nu)\, b_0(x_3 - qd_o)\,\partial x_3 \tag{4.8}$$

where d_o is the spacing between, and $b_0(x_3)$ is the field profile of the output waveguides.

4.2.3 Gaussian spectral response

The most simple case for the R-AWG will be when a regular AWG response is desired. In this case, all the SLRs will be the same, with total reflection and,

therefore, coupling constant $K = 0.5$. Moreover, the phase shifters are not required in this configuration, as was reported experimentally in [76]. To this case, the equations can be particularized, and Eq. (4.4) can be rewritten as:

$$f_2(x_2,\nu) = j\sqrt[4]{2\pi\omega_g^2}e^{-j\beta l_{SLR}}\left[\prod\left(\frac{x_2}{Nd_\omega}\right)B_i(x_2)\,\phi(x_2,\nu)\sum_{r=-\infty}^{+\infty}\delta(x_2-rd_\omega)\right]\otimes b_g(x_2) \tag{4.9}$$

and the field at the output plane (x_3) described using Eq. (4.7) as:

$$f_{3,p}(x_3,\nu) = j\sqrt[4]{2\pi\frac{\omega_g^2}{\alpha^2}}B_g(x_3)\,e^{-j\beta l_{SLR}}\psi(\nu)\sum_{r=-\infty}^{+\infty}f_M\left(x_3+pd_i-r\frac{\alpha}{d_\omega}+\frac{\nu}{\gamma}\right) \tag{4.10}$$

where the different terms therein are given by Fourier transforms as in Chapter 2.2, $f_M(x_3)$ is defined as $\mathrm{sinc}(Nd_\omega x_3/\alpha)\otimes b_i(x_3)$ and the equations have been taking into account an input waveguide p placed at a distance pd_i from the center position, where d_i is the distance between input waveguides. As a conclusion, the field at the output plane for this particular R-AWG can be described as the same way of the Gaussian AWG presented in Chapter 2. Note that in the case of the R-AWG the positioning of the input/output waveguides has implications for the selection fo the central design wavelength. However, this can be accounted for during the design process as described in [71]. The dispersion angle (θ) with respect to the center of the slab coupler is given by [7]:

$$\theta = \arcsin\left(\frac{\beta\Delta l - m2\pi}{\beta_S d_\omega}\right) \tag{4.11}$$

where β and β_S are the propagation constants of the AW mode and slab modes, respectively, and d_ω is the spacing between AWs. For the positioning of the input/output waveguides in the R-AWG, the wavelength routing properties of the AWG need to be observed [8]. If $\lambda_{p,q}$ is the wavelength routed from the input waveguide p to the output waveguide q, if the input position is changed for instance to $p-p'$, the same wavelength $\lambda_{p,q}$ will be routed to output $q+q'$, with $p'=q'$ provided the positions of the input/outputs corresponds to the same wavelength displacement given by the derivative of Eq. (4.11) (see [7]). Figure. 4.1 shows a layout for N inputs and M outputs, accounting for these routing properties. The central input waveguide $p=0$ is placed a distance to the left from the center of the slab. Therefore, the central output waveguide $q=0$ needs to be placed the same distance to the right from the center. Nonetheless, the input and output waveguides can be placed in any configuration in the slab coupler, as for example interleaving one input with one output waveguide, as long as Eq. (4.11) is taken into account to calculate the combination of wavelengths/positions.

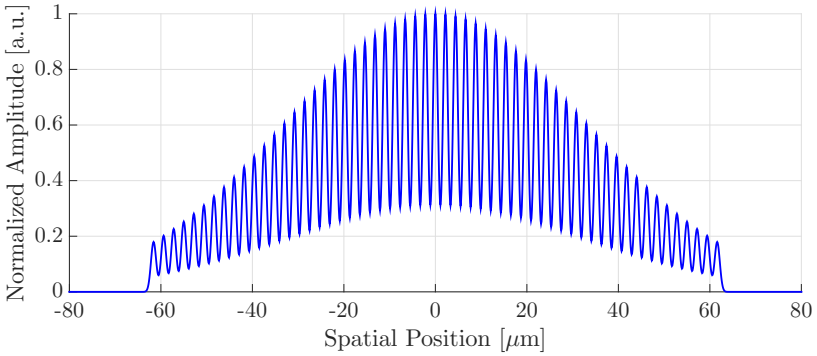

(a)

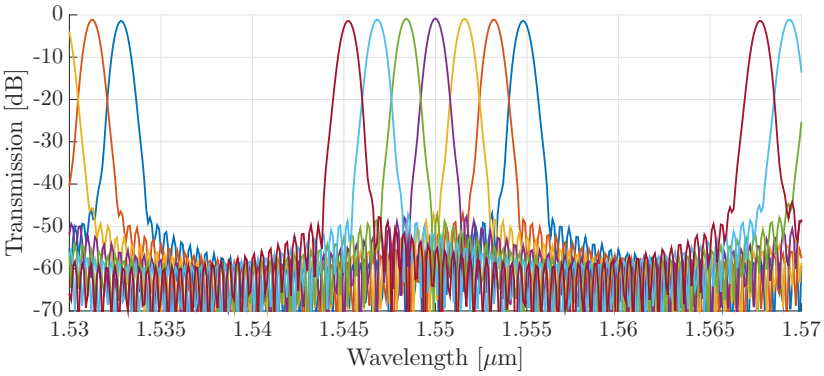

(b)

Figure 4.3: Gaussian R-AWG simulation with 1 input and 6 outputs. (a) Field at the arrayed waveguides. (b) Transfer function from i_0 to the output waveguides.

4.3 Design, fabrication and characterization

The model developed in Sec. 4.2 is used then to design, simulate and fabricate a R-AWG, similar to previously validated models [48, 49]. Despite AWGs and SLRs can be implemented in almost all integration technologies [2], the footprint advantage will be obtained in those where the bend radius can be small and, therefore, confinement in the optical waveguide is strong. Amongst the different integration technologies, the smallest bend radius is for Silicon-on-Insulator (SOI), where it can be lower than 5 μm. For this reason, the fabrication of the devices have been performed in SOI by AMO GmbH, the same technology presented in Chapter 2.4. The input/output waveguides are designed to use a 2.0 μm width shallowly etched cross-section. For the AWs, 0.8 μm width deep waveguides are used to minimize phase errors [47]. The effective index for these cross-section n_c will be 2.67 for TE polarization, obtained from simulations using a commercial

software [50]. Then, this straight section of the AWs is tapered down to 0.45 μm width in the bent sections, where a radius of 5 μm can be used. Finally, an effective index n_s of 2.83 is obtained in the slab coupler also for TE polarization. Even when all the equations derived in the previous sections can be used for both TE and TM polarizations, all the simulations performed in this section are for TE polarization. The reason of doing this is due to the fact that most of the SOI chips employ grating couplers as input/output structures, and they usually support only a single polarization [51, 52]. It is also possible to find in the literature grating couplers coupling both polarizations from the fiber [53], however both polarizations are coupled as TE polarization into the chip. The only possibility then to couple TM polarization on-chip is butt-coupling the light horizontally in the devices, but this is not the case of this design where grating couplers will be used.

4.3.1 Design and simulation

For the design of the R-AWG, the central wavelength is 1550 nm. The number of channels is 7, the channel spacing is set to 1.6 nm (200 GHz) and the FSR has been chosen to be 22.4 nm. With these parameters, the calculated focal length is 189.32 μm, the incremental length between AWs will be 36.03 μm and the number of AWs is 49. This design has been thought to have one single input waveguide i_0 placed at the central position of the slab coupler. Then, the output waveguides are located at both sides of this central input waveguide. Note that due to the reflective nature of the R-AWG, the central input waveguides will be also used as an output waveguide, since the central channel will be reflected to this input/output. The reason for using an input waveguide located at the central position is that in the case the input waveguide is displaced from the center, it is necessary to apply additional tuning techniques to compensate the non-uniformities that arise due to the use of a Rowloand mounting as input/output plane. For example, one of these techniques could be the modification of the angle and/or positions of the input/output waveguides [55].

This R-AWG is then simulated for a Gaussian response. As has been described in Sec. 4.2.3, it is not necessary to include the phase shifters in each arm since all the SLRs have been designed to have total reflection, i.e. with identical coupling constant $K = 0.5$. Figure 4.3-(a) shows the Gaussian field distribution at the plane x_2 obtained as the summation of all the AW contributions through Eq. (4.9) and the total transfer function is depicted in Fig. 4.3-(b). From simulations, the insertion losses are approximately 1 dB for the central channel and less than 1.5 dB for the outer channels. Note that this simulation shows the ideal response of the R-AWG, since propagation losses and other detrimental effects as fabrication imperfections have not been included. As comparison, the typical insertion losses per channel of a regular SOI AWG are around 4-5 dB [47]. From the simulation the 1-dB, 3-dB and 20-dB bandwidths are 0.39 nm, 0.65 nm and 1.58 nm, respectively.

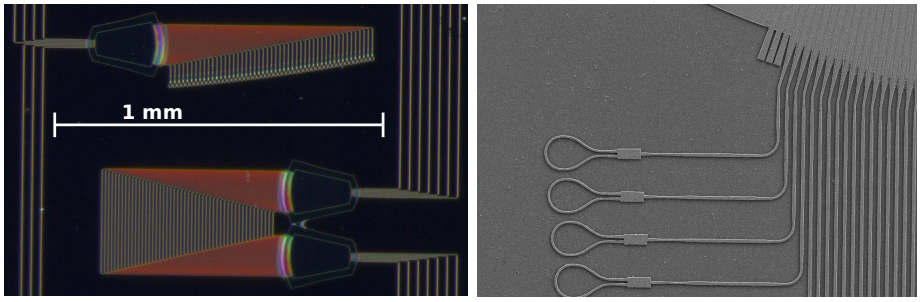

(a) (b)

Figure 4.4: Pictures of the fabricated device: (a) Optical microscope image of the R-AWG and (b) image of the detail of the SLR using a scanning electron microscope (SEM).

4.3.2 Device fabrication and characterization

Following the developed model and methodology, regular and reflective AWGs with the aforementioned parameters have been fabricated on the SOI substrates presented before. Measurements from the regular AWG can be found in Chapter 2.4. From these fabricated devices, a microscope image can be seen in Fig. 4.4, obtaining a footprint for the orthogonal AWG of approximately 400×800 μm^2 (width×height), while for the R-AWG is 230×900 μm^2. As has been mentioned early in this chapter, the size of the R-AWG is almost half the size of the regular AWG. The reason for not obtaining exactly half the size of the regular AWG lies on the loop bypassing the SLR outputs, since even with the minimum bending radius it is necessary to increase the distance between AWs.

The chip is placed then in a copper submount and is thermally controlled to 25°C using a TEC. A broadband source (C&L Band ASE source, NP Photonics) has been used at the input waveguide, and measurements are recorded using an Optical Spectrum Analyzer (OSA YOKOGAWA AQ6370C) with 10 pm resolution. To estimate the insertion losses in the AWG, all the traces are normalized with respect to a 0.8 μm width deep straight waveguide. Figure. 4.5-(a) shows the measurements for the three inner channels when entering using the central waveguide. It is possible to obtain the response from the other three output waveguides although it could not be possible with the available measurement setup since they end in the same side of the chip than the central input. Figure 4.5-(b) shows a comparison between the three measured channels of the R-AWG and the corresponding channels in the regular AWG presented in Chapter 2.4. From this comparison, two main degradations can be observed in the R-AWG. The first one is related with the channel width, as in the R-AWG the shape of the band pass is degraded towards longer wavelengths, obtaining a broadening of the channel at 6 dB below the channel peak maximum. The second is the increased side lobe level. In the case of the AWG, this lobe level is as high as 13 dB below the channel

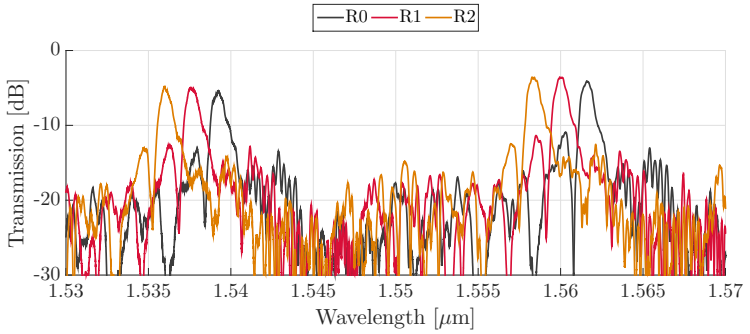

(a)

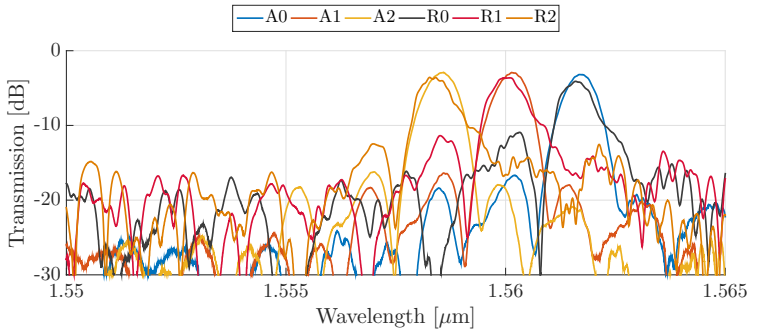

(b)

Figure 4.5: Measured spectral traces from the (a) R-AWG and (b) comparison with the regular AWG presented in Chapter 2.4.

peak, while in the R-AWG it is only 8 dB below. Since the only difference between both devices is the presence of SLRs, these degradations may be attibuted to phase/amplitude errors due to the reflectors. In this way, not only sidewall roughness can be a source of errors, but also the aforementioned grid snapping. The SLRs are placed in positions that have not been adapted to the 5 nm grid snapping, so the MMI bodies (width and length) may differ by ± 5 nm, leading to a phase error of $\pm\pi/54$. Moreover, the additional bent section as a loop in the SLR will be more sensitive to the effect of mask discretization. Both effects could be then the cause of the worse performance for the R-AWG when comparing with a regular AWG.

To verify the expected higher phase errors in the AWs, the OFDR technique has been used to measure the power and phase of each AW independently, as in Chapter 2. Measurements can be seen in Fig. 4.6 where panel (a) shows the power distribution that does not follow the simulated Gaussian shape. Moreover, panel (b) shows that for the R-AWG the phase errors are as high as 2 radians. These power imbalance and phase errors are higher than for the regular AWG

desing, where the power distribution follows the simulated Gaussian shape and a maximum error of 1 radian is obtained from the OFDR measurements. As has been mentioned, the only reason for the higher phase errors in the R-AWG case is the use of SLR that could be more sensitive to the effects of fabrication and mask discretization.

Despite this, several design techniques can be applied to improve the performance for the R-AWG, as for example adapting the SLR lengths, widths and positions to the grid or increasing the bending radius to minimize the discretization effect.

4.4 Flattened and arbitrary spectral responses

The following section presents how to tailor the spectral response of the AWG. It was previously published in a peer reviewed journal, and is reprinted here with permission: B. Gargallo, P. Muñoz, R. Baños, A.L. Giesecke, J. Bolten, T. Wahlbrink, and H. Kleinjans, "Reflective arrayed waveguide gratings based on Sagnac loop reflectors with custom spectral response," *Optics Express*, vol. 22, no. 12, pp. 14348–14362, © 2014 OSA, `dx.doi.org/10.1364/OE.22.014348`.

4.4.1 Flattened response

There are different techniques to flatten the spectral response of an AWG, amongst them the use of parabolic waveguide horns [85], MMIs [38] and interferometers [86] at the input/output waveguides. Other technique proposes the modification of the amplitude and phase in the AWs to obtain a sinc field profile [77]. The latter builds upon the signal theory duality between fields at both sides of the slab coupler, through the (spatial) Fourier transform. To obtain a box like field pattern at the output side of the slab coupler, through the diffracted (the Fourier transform) field, a sinc distribution is required in the AWs [77, 87]. As mentioned in the introduction, the SLR based R-AWG layout allows for the modification of the phase front by means of the phase shifters, while the amplitude can be adjusted by means of the SLRs. Recall the Fourier transform of a Π function is:

$$\mathcal{F}\left\{\prod\left(\frac{x}{A}\right)\right\}\Big|_{u=\frac{y}{\alpha}} = A\text{sinc}\left(A\frac{y}{\alpha}\right) \tag{4.12}$$

where A is the rectangular width, and x, y the spatial variables. Therefore, the field at the plane x_2 will be modified to adjust it to a sinc function as described in [87]. In the formulation, the adjustment can be incorporated by the terms in Eq. (4.4), to be precise $2j\sqrt{(1-K_r)\,K_r}e^{-j2\psi_{PS,r}(\nu)}e^{-j\beta l_{SLR,r}(\nu)}$, from which the following amplitude and phase conditions are derived to turn the input far field Gaussian profile $B_i\,(x_2)$ into a sinc function. Hence, the amplitude condition is written as follows:

$$B_i\,(rd_w)\,\sqrt{(1-K_r)\,K_r} = |\text{sinc}\,(ard_\omega/\alpha)| \tag{4.13}$$

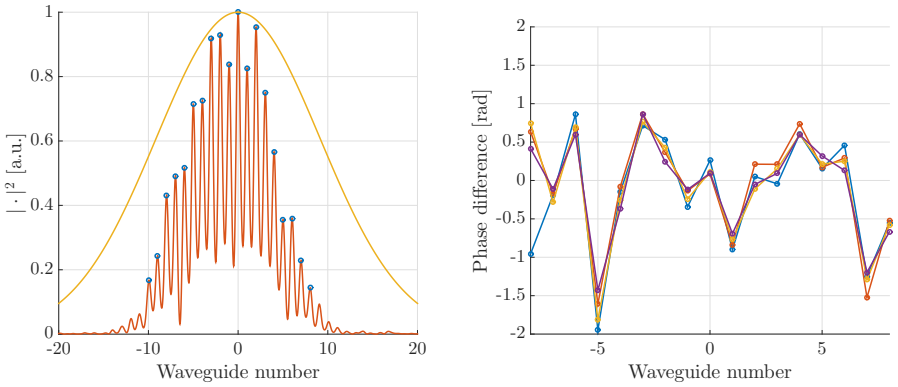

(a) **(b)**

Figure 4.6: Measurement of the R-AWG using the OFDR technique: (a) power and (b) phase errors in the arrayed waveguides.

where a will be the obtained rectangular function width when using the Fourier transform, as is detailed below. In addition, the following phase condition is required to turn the all positive values from the input far field Gaussian into negative (π shift) where needed:

$$2\psi_{PS,r}(\nu) + \beta l_{SLR,r} = \begin{cases} 0, & \text{if } \frac{2n\alpha}{a} \leq |rd_\omega| \leq \frac{(2n+1)\alpha}{a} \\ \pi, & \text{otherwise} \end{cases} \quad \text{with n=0,1,...} \tag{4.14}$$

Under these conditions, the sinc field profile for the AWs can be introduced in Eq. (4.4) for x_2, resulting in:

$$f_2(x_2,\nu) = j\sqrt[4]{2\pi\omega_g^2}\left[\prod\left(\frac{x_2}{Nd_\omega}\right)B_i(x_2)\,\phi(x_2,\nu)\cdot \sum_{r=-\infty}^{+\infty}\delta(x_2 - rd_\omega)\,\mathrm{sinc}\left(a\frac{rd_\omega}{\alpha}\right)\right] \otimes b_g(x_2) \tag{4.15}$$

Finally, the field at the plane x_3 calculated through the spatial Fourier transform of Eq. (4.15) is given by:

$$f_{3,p}(x_3,\nu) = j\sqrt[4]{2\pi\frac{\omega_g^2}{\alpha^2}}B_g(x_3)\,\psi(\nu)\sum_{r=-\infty}^{+\infty} f'_M\left(x_3 + pd_i - r\frac{\alpha}{d_\omega} + \frac{\nu}{\gamma}\right) \tag{4.16}$$

where $f'_M(x_3)$ is in this case:

$$f'_M(x_3) = \mathrm{sinc}(Nd_\omega x_3/\alpha) \otimes (\alpha/a)\prod(x_3/a) \tag{4.17}$$

Eq. (4.17) describes the field shape at the output plane, being the second term in the equation the obtained rectangular profile from the sinc field distribution in the AWs.

In general, there is a trade-off between the desired channel flatness and the acceptable channel width increase, which is inversely proportional to the number of zeros of the sinc field distribution in the AWs. Furthermore, the use of a more "compressed" sinc will reduce the amplitude of the obtained dual rectangular function, i.e. the AWG will have a flatter response, but with more peak insertion loss.

Using the same physical parameters as in Section 4.3, but for a R-AWG with sinc field distribution in the AWs, the transfer function is computed resulting in a flattened spectral response. A sinc profile with a = 12 μm is incorporated. From this distribution, the required coupling constant K_r for each SLR is calculated using Eq. (4.13). Note the use of a different coupler in each AW may introduce a different phase shift in each arm [82], as already mentioned. For simplicity, this phase shift has not been included in Eq. (4.14) since it can be compensated through the phase shifters. Figure 4.7-(a) shows the field distribution at the plane x_2, being this field the summation of all the AW contributions in blue trace. On the same figure, the sinc function applied is shown in green line. Moreover, the secondary axis shows in red crosses the required coupling constant for each SLR to obtain the sinc profile.

As described above, to obtain a wider rectangular function, a more compressed sinc function at the AWs is required. However, widening comes at the expense of increased channel insertion loss. This can also be understood by comparing Fig. 4.3-(a) and Fig 4.7-(a), from which is clear the sinc field distribution is attained in part by modifying the amplitude of the original Gaussian field distribution, with partial reflectors, i.e. some signal is lost. The transfer function for the flat-top R-AWG is shown in Fig. 4.7-(b). The flat spectral response and increased insertion losses are clearly noticeable by comparing these results with Fig. 4.3-(b). The obtained losses in this case are 6.2 dB and 6.8 dB for the central and side channels respectively. The bandwidths at the points of interest are in this case 1.12 nm, 1.50 nm and 2.53 nm, for 1-dB, 3-dB and 20-dB fall from the channel center. As expected, an increase in the channel bandwidth is attained at the expense of more insertion losses. Note the closer these values are, the better (more box shapped) is the response. At the sight of all the above, a variation of the sinc field distribution in the AWs may be found numerically to that purpose. Finally, the lateral channels shape appears slightly degraded compared to the central channels. This can be corrected by optimizing its positions with respect to the canonical Rowland circle, as described in [55].

4.4.2 Arbitrary spectral responses

Although the semi-analytical model in previous sections was only derived for the Gaussian and flattened response cases, in principle it is possible to apply any desired field distribution for the AWs, which will result in different spectral responses.

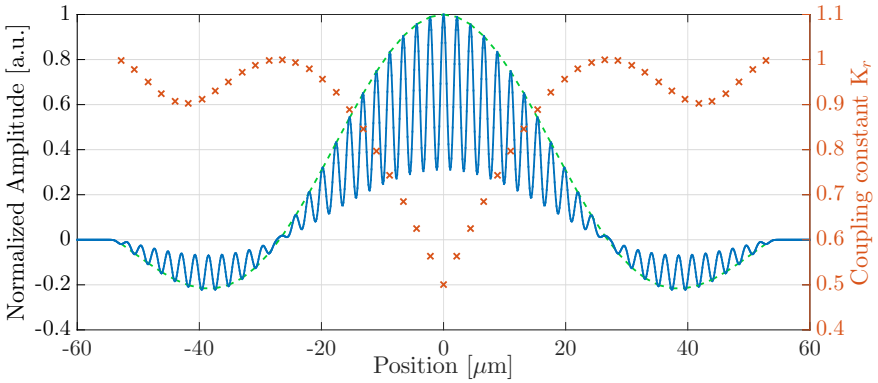

(a)

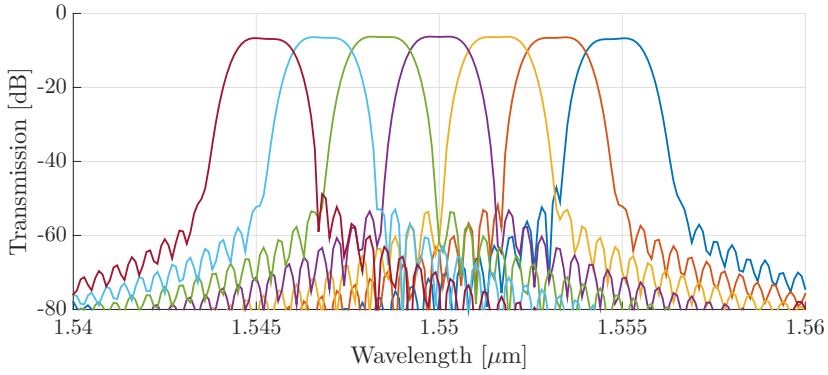

(b)

Figure 4.7: Flat-top R-AWG using a sinc field distribution at the arrayed waveguides. (a) Field at the arrayed waveguides (blue solid), the sinc profile applied (green dashed) and SLR coupling constant k_r in each arm of the array (red crosses). (b) Transfer function from i_0 to the output waveguides. (Both for a sinc distribution with parameter a=12.0μm).

In this subsection we present several field distributions and corresponding spectral responses, which we take from well-known Fourier transform pairs. To be precise, we targeted triangular, decaying exponential, truncated cosine and Lorentzian spectral responses. The mathematical expressions for these functions are listed in Table 4.1. Hence, Fig. 4.8-(a) shows the required AWs field distributions, i.e. at plane x_2. Note the legend labels are for the target transform pair, not the actual function employed in the field distribution for the AWs. Detailed expressions can be found elsewhere, as for instance in [88].

Similar to the previously shown case for the flattened response (AWs sinc distribution), the required coupling factors K to be applied in each AW are shown

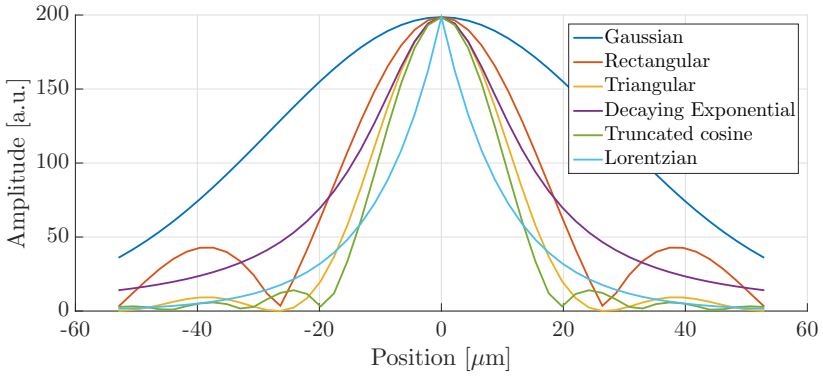

(a)

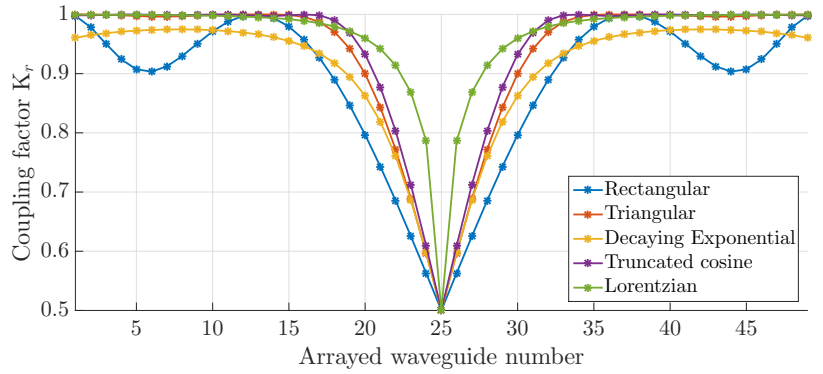

(b)

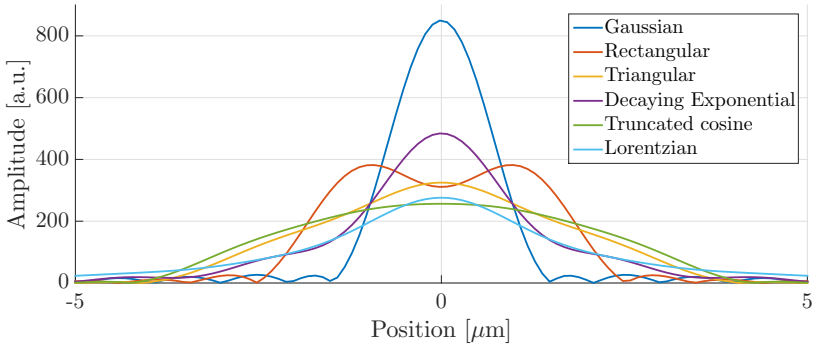

(c)

Figure 4.8: (a) Field profiles at the AWs and (b) necessary coupling constants to obtain different pass-band shapes (c) at the output plane.

Function	Target response	AWs field distribution	a parameter
Rectangular	$\prod(x/a)$	$a\mathrm{sinc}(ay)$	12.0 μm
Triangular	$\Lambda(x/a)$	$a^2\mathrm{sinc}^2(ay)$	12.0 μm
Decaying exponential	$e^{-\lvert ax\rvert}$	$2\lvert a\rvert / \left(\lvert a\rvert^2 + (2\pi y)^2\right)$	2.5 μm
Truncated cosine	$\cos\left(\frac{\pi x}{a}\right)\prod\left(\frac{x}{a}\right)$	$\frac{a}{2\pi}\left[\frac{\cos(\pi y a)}{\left(\frac{1}{2}\right)^2-(ya)^2}\right]$	8 μm
Lorentzian	$\frac{1}{\pi}\frac{0.5a}{x^2+(0.5a)^2}$	$e^{-a\pi\lvert y\rvert}$	3.0 μm

Table 4.1: Mathematical Fourier transform pair expressions.

in Fig. 4.8-(b). Note there is no plotted value for the Gaussian case, since all the SLRs use $K = 0.5$ for full reflection. An additional important remark is how the regular Gaussian field distribution ingoing to the array is transformed into the targeted one. In principle some field distributions, can have amplitudes higher than those of the Gaussian for some of the waveguides in the array. This would require amplification, which is not contemplated with the proposed SLR-based layout. Therefore, the targeted profile needs to be inscribed under the starting Gaussian profile. Hence, the amplitude in each AW needs to be reduced to inscribe the profile inside the Gaussian, at the cost of more insertion losses. This is the result in Fig. 4.8-(a), where all the field profiles at the AWs have amplitude levels below the starting Gaussian distribution.

The flat spectral response case, developed in Section 4.4.1, shows the shape of the field at the output plane given by Eq. (4.17). For all the targeted spectral responses, this far field at the output plane is plotted in Fig. 4.8-(c) for λ_0. The far field is not exactly the Fourier transform pair of the AWs field distribution in Fig. 4.8-(a). As expressed in Eq. (4.17), the field profiles at x_2 have a finite extensions (i.e. a finite number of AWs is employed), therefore the field profiles are truncated and the far field is in fact the convolution between a sinc function (Fourier transform of a truncation function in the array) and the Fourier transform of the profile applied at the AWs. From all the curves in Fig. 4.8-(c) the triangular function case (red line) is the most suitable to understand this fact. Ideally, for an infinity (unpractical) number of AWs, one would expect a perfect (sharp) triangular shape, but in practice the truncation by a finite number of waveguides results in some smoothing in the curves.

In addition to this intrinsic smoothing, the corresponding end-to-end transfer functions for the R-AWGs involves the calculation of the convolution integral between the (already smoothed) far field at the output plane and the mode at the output waveguide, as described by Eq. (4.8). The transfer functions are depicted in Fig. 4.9, using linear units, for the output waveguide o_3, placed at the center of the slab coupler.

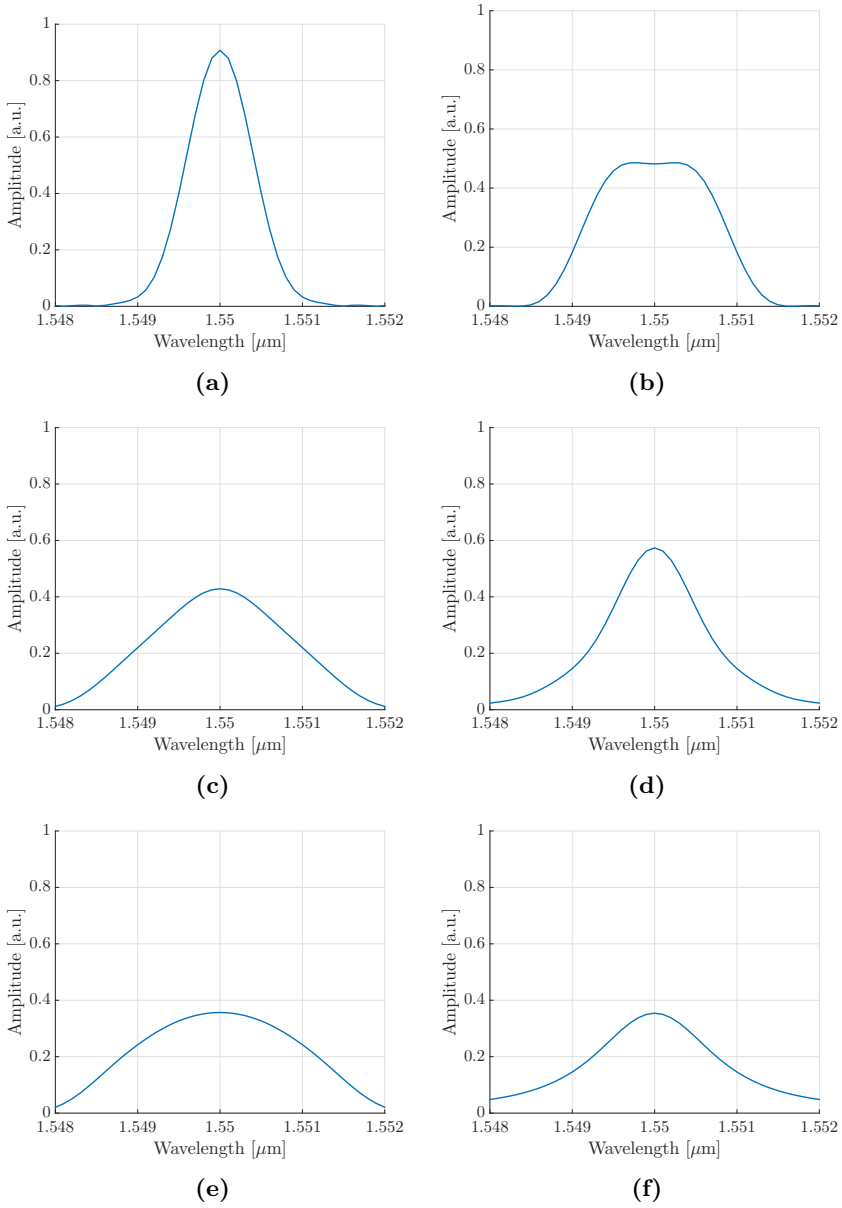

Figure 4.9: Transfer function (linear) in one output waveguide for each different profile applied: (a) Gaussian, (b) rectangular, (c) triangular, (d) decaying exponential, (e) truncated cosine and (f) Lorentzian functions.

4.5 Conclusions

The R-AWG using SLR as reflectors at the AWs has been proposed and analyzed in this chapter. This layout, in its most basic form without phase shifters and similar reflectors in each arm, can perform in tha same way than a regular AWG. As an advantage, the size is dramatically reduced, obtaining an improvement in the cost per device. Moreover, the use of phase shifters and tunable couplers enables the control of the field amplitude and phase per arm, obtaining the possibility of tailoring the spectral shape of the R-AWG pass-band channels. For this reason, a theoretical model for the analysis and design of the R-AWG is provided in this chapter. The validity of this model has been checked by means of the comparison of a regular AWG and a R-AWG fabricated in the same chip. Even though both AWGs perform in the same way in terms of channel spacing, FSR and central wavelength, several degradations are observed in the R-AWG compared with the AWG. Possible error sources are discussed through the chapter, being the fabrication problems and the grid snapping that causes differences between arms the most likely.

As a chapter outlook, different spectral shapes using the phase shifters and the variable couplers in AWs are presented. For completeness, an example of use of the sinc function AW field distribution to obtain a box-like pass-band shape is provided. This sinc function in the AWs will be introduced by means of the combination of phase shifters and SLRs whose reflectivity is set through the coupling constant of te optical coupler. Moreover, different field profiles to apply in the AWs to obtain different tailored pass-band shapes are provided.

The contents of the chapter have been published in the following journals and conferences:

- B. Gargallo, P. Muñoz, R. Baños, A.L. Giesecke, J. Bolten, T. Wahlbrink, and H. Kleinjans, "Reflective arrayed waveguide gratings based on Sagnac loop reflectors with custom spectral response," *Optics Express*, vol. 22, no. 12, pp. 14348–14362, 2014.

- B. Gargallo, P. Muñoz, R. Baños, A.L. Giesecke, J. Bolten, T. Wahlbrink, and H. Kleinjans, "Reflective Arrayed Waveguide Grating with Sagnac Loop Reflectors in Silicon-on-Insulator with Gaussian Pass-band," in *Proceedings of the 17th European Conference on Integrated Optics (ECIO)*, Nice, France, 2014.

- B. Gargallo, P. Muñoz, R. Baños, A.L. Giesecke, J. Bolten, T. Wahlbrink, and H. Kleinjans, "Silicon-on-insulator reflective arrayed waveguide grating with sagnac loop reflectors," in *Proceedings of the 40th European Conference on Optical Communication (ECOC)*, Cannes, France, 2014.

- B. Gargallo, P. Muñoz, and R. Baños, "Reflective Arrayed Waveguide Grating in Silicon-on-Insulator with flattened spectral response," in *Proceedings of the 19th Annual Symposium of the IEEE Photonics Benelux Chapter*, Enschede, The Netherlands, 2014.

- P. Muñoz, B. Gargallo, G. Micó, D. Pastor, and A. Ortega-Moñux, "Reconfigurable integrated optics spectrometer," in *Photonics North 2015*, Ottawa, Canada, 2015.

Last but not least, two intellectual property results have been registered related to the activities in this chapter:

- B. Gargallo, P. Muñoz, J. Capmany, and J.S. Fandiño, "Dispositivo AWG reflectante con respuesta espectral configurable implementado con reflectores de Sagnac," OEPM P201331792 / ES2540378 - PCT/ES2014/070782, 2013.
- B. Gargallo, P. Muñoz, D. Pastor, and G. Micó, "Integrated Optics Sensing Spectrometer (IOSS)," ref. R-17050-2014, 2014. Spanish patent being filed at the time of writing this thesis.

These were attempted in the late stages of the thesis, and their experimental validation is left to be attempted in future research.

Chapter 5
Wavelength scanning AWGs using Surface Acoustic Waves

Along the realization of this PhD thesis, different AWG funciontalities have been subject of research. In this chapter, the combination of Surface Acoustic Waves (SAW) and an adapted design of a regular AWG, for continous multi-channel wavelength scanning is presented.

5.1 Introduction

In a regular AWG, as discussed in the previous chapters, the incremental length between the AWs provides a wavelength-dependent linear phase front. As a result, the combination of this phase front with a free propagation region results into the focusing of different wavelengths to different output spatial positions, obtaining a multi/demultiplexer device. When the linear phase front is changed along time, dynamic allocation of the wavelength channels can be obtained.

Several techniques have been previously reported in order to introduce a dynamic phase shift in arrayed waveguides, as for example the use of metamaterials [89] or taking advantage of the electro-optic [90], non-linear optical [91] or the thermo-optic [92] effects. As a drawbacks, the first two approaches require extra fabrication processes and the last two require long structures. For this reason, the acousto-optical effect proposed in [93–97], where a surface acoustic wave (SAW) can introduce a controlled phase shift in the waveguides, is envisaged as promising.

In this section, the proof of concept of an AWG whose channels are tuned by means of a SAW (AWG-SAW) is discussed. The device has been fabricated in AlGaAs technology, and measurements are provided to validate the concept.

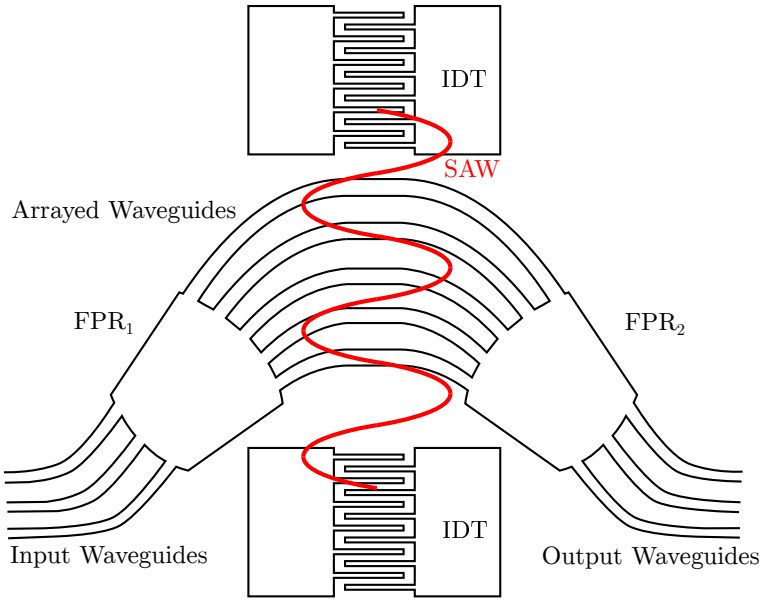

Figure 5.1: Schematic of the AWG-SAW, where the arrayed waveguides are placed between two interdigital transducers (IDTs). FPR stands for free propagation region and SAW stands for surface acoustic wave.

5.2 Operation principle

A schematic of the device is shown in Fig. 5.1. Basically, it is composed of a regular AWG where two interdigital transducers (IDTs) are placed at both sides of the arrayed waveguides. These IDTs will generate a surface acoustic wave (SAW) that modulates the AWs and dynamically modifies the output channel.

For completeness, the operation of the AWG, extensively discussed in Chapters 2 and 4, is revisited in the following lines. In the AWG, the incremental length between the arrayed waveguides introduces a linear phase shift that, combined with the output FPR, will focus the different wavelengths in different output spatial positions. Due to the fixed incremental length, for different wavelenghts the linear phase front slope is different (Section 2.2), hence they are focused to separated spatial positions. If the lineal phase front slope is externally modified, it is possible to redirect the wavelength components from one output waveguide to another one, obtaning a dynamic device. When applying a surface acoustic wave, a phase shift $\Delta\phi$ will be introduced in each of the waveguides due to the acousto-optic and electro-optic effects associated with the strain and piezoelectric fields, respectively. In the case of study the former dominates, and the latter can be omitted. The phase shift introduced by the SAW will be then formulated as [94]:

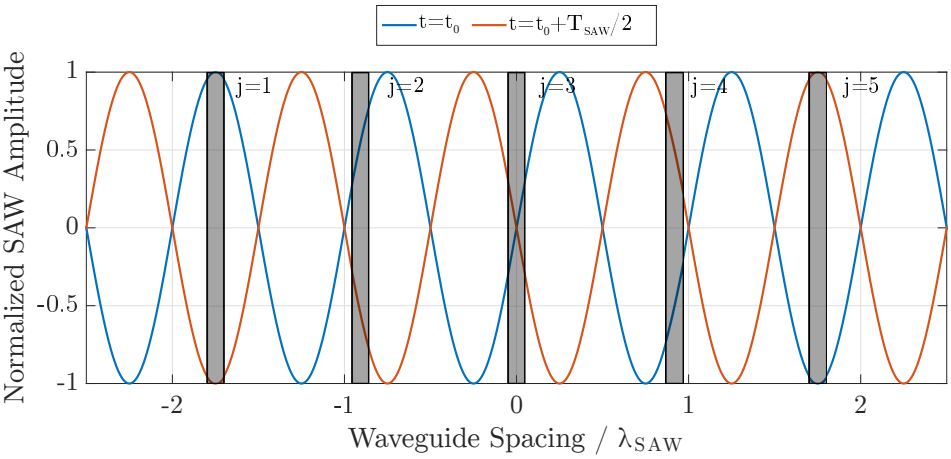

Figure 5.2: Positions for the AWs (grey color) taking into account the standing SAW nodes and anti-nodes for two different times. These positions are calculated to obtain a linear phase front, i.e. $\langle \kappa_1, \ldots, \kappa_5 \rangle = \langle \mp 1, \mp 1/2, 0, \pm 1/2, \pm 1 \rangle$.

$$\Delta\phi = \frac{2\pi l_{IDT}}{\lambda} \Delta n_{eff} = a_p \sqrt{P_{IDT}} \tag{5.1}$$

where l_{IDT} is the interaction length between the light and the acoustic wave, λ is the wavelength, Δn_{eff} is the variation of the AW effective index due to the SAW, a_p is a constant that depends on the elasto-optical properties of the material and the overlap between optical and acoustic fields [98], and P_{IDT} is the radio-frequency (RF) power applied to the IDT. Then, the effective index in the waveguide number j can be expressed as:

$$n_{eff(j)} = n^0_{eff} + \kappa_j \Delta n_{eff} \cos\left(\omega_{SAW} t\right) \tag{5.2}$$

where n^0_{eff} is the AW effective index when no SAW is applied, κ_j is the weight factor that accounts for the amplitude and the phase of the modulation in the jth AW, ω_{SAW} is the SAW angular frequency and t is the time. For the regular AWG, the length of the AW number j can be expressed as [34, 99]:

$$l_j = l_0 + \Delta l \left(j - 1\right) \tag{5.3}$$

where l_0 is the length of the shortest arm in the array and $\Delta l = m\lambda_0 / n^0_{eff}$ is the incremental length between the arms. The phase match condition for the output plane in the device will be [7, 34]:

$$\frac{2\pi}{\lambda} \left(n_{eff} \Delta l + n_s d_\omega \sin\theta\right) = 2n\pi \tag{5.4}$$

where n_{eff} is the effective index for the AWs, n_s is the effective index for the FPRs, d_ω is the separation between AWs, θ is the dispersion angle and n is an integer

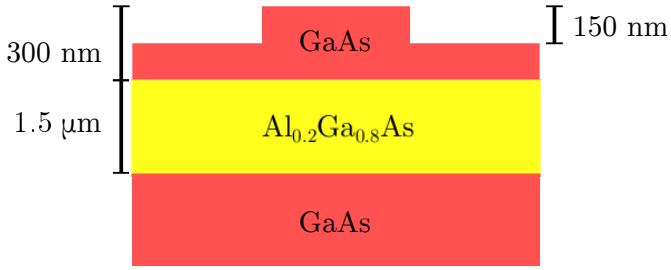

Figure 5.3: Structure of the simulated (Al,Ga)As cross-section.

number. With this equation, it is possible to calculate the dispersion angles where the output waveguides will be placed:

$$\theta(\lambda) \simeq \left(\frac{n_{eff}\Delta l}{n_s d_\omega}\right)\left[\left(\frac{\lambda}{\lambda_0}\right)\left(\frac{n^0_{eff}}{n_{eff}}\right) - 1\right] \tag{5.5}$$

In the last equation, if λ_0 is used, the dispersion angle will result zero, so the central wavelength will be focused at the center of the output plane, as was mentioned before. When a SAW is applied in the IDTs, there will be a modification of the dispersion angle in terms of time. For this reason, Eq. (5.5) can be rewritten introducing the shift in the effective index accounted in Eq. (5.2) as:

$$\theta(\lambda) \simeq \left(\frac{n_{eff}\Delta l}{n_s d_\omega}\right)\left[\left(\frac{\lambda}{\lambda_0}\right)\left(\frac{n^0_{eff}}{n_{eff}}\right) - 1\right] + \theta_{SAW}(\lambda) \tag{5.6}$$

where

$$\theta_{SAW}(\lambda) = -\left(\frac{l_{SAW}}{2n_s d_\omega}\right)(\kappa_{j+1} - \kappa_j)\,\Delta n_{eff}\cos(\omega_{SAW} t) \tag{5.7}$$

where l_{SAW} is the interaction length between the surface acoustic wave and the arrayed waveguides. From this last two equations, it is possible to determine the response for the AWG when no SAW has been applied, and also the channel shift depending on the time when the SAW has been applied. As a conclusion, if the variation of the dispersion angle is carefully designed, it is possible to obtain that one wavelength channel will be shifted through all the output waveguides. Because the phase difference introduced by the SAW modulation has to increase linearly between contiguous waveguides, the relative position among the AWs will be determined by the positions where the relative amplitude of the SAW increases linearly, being possible to use different periods. As an example, for the case of 5 waveguides in the array, Fig. 5.2 shows the positions where the AWs will be placed.

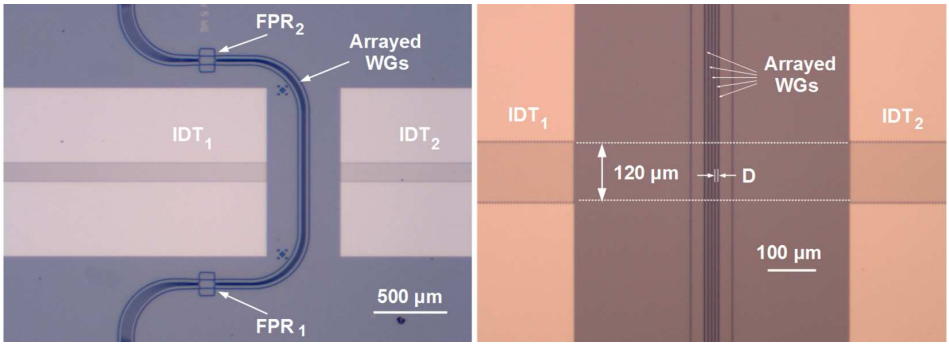

Figure 5.4: Microscope picture (a) of the fabricated device and (b) zoom of the modulated region where D $\simeq$ 6.53 μm.

5.3 AlGaAs technology

Some devices were designed and fabricated using the AlGaAs platform offered by the Paul Drude Insitute (PDI) in Berlin. These materials offer a good compromise between the index contrast in the processed optical waveguides and its acoustic properties. The structure of the simulated cross-section is shown in Fig. 5.3. The guiding layer consists of a 300-nm-thick GaAs film, which is deposited on a 1500-nm-thick $Al_{0.2}Ga_{0.8}As$ buffer layer. Both layers are grown on a (001) GaAs substrate. Then, the waveguide is etched 150 nm, obtaining the final cross-section.

Finally, the IDTs were fabricated using a three layer metallization of Ti/Al/Ti with a lift-off process in a split-finger configuration for efficient SAW generation.

5.4 Design, fabrication and characterization

In the aforementioned platform, the following design parameters were used. The width of the waveguide cross-section is 900 nm, and the core of 300 nm is shallowly etched down to 150 nm. The IDTs were designed for a SAW wavelength of λ_{SAW} = 5.6 μm [100], corresponding to a resonance frequency of approximately 520 MHz, with finger width and spacing of 700 nm and a length of 120 μm, as determined by the IDT aperture. From this data, the width of the AWs corresponded to approximately $\lambda_{SAW}/6$. This width was narrow enough to ensure a constant acoustic amplitude of modulation [94,95] but suitable to be fabricated with typical etching techniques as well.

The AWG-SAW was designed to operate at a wavelength of λ_0 = 900 nm for TE polarization. From the cross-section simulations, the effective index for the 900 nm width waveguide n_{eff} is 3.4872 and the effective index for the FPRs n_s is 3.4669. The focal length was calculated to be 105.305 μm and the incremental length between AWs Δl = 18.43 μm. As discussed before, the most important parameter when designing AWG-SAWs is the separation between the arrayed wa-

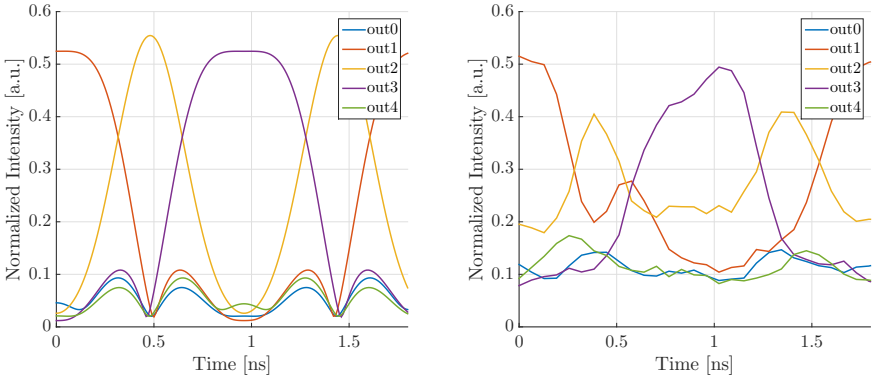

Figure 5.5: Dynamic response of the device: (a) simulations and (b) measurements when a SAW with a power $P_{IDT} = 80$ mW is applied in the IDTs. Light entering to the device has a $\lambda = 899$ nm and TE polarization. Only one acoustic period is shown.

veguides, as they have to be in positions where the amplitude relation of the standing wave remains linear. Considering the periodic nature of the SAWs, the separation between AWs that enables to obtain the linear change was 6.53 μm. For this particular design, the number of AWs was set to 5. Although an optimum imaging condition is obtained increasing the number of AWs, this improvement is at the expense of increasing the λ_{SAW}, consequently obtaining slower time response. Figure 5.4 shows a microscope picture of the fabricated device (left part) and the detail of the AWs between the two IDTs. The total size for the fabricated devices shown in the picture is 4.7×2.7 mm^2.

The response of the AWG device for no SAW applied was calculated using the models in Chapter 2, implemented in MATLAB/Octave [101, 102]. Figure 5.6-(a) shows the results, from which it is possible to derive that the maximum channel imbalance is around 3 dB and the channel insertion loss is approximately 10 dB. The motivation behind these high insertion loss per channel lies in the use of a very low number of AWs.

By design, when no SAW is applied in the device, stating from the central input waveguide, the central design wavelength will be focused to the central output waveguide. When the SAW is applied in the AWs, each channel will be shifted, to the adjacent output in the present design, durign the SAW period. To obtain a complete shift from one channel to the rest of channels, an additional 1.26 radians phase shift in the AWs would be required. For the designed IDT length of 120 μm, the required effective index change in each arrayed waveguide would be $\{-3.02, -1.51, 0, 1.51, 3.02\} \times 10^{-3}$, for j = 1 to 5, respectively.

For the device characterzation, a superluminescent diode (SLD) with peak emission at 920 nm and a full width at half maximum of 40 nm was employed

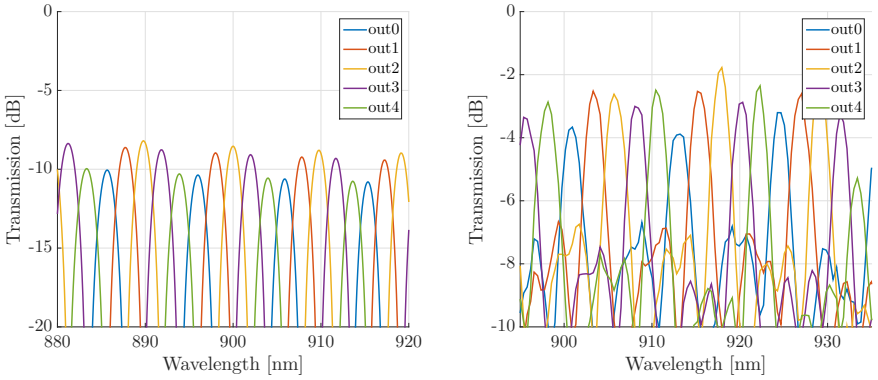

Figure 5.6: Response of the designed AWG-SAW from the central input waveguide and for TE polarization: (a) simulations and (b) measurements.

as a source, and the light was edge coupled into the photonic chip by means of a lensed fiber. Then, the transmitted light from the device was out-coupled from the chip to a single mode fiber using a 20× objective. The desired polarization was selected using a linear polarizer just before a beam splitter where half of the light was measured using a monochromatic CMOS camera to track the coupling. The other half arrived to a monochromator where different wavelength channels were spatially separated and the total spectral response measured by a CCD camera. Time-resolved measurements were obtained using a Si avalanche photodiode with a time resolution of 500 ps or a micro-channel plate photomultiplier tube with a time resolution of 300 ps. Both detectors were syncrhonized with the RF signal driving the IDTs and provided by an RF generator.

Figure 5.5-(a) shows the simulations when a SAW with a power $P_{IDT} = 80$ mW is applied in the IDTs. These simulations were performed using the central input waveguide with $\lambda = 899$ nm and TE polarization. From the results, the light oscillates between the preset channel (3) to the neighbour channels (2 and 4). Note that trace for channels 2 and 4 are de-phased by 180° with respect to each other because maximum transmission in each of these channels occurs when the cosine term in Eq. (5.2) is +1 or -1. In contrast, two maxima in the transmission occurs for the times when the standing SAW vanishes and then transmission happens for designed case, i.e. light from input 3 focuses in output 3. No modulation is observed in channels 1 and 5, since the applied SAW only enables to obtain oscillation from the preset output channel to the adjacent waveguides. As a comparison, Fig. 5.5-(b) shows the measurements from the fabricated device, obtaining a very good agreement with simulations.

5.5 Conclusion

A novel technique to dynamically tune the AWG has been presented. It is based on a standing surface acoustic wave that enables to introduce a linear phase shift in the arrayed waveguides of the AWG. The linear phase changes will shift the different wavelength channels between the output waveguides at different times. This device can operate in the low GHz range and, from measurements, modulation times of 1.9 ns have been demostrated. Comparing with other modulation techniques, the SAW offers a good compromise between operation speed and chip size.

The results of this chapter were obtaiened in close cooperation with Dr. Mauricio Morais de Lima and Antonio Crespo-Poveda (measurements of the devices), from Universitat de València, and Dr. Paulo Santos (fabrication) from the Paul Drude Institute Berlin. The results obtained from this chapter have been published in the following conferences and journals:

- A. Crespo-Poveda, R. Hey, K. Biermann, A. Tahraoui, P.V. Santos, B. Gargallo, P. Muñoz, A. Cantarero, and M.M. de Lima, "Synchronized photonic modulators driven by surface acoustic waves," *Optics Express*, vol. 21, no. 18, pp. 21669–21676, 2013.

- A. Crespo-Poveda, A. Hernández-Mínguez, B. Gargallo, K. Biermann, A. Tahraoui, P.V. Santos, P. Muñoz, A. Cantarero, and M.M. de Lima, "Acoustically driven arrayed waveguide grating," *Optics Express*, vol. 23, no. 16, pp. 21213–21231, 2015.

- A. Crespo-Poveda, B. Gargallo, I. Artundo, J.D. Doménech, P. Muñoz, R. Hey, K. Biermann, A. Tahraoui, P.V. Santos, A. Cantarero, and M.M. de Lima, "Photonic Mach-Zehnder modulators driven by surface acoustic waves in AlGaAs technology," in *Proc. SPIE 8989, Smart Photonic and Optoelectronic Integrated Circuits XVI*, paper 898905, San Francisco, California, United States, 2014.

- A. Crespo-Poveda, K. Biermann, A. Tahraoui, P. Santos, B. Gargallo, P. Muñoz, A. Cantarero, and M.M. de Lima, "Integrated Photonic Devices Driven by Surface Acoustic Waves," in *Proceedings of the 17th European Conference on Integrated Optics (ECIO)*, Nice, France, 2014.

Chapter 6
Thesis conclusions and outlook

6.1 Conclusions

The realization of all the objectives proposed at the beginning of this Ph.D. has been attained with the following conclusions:

- The analytical model to describe the operation of AWGs presented in [34] is used in Chapter 2 to develop the first version of the AWG design libraries. These libraries can be used to design regular AWGs following an orthogonal layout and are tested in two of the most important integration technologies (SOI and InP). Moreover, Si_3N_4 AWGs are reported in Appendix A, due to the lack of experimental results. From the comparison, InP AWGs seem to be better in terms of crosstalk and side lobe level due to the lower index contrast that implies lower phase errors, but SOI technology enables to obtain smaller devices since it permits the use of lower bending radius. Although Si_3N_4 AWGs were fabricated and characterized, no conclusions can be drawed from this technology due to the fabrication errors affecting all the devices. The AWG design libraries developed in this chapter have been licensed to the UPV Spin-Off company VLC Photonics S.L.

- In Chapter 3 the formulation introduced previously is extended for the case where different subsets of arrayed waveguides are used. This results in a variation of the AWG called interleave-chirped arrayed waveguide grating (IC-AWG). The theoretical model is able to describe the three fold operation of the device: channel demultiplexing, polarization splitting and 90° optical hybrid, obtained through the introduction of different base lengths in each subset of waveguides. The device has been fabricated in InP technology using four subsets to obtain the four different phase relations at the output. Measurements using a Mach-Zehnder interferometer as auxiliary input shows a good performance in terms of phase shift at the output waveguides, obtaining the necessary phase relations for each channel, and proving

that the channel demultiplexing and 90° optical hybrid operations are obtained. Finally, the polarization splitting operation is achieved due to the use of birefringent waveguides. However, birefringence is higher than expected from simulations, so it is necessary to include feedback from fabrication for the design of IC-AWGs.

- The formulation of the AWG is also extendend in Chapter 4 for the case where the AWG is cut in half and the arrayed waveguides are ended with reflectors. This reflective type of AWG, called R-AWG, can be used to reduce the size of the device and thus decrease the price of fabrication. Moreover, the use of tunable couplers and phase shifters is useful to obtain different pass-band shapes. For the proof of concept, a R-AWG where all the reflectors are the same with total reflection is designed and fabricated in SOI technology. Then, it is compared with a regular AWG fabricated in the same chip. Degradations in the pass-band shape can be observed in this comparison, mainly attributed to design of the Sagnac loop reflectors used at the end of the arrayed waveguides. In any case, the theoretical model developed in this chapter can be used to explain the functionality of R-AWGs and introduce the tunability of the pass-band shape.

- Finally, the last chapter of this thesis is devoted to develop one new AWG functionality, an AWG driven by surface acoustic waves, called AWG-SAW. This device can be tuned by means of a SAW, introducing a controlled phase shift in the arrayed waveguides. The theoretical expressions to describe the functionality of the device are provide during this chapter, providing the necesary design equations. The device has been fabricated in AlGaAs technology since in this material the acousto-optic effect is high enough to modify the phase in the AWs and tune the AWG response. Simulations using the theoretical model are in good agreement with the static and dynamic measurements of the device, obtaining operation in the low GHz range.

6.2 Outlook

After the work developed in this thesis, there are some open research lines that may be continued:

- The development of the design libraries for regular AWGs presented in Chapter 2 to include not only the orthogonal layout but also Smit and S-type layouts in technologies other than Si_3N_4.
- The fabrication of regular AWGs in Si_3N_4 technology in a mature platform using the developed design libraries to test and compare the three most used technologies (SOI, InP and Si_3N_4).
- The design, fabrication and characterization of R-AWGs presented in Chapter 4 in other integration technologies where phase errors are lower than in SOI technology, as for example InP.
- The fabrication and characterization for the R-AWG with custom spectral response presented in Chapter 4 to obtain different tailored pass-band shapes.

Appendices

Appendix A
Silicon Nitride AWGs

A.1 Overview

The AWGs in this appendix were designed for and fabbed in the Silicon Nitride technology of the National Center for Microelectronics of Barcelona, Spain [1]. This technology offers guidance of light in a wavelength range from visible (around 400 nm) to mid-infrared (2.3 μm) [103], giving room to applications other than the typical in communications: spectrometry, sensing, lab-on-a-chip systems, optical coherence tomography, multispectral light source, point of care cytometer and vital multi-degree-of-freedom sensor on chip, among other.

This platform, following the concept of generic integration introduced in Section 1.2, incorporates fundamental building blocks such as waveguides, bends, multimode interference (MMI) couplers, waveguide transitions and input/ouput tapers. However, AWGs are not part of the PDK and had not been demonstrated before.

Two different cross-sections are available in this platform: deep and shallow (Fig. A.1). In the deep waveguides, the light is more confined in the core than in the shallow waveguides. Thus, smaller bending radius can be achived for deep waveguides. However, deep waveguides have higher losses than shallow waveguides, due to sidewall roughness (that causes optical scattering) induced during the etching process (deep waveguides are etched down the 300 nm of the Silicon Nitride, and shallow aveguides only the first 150 nm).

In the platform, two additional process steps are offered: metalization and selective area trenching, as is shown in Fig. A.1. Selective area trenching exposes the evanescent field of the waveguides, that may interact with different substances filling the trench, for sensing applications. The trenches may also be useful for heat isolation, since the heat conduction in air much smaller than in the materials used in the layerstack. Moreover, thermo-optic heaters are used in several components

[1] A process co-developed by VLC Photonics, a spin-off from the Universitat Politècnica de València (Valencia, Spain).

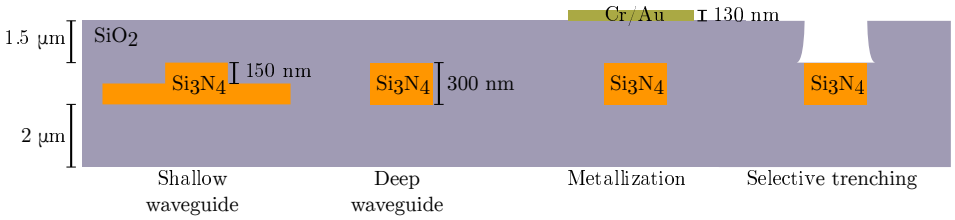

Figure A.1: Available cross-sections and extra process steps available in the CNM-VLC Photonics MPW.

in photonics, as for instance in optical phase shifters and modest speed modulators (speed up to few kHz).

A.2 Design, fabrication and characterization

Two chips were designed and fabbed, employing cells in the MPW run of different sizes [1]. For this first run, the main idea is to use the AWG libraries to design and fabricate regular AWGs as a test of the technology.

The design for the large cell layout is shown in Fig. A.2-(a) and a microscope photograph of the fabricated chip is provided in Fig. A.2-(b). AWGs with three different channel spacings (100, 200 and 400 GHz) and three different i/o waveguide widths in the slab coupler-array interface (1.5, 2.0 and 3.0 μm) were included. The arrayed waveguides (AWs) were fabricated in the deep cross-section using a width of 1.0 μm to reduce the cross-talk due to phase noise [47]. Thus, these sections will be no longer single-mode, but due to the use of adiabatic transitions (i.e. no high-order modes are excited) and the no presence of bends, coupling to high-order modes should be small. As a result, the field in this sections is not highly confined in the waveguide core, being more tolerant to the phase errors arising from sidewall roughness [47]. The bend radius in the PDK for the deep waveguide was set to 50 μm.

For the medium die size, one AWG with a channel spacing of 50 GHz and two 200 GHz AWGs are designed. The mask layout for this design can be seen in Fig. A.3-(a) and a microscope picture of the fabricated devices is shown in Fig. A.3-(b).

The most important parameters for the designed and fabricated devices in the CNM-VLC Photonics MPW run can be found in Table A.1. In this case, the 2.0 μm width input/output waveguide designs were chosen as a reference, and AWGs with a channel spacing of 50, 100, 200 and 400 GHz were designed. As is explained in [46], if the channel spacing is maintained, different FSRs can be obtained increasing the focal length or decreasing the arrayed waveguides spacing. Increasing the focal length will result in bigger AWGs, obtaining higher propagation losses and phase

[1] Two different user area sizes available: medium and large. The sizes are 5.5×5.5 mm^2 and 11×5.5 mm^2, respectively.

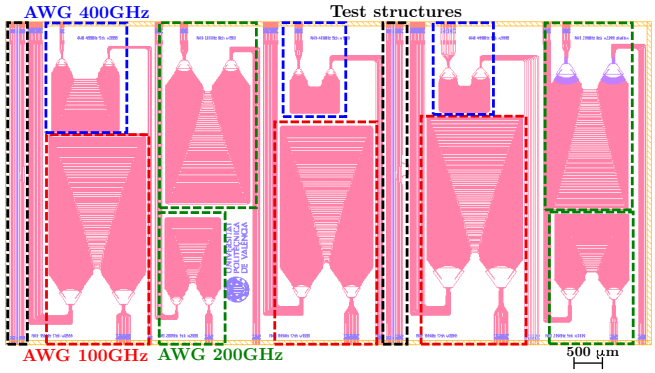

(a)

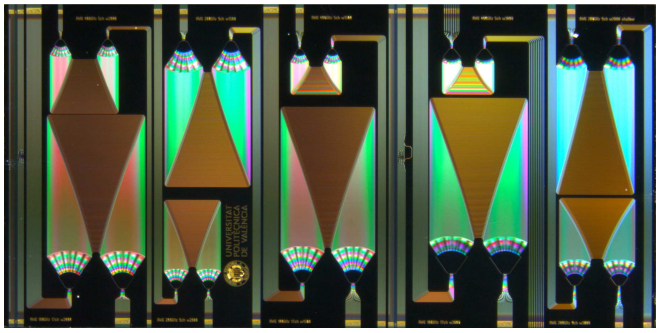

(b)

Figure A.2: Chip design (a) and fabricated cell (b) (5.5×11 mm^2).

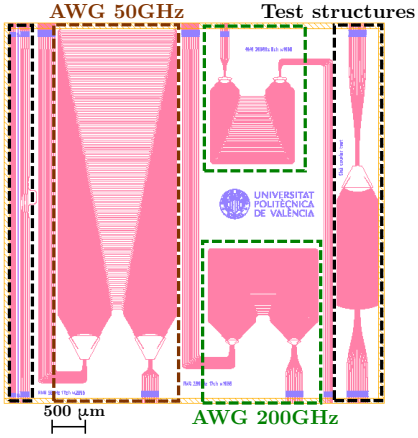

(a)

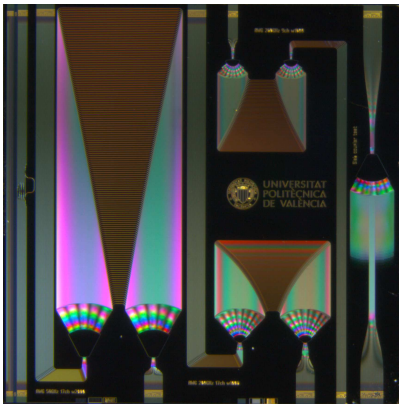

(b)

Figure A.3: Design for the medium size cell in the CNM-VLC MPW run: (a) layout and (b) microscope picture.

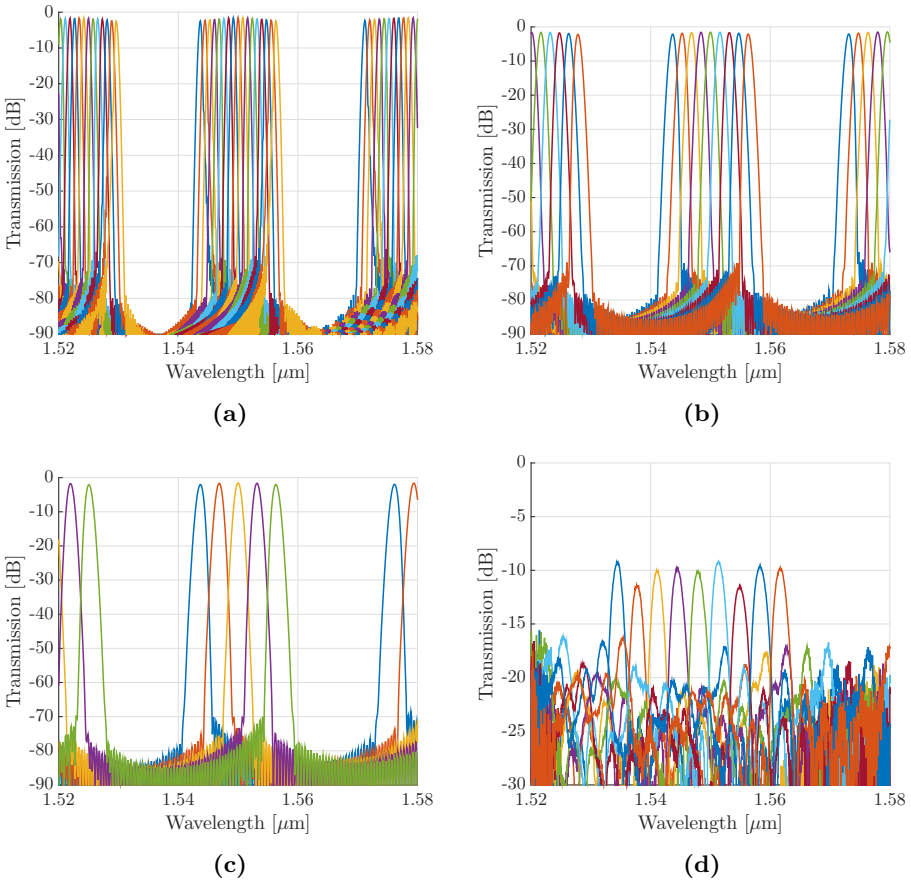

Figure A.4: Simulations for the AWGs, using the 2.0 μm width deep cross-section in the interface between the slab coupler and the AWs, when a channel spacing of (a) 100 GHz, (b) 200 GHz and (c) 400 GHz is chosen. (d) Measurements for the 400 GHz AWG using the 1.5 μm width deep cross-section in the interface between the slab coupler and the AWs.

errors. In the case of decreasing the AWs spacing, the size of the AWG will remain the same but the number of AWs will increase. Then, some variations were introduced in the width of the arrayed waveguides and the length of the slab couplers, in order to study the performance of these devices for different FSRs.

Note that typical test structures were introduced in every chip, in order to derive information on the fabrication process. As a test structures it is possible to find deep and shallow straight waveguides of different widths, 1x2 and 2x2 multimode intereference couplers and Mach-Zehnder interferometers were included. For example, the source spectrum after traversing the straight waveguides is used

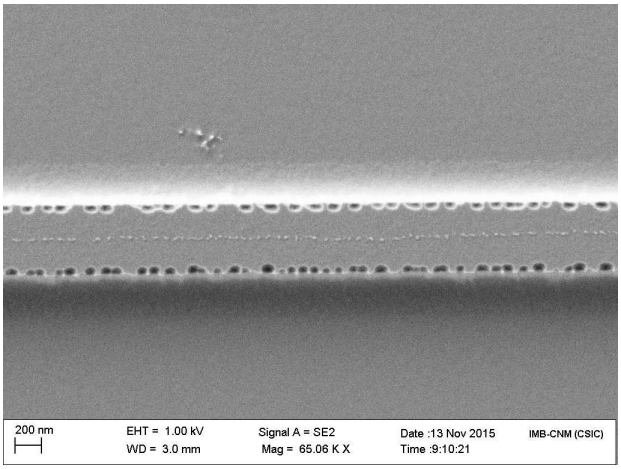

Figure A.5: SEM picture of the pilot CNM run showing side-wall roughness.

to normalize the response of every device in the chip, so as to correct the source non-uniform spectrum (typically an ASE source) and the in/out coupling losses. This group of test structures will be repeated during this thesis in every design made and in any technology, sometimes including new ones when some additional functionality needs to be tested.

The simulations for the designed 100, 200 and 400 GHz AWGs are shown in Figs. A.4-(a), (b) and (c). In the simulations, typical propagation losses for this technology (around 0.5 dB/cm) were not included. The AWG insertion losses in the graphs, correspond then to the diffraction losses [34].

Since the devices were fabricated in a pilot run for this technology, issues derived from the fabrication process made impossible to characterize most of the AWGs. From SEM pictures, Fig. A.5, the sidewall roughness in the waveguides is high, due to the lack of an annealing process in the SiNx layer to obtain smoother waveguides. Thus, the measured propagation losses on-chip for this run are higher than 2 dB/cm, while 0.5 dB/cm were expected as maximum. Moreover, chip facets were not correctly cut, making difficult to couple the light in/out of the chip. Finally, the lithography process for the waveguide definition reduced the designed waveguide width in 200 nm. For these reasons, only measurements for the 400 GHz AWG using $w_{AW} = 1.5$ μm are shown in Fig. A.4-(d). From measurements, the central wavelength λ_0 is 1548 nm, the separation between channels $\Delta\lambda_{ch}$ is 3.3 nm and the FSR is 64.64 dB. This deviation in the design parameters is mainly attributed to the fact that the fabricated waveguide widths are not the designed ones. The side-lobe level is around 10 dB in the worst case. The losses per channel are between 9 and 12 dB, as was commented mainly due to the side-wall roughness that induces losses around 2 dB/cm (while 0.5 dB/cm maximum is expected for this technology).

DIE	Δf_{ch} [GHz]	w_{IO} [μm]	w_{AW} [μm]	g_{AW} [μm]	N_{IO}	FSR [nm]	N	m	L_f [μm]	ΔL [μm]	BW	DE
L	400	2.0	1.5	0.6	9	57.6	71	22	119.8	21.7	0.5	NO
L	400	2.0	2.0	0.6	5	32.0	65	40	135.9	39.4	0.3	NO
L	400	2.0	3.0	0.6	9	57.6	71	22	205.4	21.7	0.5	NO
M	200	1.0	1.0	1.6	9	28.8	109	31	110.2	30.5	0.5	NO
M	200	1.0	1.0	0.6	17	40.8	65	44	100.9	43.3	0.4	NO
L	200	2.0	1.5	0.6	9	28.8	119	44	199.7	43.3	0.3	NO
L	200	2.0	2.0	0.6	9	28.8	71	44	148.3	43.3	0.5	NO
L	200	2.0	3.0	0.6	9	28.8	71	44	205.4	43.3	0.5	NO
L	200	2.0	2.0	0.6	9	28.8	119	44	247.2	43.3	0.3	YES
L	100	2.0	1.5	0.6	17	27.2	133	47	224.3	46.3	0.5	NO
L	100	2.0	2.0	0.6	17	27.2	133	47	277.7	46.3	0.5	NO
L	100	2.0	3.0	0.6	17	27.2	133	47	384.5	46.3	0.5	NO
M	50	2.0	2.0	0.6	17	20.4	159	62	382.8	61.0	0.5	NO

Table A.1: Summary of the AWGs designed for the silicon nitride devices run. Abbreviations: DIE stands for die size (L: large, 11×5.5 mm^2; and M: medium, 5.5×5.5 mm^2), Δf_{ch} for channel spacing, w_{IO} for input/output waveguide width, w_{AW} for arrayed waveguide width, g_{AW} for gap between arrayed waveguides, N_{IO} for number of input/output waveguides, FSR for free spectral range, N for number of arrayed waveguides, m for grating order, L_f for focal length, ΔL for incremental length between arrayed waveguides, BW for channel bandwidth as a fraction of the channel spacing, and DE for double etched (YES) or single etched (NO) waveguide in the array.

Appendix B
AWG layouts

As has been mentioned through this thesis, the AWG is composed of two free propagation regions and a group of arrayed waveguides with an incremental length between them [7]. For the design layout, several geometries have been discussed in the literature, being the two most typicals the orthogonal layout presented in [54] and the Smit layout introduced in [104]. However, other layouts have been proposed to avoid phase errors [105], reduce channel spacing [106] or obtain broadband multiplexers [107].

From the large variety of options, three different layouts have been implemented in the AWG design libraries (Appendix C): the orthogonal, the Smit and the S-type layouts. In this appendix, the lyaout structure and the advantages and disavantages of each layout will be explained.

B.1 Orthogonal layout

In the orthogonal layout, all the waveguides have approximately the same length in the bend sections and the incremental length is introduced in the straight sections, as is shown in Fig. B.1-(a). The strenght of this layout lies in that the arrayed waveguides have the same number of bend sections and almost all the incremental length between arrayed waveguides is introduced in the straight sections, so the errors derived from the different effective index calculations for different waveguides are avoided. In opposition, this layout increases drastically when the incremental length between arrayed waveguides is large (i.e. reduced free spectral ranges). Also, if the incremental length between arrayed waveguides is small, straight sections on top of the AWG can be overlapped. Due to the fact that a high number of arrayed waveguides run parallel long distances, it is possible to obtain cross-talk between the waveguides.

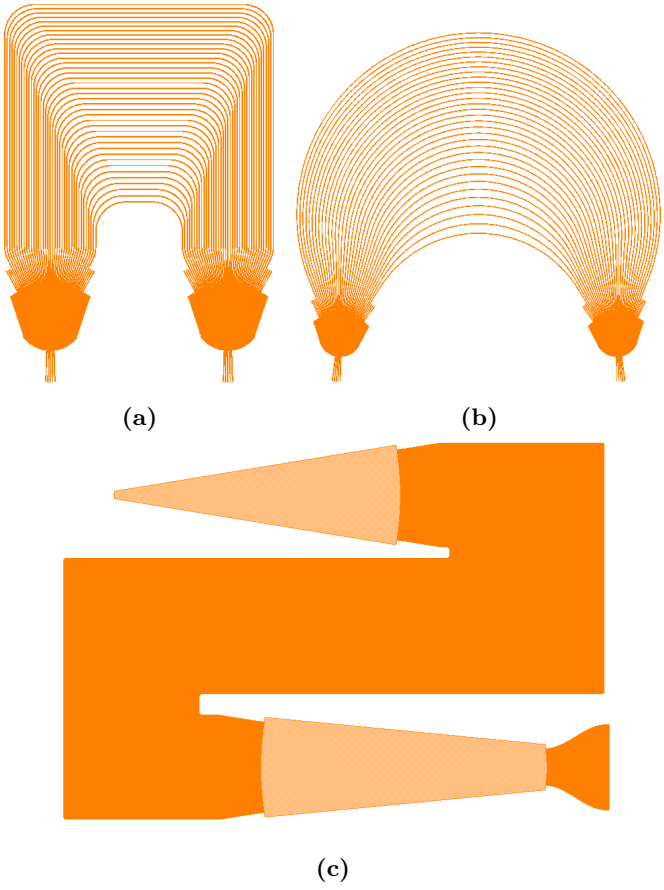

Figure B.1: Different layout configurations for the AWG: (a) Orthogonal, (b) Smit and (c) S-type layouts.

B.2 Smit layout

In the Smit layout, Fig. B.1-(b), the incremental length between arrayed waveguides is introduced in bend sections with different radius. As a result, the layout is generally smaller than in the case of the orthogonal layout. Moreover, it is more flexible to obtain lower and higher free spectral ranges than in the case of the orthogonal layout. On the other hand, the use the difference between arrayed waveguides where different radius are used implies that the calculation of the effective index should be very accurate for each arrayed waveguide to avoid possible design errors. In addition, bend sections have higher losses than straight sections for reduced radius, so it should be necessary a compromise between size and losses. Finally, low index contrast technologies usually have large bending radius, so the reduction of size is not an advantage for these technologies.

B.3 S-type layout

The S-type layout shown in Fig. B.1-(c) is suitable for applications where a large free spectral range is required, and the small incremental length between arrayed waveguide makes impossible to use the other layouts. Thus, it is possible to obtain very large free spectral ranges, since it enables to introduce small incremental lengths between arrayed waveguides. On the other side, the arrayed waveguide are very long, which introduces higher propagation losses and phase errors compared with other layouts. Moreover, the long arrayed waveguides imply that the size for the complete layout is usually very big.

Appendix C
AWG libraries

As has been mentioned through this thesis, AWG design libraries for different technologies/materials have been developed to obtain an AWG layout from the high level parameter requirements. These libraries also provide the framework to simulate the designed AWG in a mathematical software as Octave/Matlab.

C.1 Introduction

C.1.1 Libraries provided in this version

In this library version, the next layouts for specific technologies or foundries are provided:

		Layout		
Technology	**Foundry**	**Orthogonal**	**Smit**	**S-type**
InP	HHI	✓	✓	
	SMART	✓	✓	
	Oclaro	✓	✓	
Si_3N_4	CNM	✓	✓	✓
	TripleX	✓	✓	✓
SOI	Thin SOI	✓	✓	
	VTT	✓	✓	
	Imec	✓	✓	
	IME	✓	✓	

C.1.2 Available waveguides from each foundry

For each technology/foundry, the next waveguide cross-sections are available to design AWGs:

Foundry	CNM	HHI	SMART	SOI	VTT
$De_{st}w\,[\mu m]$	$[1.0, 1.5]$	$[1.5, 2.0]$	$[1.2, 3.0]$	0.45	2.4
$De_{bd}w\,[\mu m]$	$[1.0, 1.5]$	$[1.5, 2.0]$	$[1.2, 3.0]$	0.45	2.4
$De_{bd}R\,[\mu m]$	≥ 25	≥ 225	≥ 100	≥ 5	≥ 150
$Sh_{st}w\,[\mu m]$	$[1.0, 1.5]$	$[1.5, 2.0]$	$[1.8, 2.2]$	2.0	2.4
$Sh_{bd}w\,[\mu m]$	$[1.0, 1.5]$	$[1.5, 2.0]$	$[1.8, 2.2]$	2.0	2.4
$Sh_{bd}R\,[\mu m]$	≥ 100	≥ 5000	≥ 100	≥ 250	≥ 3000
$wvl\,[\mu m]$	$[1.5, 1.6]$	$[1.5, 1.6]$	$[1.53, 1.57]$	$[1.5, 1.6]$	$[1.25, 1.35]$

where $De_{st}w$ stands for deep straight width, $De_{bd}w$ for deep bend width, $De_{bd}R$ for deep bend radius, $Sh_{st}w$ for shallow straight width, $Sh_{bd}w$ for shallow bend width, $Sh_{bd}R$ for shallow bend radius and wvl for wavelength.

C.1.3 Different layouts

The module currently supports 3 types of AWGs: Orthogonal, Smit and S-type, as is explained in Appendix B.

C.1.4 Single-etched and double-etched AWG

When designing the AWGs, it is possible to choose between a single-etched or a double-etched slab coupler. Typical AWGs are designed to be double-etched, what means that the slab couplers will be fabricated in the shallow cross-sections and also their input/outputs, while the arrayed waveguides (where the incremental length will be introduced) should be fabricated in deeply etched cross-sections. The main reason for such structure is to reduce the losses and the possible reflections in the interface between the slab coupler and the waveguides, since deeply etched waveguides cause a large discontinuity in this interface. Figure C.1 shows the difference between etching levels in the mask and in a fabricated device. It is up to the designer to choose a single-etched or double-etched AWG depending on the technology and the requirements. To know more about how to choose between etching levels in the AWG, please refer to Section C.2.4.

C.1.5 AWG layout with parameters

Figure C.2 shows the AWG with the parameters that can be modified. Please refer to Sections C.2.4 (parameters in blue) and C.2.5 (parameters in black) to further details.

C.2 Drawing an AWG

This section describes how to draw an AWG for one specific technology. Note that it is possible to use a different technology/foundry if it has been implemented.

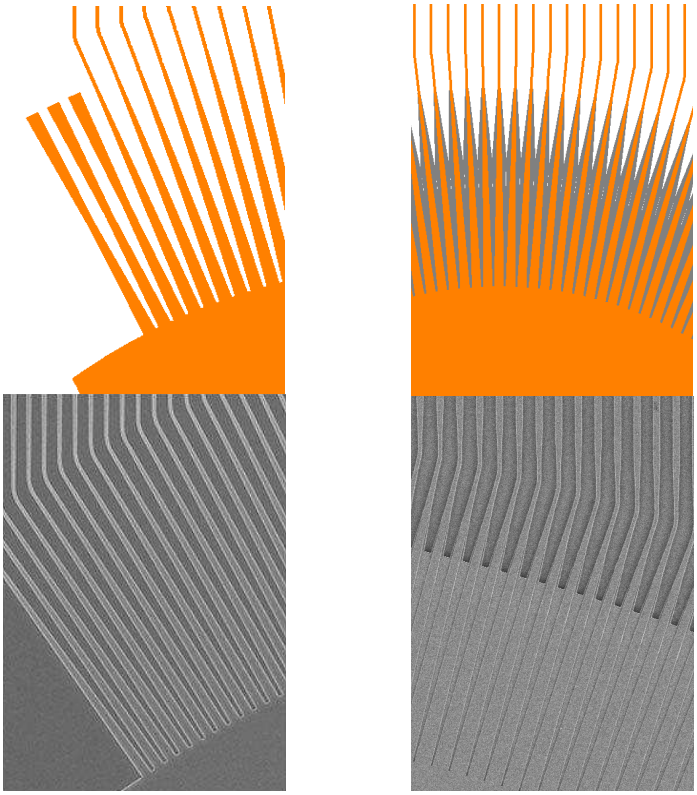

(a) Single-etched AWG **(b)** Double-etched AWG

Figure C.1: Etching levels in the Slab coupler

For more information about implemented technologies and layouts, please refer to Section C.1.1.

C.2.1 Loading the AWG module

The first thing to do when loading the AWG module is to enable the foundry that we are going to use. In this case, the selected technology will be `CNM`. The procedure to do it is the next one:

```
// ----------------------------------------
// LOAD AND SELECT FOUNDRY, PACKAGING AND DESIGN HOUSES
pda::loadFoundry    ("foundryCNM");
pda::enableFoundry  ("CNM");
#include @topview;
```

If necessary, it is possible to include additional foundry files. Please, contact your selected foundry or design house to obtain more information about additional files.

As an example, CNM provides the design kit (PDK) in additional files that have to be included:

```
#include "cnm_library_02_MaskCrossSection.spt";
```

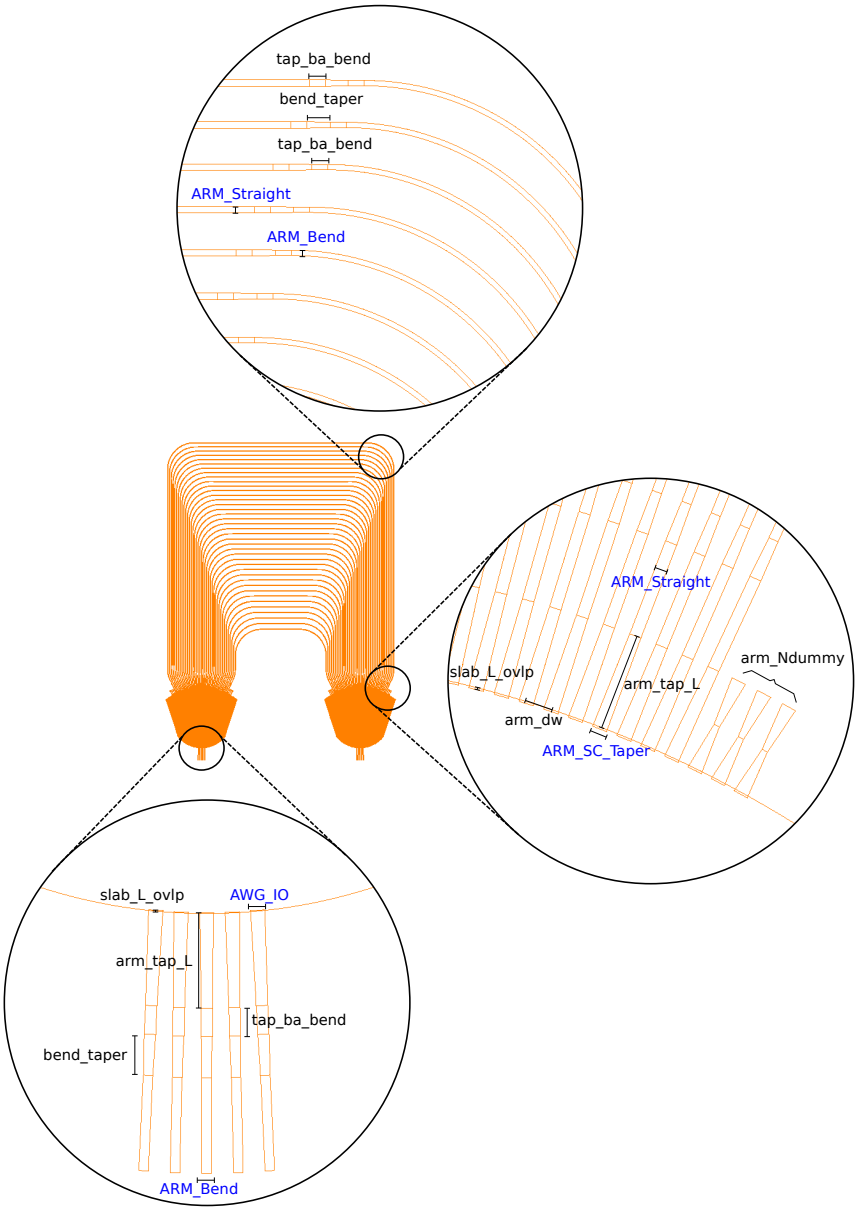

Figure C.2: The AWG with parameters

```
#include "cnm_library_04_MaskLayout.spt";
```

Once we have prepared the foundry library, we will include the library files necessary to design and draw the AWG. First, we add the two library folders (`lib` folder with the generic files and foundry folder with the specific files) to the path. Then we include the Orthogonal and Smit AWG libraries that are implemented in `CNM`.

```
// ----------------------------------------
// MY INCLUDES
sys::include("~/AWGlib/lib/");
sys::include("~/AWGlib/cnm/");
#include "libBB-CNM-AWG-ORTHOGONAL.spt";     // ORTHOGONAL AWG
#include "libBB-CNM-AWG-SMIT.spt";           // SMIT AWG
```

At this point, we are ready to specify the AWG high level parameters and draw the AWG layout.

C.2.2 Creating the AWG

Once we have loaded the foundry PDK and the AWG module, it is necessary to create the "void" AWG that we will modify specifying the required parameters. The instruction to create an Orthogonal AWG will be:

```
upv_AWG_CNM_ORTHOGONAL() awg_orthogonal;
```

where `awg_orthogonal` will be our "void" Orthogonal AWG. In the case of the Smit AWG, the procedure is the same but calling the Smit building block:

```
upv_AWG_CNM_SMIT() awg_smit;
```

For simplicity, the next instructions about specifying the AWG attributes will be explained for the orthogonal case, since all that attributes and functions are shared between both layouts.

C.2.3 Specifying data export options

The AWG physical parameters that are calculated internally from the high level requirements (incremental length, focal distance...) will be exported to make easier the later simulation. For this reason, it is necessary to specify the AWG name and the different folders where this parameters will be saved. The set of functions to provide the export options are the next ones:

```
string simulationpath = "~/AWGlib/cnm/";
string projectname_orthogonal  = "CNM_AWG_ORTHOGONAL_TEST";
awg_orthogonal.setFNAMEPREFIX(simulationpath+projectname_orthogonal);
awg_orthogonal.setEXPORTARMS(1);
awg_orthogonal.setEXPORTOCTAVEWVG(1);
```

The first two string definitions will define the simulation path and the name for the generated files. The AWG functions to set these parameters are the next three, being summarised in the table below:

awg.setFNAMEPREFIX(string)	Set the AWG name and path
awg.setEXPORTARMS(int)	0: Do not export arm lengths to file 1: Export lengths
awg.setEXPORTOCTAVEWVG(int)	0: Do not export parameters for simulation 1: Export parameters

C.2.4 Specifying the technology and waveguide parameters

The next step is to specify the technology file that we will use for the AWG and the waveguide parameters (width, radius, polarization...) that we require. The next code provides an example of how to use the different AWG functions to provide the data:

```
string foundry_file = "~/AWGlib/cnm/cnm_technology.txt";
awg_orthogonal.setFOUNDRY_FILE(foundry_file);
awg_orthogonal.setDOUBLE_ETCHED(1);
awg_orthogonal.setFOUNDRY("CNM");
awg_orthogonal.setARM_Straight("de",0,1.0,0);
awg_orthogonal.setARM_Bend("de",50.0,1.0,0);
awg_orthogonal.setARM_SC_Taper("sh",0,1.5,0);
awg_orthogonal.setSlabCoupler("SLAB",0,0,0);
awg_orthogonal.setAWG_IO("sh",0,1.5,0);
```

The used functions are explained in the table below:

C.2.5 Specifying design parameters

When the technology, the layout and the waveguides are chosen, it is only necessary to specify the parameters that govern the AWG generation. An example of this parameters is provided, and also a table to list each parameter and its function.

```
int No_orthogonal = 5;
double wvl0_orthogonal = 1550e-9;
double Awvl_c_orthogonal = 1e-9;
double Av_c_orthogonal = Awvl_c_orthogonal*physics::c/wvl0_orthogonal/
    wvl0_orthogonal;
double Av_FSR_orthogonal = 3*No_orthogonal*Av_c_orthogonal;
double Av_bw_orthogonal = 0.5*Av_c_orthogonal;
double f0_orthogonal = physics::c / wvl0_orthogonal;
double p_arm_dw_orthogonal = 2.6e-6;
double p_arm_tap_L_orthogonal = 40e-6;
double p_arm_Lv_0_orthogonal = 11e-6;
double p_arm_R_ref_orthogonal = 100.0e-6;
double p_Lu_orthogonal= 0.5;
double p_AAF_orthogonal = 0.99;
double p_f0_orthogonal = f0_orthogonal;
int p_No_orthogonal = No_orthogonal;
int p_Nch_in_orthogonal = No_orthogonal;
int p_Nch_out_orthogonal = No_orthogonal;
double p_Av_c_orthogonal = Av_c_orthogonal;
double p_Av_FSR_orthogonal = Av_FSR_orthogonal;
double p_Av_bw_orthogonal = Av_bw_orthogonal;
double p_slab_d_IO_orthogonal = 1000.0;
```

awg.setFOUNDRY_FILE(string foundry_file)	Set the path to the foundry file
awg.DOUBLE_ETCHED(int etching)	0: Use a single-etched slab coupler 1: Use a double-etched slab coupler
awg.FOUNDRY(string foundry)	Specify the foundry name
awg.ARM_Straight(string type, double radius, double width, int pol)	Define the waveguide used in the straight section "de" for deep and "sh" for shallow waveguides Bending radius in microns Waveguide width in microns Design polarization (0: TE, 1: TM)
awg.ARM_Bend(string type, double radius, double width, int pol)	Define the waveguide used in the bent section "de" for deep and "sh" for shallow waveguides Bending radius in microns Waveguide width in microns Design polarization (0: TE, 1: TM)
awg.ARM_SC_Taper(string type, double radius, double width, int pol)	Define the waveguide in the slab/AW interface "de" for deep and "sh" for shallow waveguides Bending radius in microns Waveguide width in microns Design polarization (0: TE, 1: TM)
awg.SlabCoupler(string type, double radius, double width, int pol)	Define the slab coupler "SLAB" typically for the slab coupler Bending radius in microns Waveguide width in microns Design polarization (0: TE, 1: TM)
awg.AWG_IO(string type, double radius, double width, int pol)	Define the waveguide in the IO/slab interface "de" for deep and "sh" for shallow waveguides Bending radius in microns Waveguide width in microns Design polarization (0: TE, 1: TM)

```
int p_arm_Ndummy_orthogonal = 3;
double p_slab_L_ovlp_orthogonal = 0.1;
int type_orthogonal = 0;
double p_tap_ba_bend_orthogonal = 3.0;
double p_bend_taper_orthogonal = 4.3;
```

C.2.6 Calling the constructor, designing and drawing

The final step is to call the constructor function specifying the aforementioned parameters, execute the design function and draw the AWG in the preferred place. The necessary sentences to execute that, are the next ones:

```
awg_orthogonal.constructor(p_arm_dw_orthogonal,p_arm_tap_L_orthogonal,
    p_arm_Lv_0_orthogonal,p_arm_R_ref_orthogonal,p_Lu_orthogonal,
    p_AAF_orthogonal,p_f0_orthogonal,p_No_orthogonal,
    p_Nch_in_orthogonal,p_Nch_out_orthogonal,p_Av_c_orthogonal,
    p_Av_FSR_orthogonal,p_Av_bw_orthogonal,p_slab_d_IO_orthogonal,
    p_arm_Ndummy_orthogonal,p_slab_L_ovlp_orthogonal,type_orthogonal,
    p_tap_ba_bend_orthogonal,p_bend_taper_orthogonal);
awg_orthogonal.design();
var awg_design_orthogonal = awg_orthogonal.lyt(cin -> [500,500,90]: );
```

With the `constructor` function, we provide the AWG with all the necessary high level parameters to obtain the desired AWG. The `design` function will execute

Name	Function	Range	Units	Type
No	Number of design IO	> 0		int
Nch_in	Number of physical inputs	> 0		int
Nch_out	Number of physical outputs	> 0		int
wvl0	Central wavelength	$[0.6, 1.6]$	μm	double
f0	Central frequency	$[187.5, 500]$	THz	double
Awvl_c	Channel spacing (wavelength)	> 0	m	double
Av_c	Channel spacing (frequency)	> 0	Hz	double
Av_FSR	Free spectral range	> 0	Hz	double
Av_bw	Channel bandwidth	> 0	Hz	double
arm_dw	Arm distance between centers	≥ 0	m	double
arm_tap_L	Taper length	≥ 0	m	double
Lv_0	Shortest arm length (unused)	≥ 0	m	double
arm_R_ref	Reference radius (unused)	≥ 0	m	double
Lu	Non-uniformity level (unused)	≥ 0		double
AAF	Array Acceptance Factor	$[0, 1]$		double
slab_d_IO	Distance between input/output slab	≥ 0	μm	double
arm_Ndummy	Number of dummy arms in the slab	≥ 0		double
slab_L_ovlp	Overlap between waveguides and slab	≥ 0	μm	double
type	Slab type (unused)	0		int
tap_ba_bend	Straight section before/after bends	≥ 0	μm	double
bend_taper	Taper length before/after bends	≥ 0	μm	double

the necessary calculations to obtain the different physical parameters. Finally, the `lyt` function will place the AWG layout in the specified place (in the case of the example in the position $[500, 500]$ and rotated 90 degrees).

C.3 Simulating the AWG in Matlab

This section explains how to simulate the designed AWG with the provided Matlab simulator.

C.3.1 Simulator files

The AWG simulator is located in the `simulator` folder. It is composed by four files:

- `data_from_sql.m` : Obtains the data from the sql library
- `read_technology.m` : Obtains the data from the technology file
- `diffr.m` : Calculates the Fresnel diffraction integral
- `simulator.m` : Main file of the simulator

C.3.2 Optodesigner AWG output files

This simulator makes use of the OptoDesigner AWG output files, that are listed below:

- `XXXX_ARMS` : File containing the arms physical length
- `XXXX_PARAMS.m` : File containing the AWG high level parameters
- `XXXX_wvgARM_Bend.m` : File containing the bent waveguides
- `XXXX_wvgARM_SC_Taper.m` : File containing the slab/AW interface waveguides
- `XXXX_wvgARM_Straight.m` : File containing the straight waveguides
- `XXXX_wvgAWG_IO.m` : File containing the input/output waveguides
- `XXXX_wvgSlabCoupler.m` : File containing the slab coupler

where XXXX is the AWG name given through the `setFNAMEPREFIX` function (see Sec. C.2.3 for further details).

C.3.3 AWG simulator main file

There are some options that can be changed in the main simulator file. This is an example of the parameters:

```
%% CHANGE HERE THE SIMULATION PARAMETERS!!!

  % Select the AWG prefix to simulate
  fileprefix='CNM_AWG_REGULAR_TEST';

  % Select if simulate using the DB or the spline (0: DB, 1: spline)
  select_inter = 1;
  techfile = 'cnm_technology.txt';

  % Wavelength
  wvls=1.54;     % Wavelength start
  wvle=1.56;     % Wavelength end
  wvli=0.0001;     % Wavelength increment

  % Polarization
  SIMPOL=0;    % Polarization (0:TE, 1:TM)

  % Save data
  save_fig = 0; % Save the figures (0:no, 1:yes)
  save_res = 0; % Save the results in a mat file (0:no, 1:yes)

  % Applied arrayed waveguide profile
  appl_profile = 0;    % Applied a profile or use the typical Gaussian
      (0:Gaussian, 1:Profile)
  select_profile = 5;    % Select the profile(1:rect, 2:triang, 3:
      decaying exp, 4:trunc cos, 5:lorentzian, 6:ramp)
  select_ampmode = 1;    % Choose to cut the amplitudes or force the
      value (0:cut amplitudes, 1: force amplitudes)

  % Change the input/output positions
  input_d = 0;
```

```
output_d = 0;

% Losses
alfa_dB_cm = 0;   % Loss in dB/cm

% Spatial resolution
x0_f = -20e-6:0.1e-6:20e-6;   % First simulation input
xaw_f = -150e-6:0.1e-6:150e-6;  % First simulation array

Ax0 = 3;              % Real simulation input range in terms of
    Gaussian width
dx0 = 0.1e-6;         % Real simulation input spacing

Axaw = 5;           % Real simulation array range in terms of
    Gaussian width
dxaw = 0.1e-6;          % Real simulation array spacing

xos_Ax = 10e-6;         % Real simulation output range
Axos = 0.1e-6;          % Real simulation output spacing
```

fileprefix	Name of the AWG
select_inter	0: Use the sql database 1: Use the technology file
techfile	Technology file path (only if select_inter=1)
wvls	Start wavelength in microns
wvle	Final wavelength in microns
wvli	Wavelength increment in microns
SIMPOL	Simulation polarization (0: TE, 1: TM)
save_fig	Save the figures (0: No, 1: Yes)
save_res	Save the results in a mat file (0: No, 1: Yes)
appl_profile	Apply a profile in the AW or use the Gaussian (0: Gaussian, 1: Apply profile)
select_profile	1: Rect, 2: Triang, 3: Decaying exp, 4: Trunc cos, 5: Lorentzian, 6: Ramp
select_ampmode	Cut profile amplitudes or force value (0: Cut amplitudes, 1: Force amplitudes)
input_d	Change the input position
output_d	Change the output position
alfa_dB_cm	Introduce waveguide losses in dB/cm
x0_f	Input spatial grid vector in meters
xaw_f	Arrayed waveguide spatial grid vector in meters
Ax0	Input range in terms of Gaussian width
dx0	Input spacing in meters
Axaw	Array range in terms of Gaussian width
dxaw	Array spacing in meters
xos_Ax	Output range in meters
Axos	Output spacing in meters

C.3.4 Simulation output

Finally, it is only necessary to launch the file `simulador.m` in Matlab. The simulation percentage will be shown as in Fig. C.3-(a). Once the simulation has ended, a plot showing the AWG transfer function will be shown. It is possible to see an example in Fig. C.3-(b).

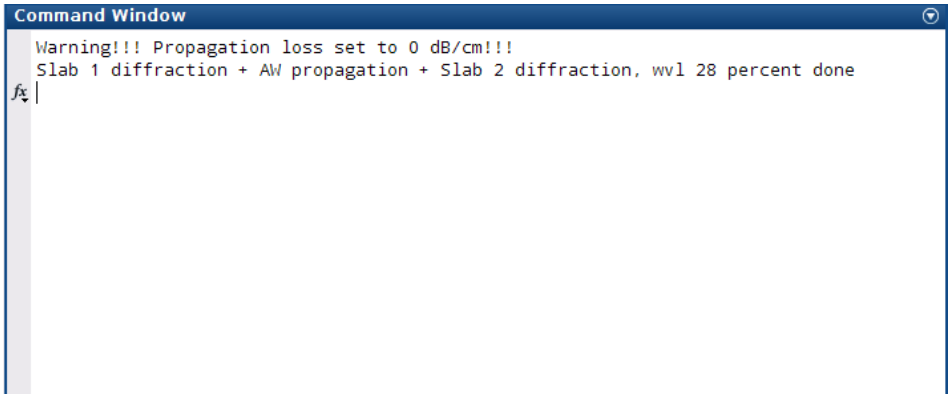

(a)

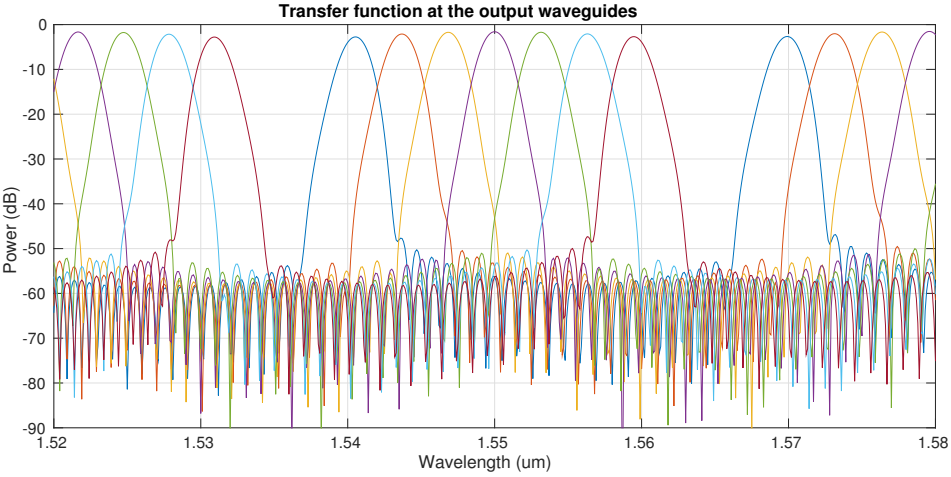

(b)

Figure C.3: AWG simulation in Matlab: (a) progress in the terminal window and (b) example of the result from one simulation.

Appendix D
AWG channel cross-talk definition

Cross-talk of AWGs is mainly attributed to the phase and amplitude errors introduced in the AWs [87]. These amplitude and/or phase fluctuations in the AW field profile cause an imperfect focused beam profile at the output plane, modifying the output spectrum profile and increasing the level of side-lobes. As a figure of merit of this cross-talk, several definitions have been used in the literature. However, the most common is the definition of what is called adjacent cross-talk. The adjacent cross-talk is calculated in a clear window (typically 3 dB from the peak maximum) as the highest transmission of one adjacent pass-band referenced to the lowest transmission of the selected channel pass-band.

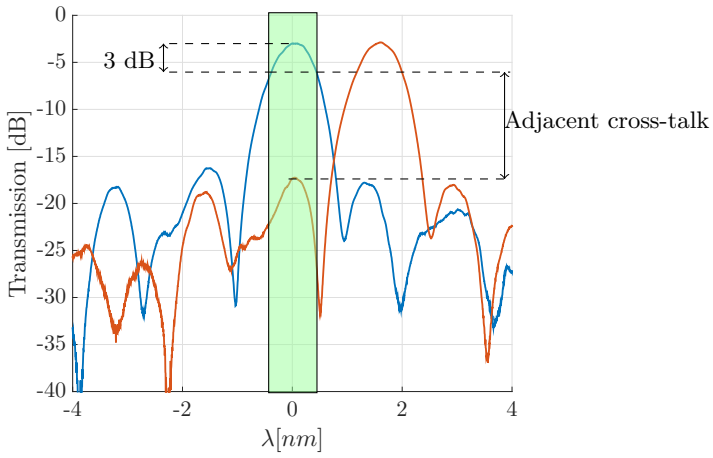

Figure D.1: Definition of the adjacent cross-talk. 3 dB clear window is represented in green color.

Appendix E
Optical frequency domain reflectometry (OFDR)

The key part in the AWG is the incremental length introduced at the arrayed waveguides. Thus, is extremely important to minimize the phase errors that will be introduced by fabrication. As the response of the AWG that can be measured with an optical spectrum analyzer is the convolution of the response of all the blocks composing the AWG, it is not possible to isolate and measure the phase errors introduced in the AWs. For this reason, the development of techniques to measure the phase errors due to fabrication would be very useful.

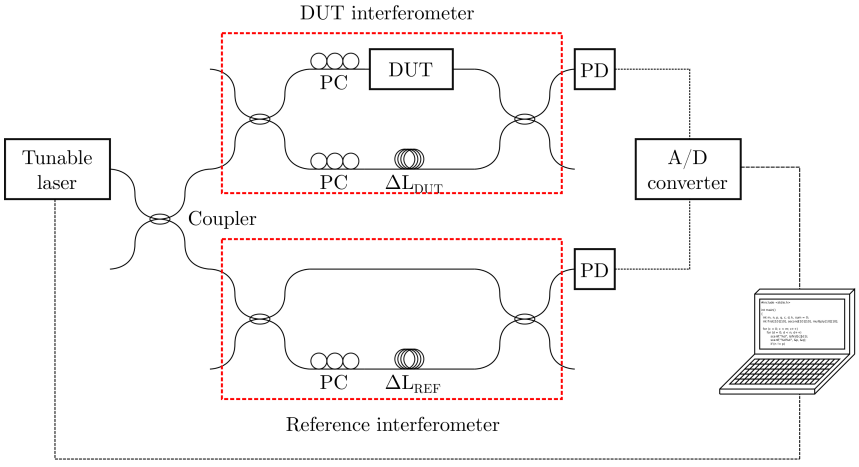

Figure E.1: Optical frequency domain reflectometry (OFDR) setup used for measurements.

In the literature, it is possible to find several examples using Fourier transform

spectroscopy and inserting the device with in an interferometer to measure the amplitude and phase in each AW independently [43, 108–110]. This technique is called optical frequency domain reflectometry (OFDR).

For completeness, the OFDR technique is summarized here. The schematic of the used OFDR setup is shown in Fig. E.1. In this setup, the light from a tunable source goes to a first coupler and it is splitted to the upper interferometer (DUT interferometer), where the device under test (DUT) will be inserted, and to the lower interferometer (reference interferometer) that will be used to correct the frequency errors of the tunable laser sweep. When measuring an AWG, the free spectral range (FSR) can be expressed as $FSR = c/\left(n_g \Delta l\right)$ where c is the speed of light in vacuum, n_g is the group index of the AWs and Δl is the incremental length between AWs. If the laser can sweep Δv_{LAS} more than one FSR, then $n_g \Delta l > c/\Delta v_{LAS}$, obtaining an optical length resolution $c/\Delta v_{LAS}$ shorter than the incremental length between AWs. Then, the fringes obtained from the interference of the DUT and the reference arm can be used to extract the measurement of the amplitude and phase in each AW independently. Later, the response of the two interferometers is converted to the electronic domain using two photodetectors, and then recorded in the computer using an analog to digital converter. Finally, it is only necessary to perform an inverse Fourier transform to obtain the response (amplitude and phase) in each AW independently.

Appendix F
List of publications

F.1 SCI Journal papers

1. B. Gargallo and P. Muñoz, "Full field model for interleave-chirped arrayed waveguide gratings," *Optics Express*, vol. 21, no. 6, pp. 6928–6942, 2013.

2. A. Crespo-Poveda, R. Hey, K. Biermann, A. Tahraoui, P. Santos, B. Gargallo, P. Muñoz, A. Cantarero, and M.M. de Lima, "Synchronized photonic modulators driven by surface acoustic waves," *Optics Express*, vol. 21, no. 18, pp. 21669–21676, 2013.

3. B. Gargallo, P. Muñoz, R. Baños, A.L. Giesecke, J. Bolten, T. Wahlbrink, and H. Kleinjans, "Reflective arrayed waveguide gratings based on Sagnac loop reflectors with custom spectral response," *Optics Express*, vol. 22, no. 12, pp. 14348–14362, 2014.

4. J.D. Doménech, J. Fandiño, B. Gargallo, and P. Muñoz, "Arbitrary coupling ratio multimode interference couplers in Silicon-on-Insulator," *Journal of Lightwave Technology*, vol. 32, no. 14, pp. 2536–2543, 2014.

5. A. Crespo-Poveda, A. Hernández-Mínguez, B. Gargallo, K. Biermann, A. Tahraoui, P.V. Santos, P. Muñoz, A. Cantarero, and M.M. de Lima, "Acoustically driven arrayed waveguide grating," *Optics Express*, vol. 23, no. 16, pp. 21213–21231, 2015.

6. B. Gargallo, Y. Jiao, P. Muñoz, J. van der Tol, and X. Leijtens, "Simulation and design of arrayed waveguide gratings for InP membranes using an efficient numerical method and improved shallow to deep transitions," *Optical Quantum Electronics*, vol. 48, no. 7, pp. 1–11, 2016.

F.2 Conference papers

1. B. Gargallo and P. Muñoz, "Theoretical model of an interleave-chirped arrayed waveguide grating (IC-AWG)," in *Proc. SPIE 8767, Integrated Photonics: Materials, Devices, and Applications II*, paper 87670S, Grenoble, France, 2013.

2. B. Gargallo and P. Muñoz, "Interleave-chirped arrayed waveguide grating theoretical model and design procedure," in *VIII Reunión Española de Optoelectrónica (OPTOEL)*, Alcalá de Henares, Madrid, 2013.

3. A. Crespo-Poveda, B. Gargallo, I. Artundo, J.D. Doménech, P. Muñoz, R. Hey, K. Biermann, A. Tahraoui, P.V. Santos, A. Cantarero, and M.M. de Lima, "Photonic Mach-Zehnder modulators driven by surface acoustic waves in AlGaAs technology," in *Proc. SPIE 8989, Smart Photonic and Optoelectronic Integrated Circuits XVI*, paper 898905, San Francisco, California, United States, 2014.

4. J.D. Doménech, J.S. Fandiño, B. Gargallo, and P. Muñoz, "Arbitrary coupling ratio multimode interference couplers in Silicon-on-Insulator," in *Proceedings of the 17th European Conference on Integrated Optics (ECIO)*, Nice, France, 2014.

5. A. Crespo-Poveda, K. Biermann, A. Tahraoui, P. Santos, B. Gargallo, P. Muñoz, A. Cantarero, and M.M. de Lima, "Integrated Photonic Devices Driven by Surface Acoustic Waves," in *Proceedings of the 17th European Conference on Integrated Optics (ECIO)*, Nice, France, 2014.

6. B. Gargallo and P. Muñoz, "Interleave-chirp arrayed waveguide grating on InP generic technology," in *Proceedings of the 17th European Conference on Integrated Optics (ECIO)*, Nice, France, 2014.

7. B. Gargallo, P. Muñoz, R. Baños, A.L. Giesecke, J. Bolten, T. Wahlbrink, and H. Kleinjans, "Reflective Arrayed Waveguide Grating with Sagnac Loop Reflectors in Silicon-on-Insulator with Gaussian Pass-band," in *Proceedings of the 17th European Conference on Integrated Optics (ECIO)*, Nice, France, 2014.

8. B. Gargallo, P. Muñoz, R. Baños, A.L. Giesecke, J. Bolten, T. Wahlbrink, and H. Kleinjans, "Silicon-on-insulator reflective arrayed waveguide grating with sagnac loop reflectors," in *Proceedings of the 40th European Conference on Optical Communication (ECOC)*, Cannes, France, 2014.

9. B. Gargallo, P. Muñoz, and R. Baños, "Reflective Arrayed Waveguide Grating in Silicon-on-Insulator with flattened spectral response," in *Proceedings of the 19th Annual Symposium of the IEEE Photonics Benelux Chapter*, Enschede, The Netherlands, 2014.

10. B. Gargallo, Y. Jiao, P. Muñoz, J. van der Tol, and X. Leijtens, "Accurate and efficient arrayed waveguide grating simulations for InP membranes," in *Optical wave and waveguide theory and numerical modelling workshop (OWTNM)*, London, United Kingdom, 2015.

11. P. Muñoz, B. Gargallo, G. Micó, D. Pastor, and A. Ortega-Moñux, "Reconfigurable integrated optics spectrometer," in *Photonics North 2015*, Ottawa, Canada, 2015.

12. B. Gargallo, J.D. Doménech, R. Baños, D. Pastor, C. Domínguez, and P. Muñoz, "Design of Arrayed Waveguide Gratings in Silicon Nitride," in *Proceedings of the 20th Annual Symposium of the IEEE Photonics Benelux Chapter*, Brussels, Belgium, 2015.

13. P. Muñoz, J.D. Doménech, J.S. Fandiño, R. Baños, and B. Gargallo, "Advanced Building Blocks in Thick Silicon on Insulator Technology: Echelle Grating Multiplexers and Reflective Multimode Interference Couplers," in *Proceedings of the 36th Progress in Electromagnetics Research Symposium (PIERS), Prague, Czech Republic, 2015.*

14. L.A. Bru, B. Gargallo, R. Baños, D. Pastor, J.D. Doménech, A.M. Sánchez, R. Mas, E. Pardo, P. Muñoz, "Optical frequency domain reflectometry applied to photonic integrated circuits," in *Proceedings of the 18th European Conference on Integrated Optics (ECIO)*, Warsaw, Poland, 2016.

15. J.D. Doménech, I. Artundo, B. Gargallo, R. Baños, P. Muñoz, and C. Domínguez, "Open access to low cost photonic integrated circuits prototyping in a generic Silicon Nitride foundry," in *V Conferencia Española de Nanofotónica (CEN)*, Valencia, 2016.

F.3 Papers in other journals

1. J.D. Doménech, J.S. Fandiño, B. Gargallo, R. Baños, and P. Muñoz, "Silicon opto-electronic wavelength tracker based on an asymmetric 2x3 Mach-Zehnder Interferometer," *Waves*, vol. 6, no. 1, pp. 29–34, 2014.

F.4 Patents

1. B. Gargallo, P. Muñoz, J. Capmany, and J.D. Doménech, "Espectrómetro óptico integrado en miniatura," OEPM P201331320 / ES2533610 - PCT/ES2014/070611, 2013.

2. B. Gargallo, P. Muñoz, J. Capmany, and J.S. Fandiño, "Dispositivo AWG reflectante con respuesta espectral configurable implementado con reflectores de Sagnac," OEPM P201331792 / ES2540378 - PCT/ES2014/070782, 2013.

3. B. Gargallo, P. Muñoz, D. Pastor, and G. Micó, "Integrated Optics Sensing Spectrometer (IOSS)," ref. R-17050-2014, 2014. Spanish patent being filed at the time of writing this thesis.

F.5 Awards

1. Second prize in the "VALENCIA IDEA 2013" contest, Information and communications technology category, received from the Ayuntamiento de Valencia, October 17, 2013.

Bibliography

[1] ePIXnet Steering Committee *et al.*, "Towards a foundry model in micro-and nano-photonics: a vision for Europe," 2007.

[2] P. Muñoz, J. D. Domenech, I. Artundo, J. H. den Besten, and J. Capmany, "Evolution of fabless generic photonic integration," in *2013 15th International Conference on Transparent Optical Networks (ICTON)*, 2013.

[3] I. P. Kaminow, "Optical integrated circuits: a personal perspective," *Journal of Lightwave Technology*, vol. 26, no. 9, pp. 994–1004, 2008.

[4] G. Treyz, "Silicon mach-zehnder waveguide interferometers operating at 1.3 μm," *Electronics Letters*, vol. 27, no. 2, pp. 118–120, 1991.

[5] J. Capmany, P. Muñoz, J. Domenech, and M. Muriel, "Apodized coupled resonator waveguides," *Optics express*, vol. 15, no. 16, pp. 10196–10206, 2007.

[6] W. Bogaerts, S. K. Selvaraja, P. Dumon, J. Brouckaert, K. De Vos, D. Van Thourhout, and R. Baets, "Silicon-on-insulator spectral filters fabricated with cmos technology," *IEEE journal of selected topics in quantum electronics*, vol. 16, no. 1, pp. 33–44, 2010.

[7] M. K. Smit and C. Van Dam, "Phasar-based wdm-devices: Principles, design and applications," *IEEE Journal of Selected Topics in Quantum Electronics*, vol. 2, no. 2, pp. 236–250, 1996.

[8] H. Takahashi, K. Oda, H. Toba, and Y. Inoue, "Transmission characteristics of arrayed waveguide n× n wavelength multiplexer," *Lightwave Technology, Journal of*, vol. 13, no. 3, pp. 447–455, 1995.

[9] P. Cheben, J. Schmid, A. Delâge, A. Densmore, S. Janz, B. Lamontagne, J. Lapointe, E. Post, P. Waldron, and D.-X. Xu, "A high-resolution silicon-on-insulator arrayed waveguide grating microspectrometer with submicrometer aperture waveguides," *Optics express*, vol. 15, no. 5, pp. 2299–2306, 2007.

[10] N. A. Yebo, W. Bogaerts, Z. Hens, and R. Baets, "On-chip arrayed waveguide grating interrogated silicon-on-insulator microring resonator-based gas sensor," *Photonics Technology Letters, IEEE*, vol. 23, no. 20, pp. 1505–1507, 2011.

[11] V. D. Nguyen, B. I. Akca, K. Wörhoff, R. M. De Ridder, M. Pollnau, T. G. van Leeuwen, and J. Kalkman, "Spectral domain optical coherence tomography imaging with an integrated optics spectrometer," *Optics letters*, vol. 36, no. 7, pp. 1293–1295, 2011.

[12] N. Ismail, L.-P. Choo-Smith, K. Wörhoff, A. Driessen, A. Baclig, P. Caspers, G. Puppels, R. De Ridder, and M. Pollnau, "Raman spectroscopy with an integrated arrayed-waveguide grating," *Optics letters*, vol. 36, no. 23, pp. 4629–4631, 2011.

[13] E. L. Wooten, K. M. Kissa, A. Yi-Yan, E. J. Murphy, D. A. Lafaw, P. F. Hallemeier, D. Maack, D. V. Attanasio, D. J. Fritz, G. J. McBrien, *et al.*, "A review of lithium niobate modulators for fiber-optic communications systems," *Selected Topics in Quantum Electronics, IEEE Journal of*, vol. 6, no. 1, pp. 69–82, 2000.

[14] Y. Inoue, A. Himeno, K. Moriwaki, and M. Kawachi, "Silica-based arrayed-waveguide grating circuit as optical splitter/router," *Electronics Letters*, vol. 31, no. 9, pp. 726–727, 1995.

[15] C. R. Doerr, L. Zhang, and P. J. Winzer, "Monolithic inp multiwavelength coherent receiver using a chirped arrayed waveguide grating," *Journal of Lightwave Technology*, vol. 29, no. 4, pp. 536–541, 2011.

[16] D. Dai, Z. Wang, J. F. Bauters, M.-C. Tien, M. J. Heck, D. J. Blumenthal, and J. E. Bowers, "Low-loss si3n4 arrayed-waveguide grating (de) multiplexer using nano-core optical waveguides," *Optics express*, vol. 19, no. 15, pp. 14130–14136, 2011.

[17] D. Feng, W. Qian, H. Liang, C.-C. Kung, J. Fong, B. J. Luff, and M. Asghari, "Fabrication insensitive echelle grating in silicon-on-insulator platform," *Photonics Technology Letters, IEEE*, vol. 23, no. 5, pp. 284–286, 2011.

[18] A. Malik, M. Muneeb, S. Pathak, Y. Shimura, J. Van Campenhout, R. Loo, and G. Roelkens, "Germanium-on-silicon mid-infrared arrayed waveguide grating multiplexers," *Photonics Technology Letters, IEEE*, vol. 25, no. 18, pp. 1805–1808, 2013.

[19] A. E.-J. Lim, J. Song, Q. Fang, C. Li, X. Tu, N. Duan, K. K. Chen, R. P.-C. Tern, and T.-Y. Liow, "Review of silicon photonics foundry efforts," *Selected Topics in Quantum Electronics, IEEE Journal of*, vol. 20, no. 4, pp. 405–416, 2014.

[20] M. Smit, X. Leijtens, H. Ambrosius, E. Bente, J. van der Tol, B. Smalbrugge, T. de Vries, E.-J. Geluk, J. Bolk, R. van Veldhoven, *et al.*, "An introduction to inp-based generic integration technology," *Semiconductor Science and Technology*, vol. 29, no. 8, p. 083001, 2014.

[21] A. Leinse, R. Heideman, M. Hoekman, F. Schreuder, F. Falke, C. Roeloffzen, L. Zhuang, M. Burla, D. Marpaung, D. Geuzebroek, *et al.*, "Triplex waveguide platform: low-loss technology over a wide wavelength range," in *SPIE Microtechnologies*, pp. 87670E–87670E, International Society for Optics and Photonics, 2013.

[22] D. Domenech, P. Muñoz, J. Cirera, C. Dominguez, and A. Sanchez, "Generic silicon nitride foundry development: Open access to low cost photonic integrated circuits prototyping," in *Proc. of the 9th Spanish Opto-electronics Conference (OPTOEL)*, 2015.

[23] "Europractice project." http://www.europractice-ic.com/.

[24] "Institute of Microelectronics (IME) of Singapore." https://www.a-star.edu.sg/ime/.

[25] "Joint European Platform for InP-based Photonic Integrated Components and Circuits (JePPIX)." http://www.jeppix.eu/.

[26] "VLC Photonics S.L.." http://www.vlcphotonics.com/.

[27] "VTT technical research centre of Finland Ltd.." http://www.vttresearch.com/.

[28] C. Brackett *et al.*, "Dense wavelength division multiplexing networks: Principles and applications," *Selected Areas in Communications, IEEE Journal on*, vol. 8, no. 6, pp. 948–964, 1990.

[29] C. Dragone, "An n×n optical multiplexer using a planar arrangement of two star couplers," *Photonics Technology Letters, IEEE*, vol. 3, no. 9, pp. 812–815, 1991.

[30] C. Dragone, C. Edwards, and R. Kistler, "Integrated optics n×n multiplexer on silicon," *Photonics Technology Letters, IEEE*, vol. 3, no. 10, pp. 896–899, 1991.

[31] M. Zirngibl, C. Dragone, and C. Joyner, "Demonstration of a 15×15 arrayed waveguide multiplexer on inp," *Photonics Technology Letters, IEEE*, vol. 4, no. 11, pp. 1250–1253, 1992.

[32] K. Okamoto, K. Moriwaki, and S. Suzuki, "Fabrication of 64× 64 arrayed-waveguide grating multiplexer on silicon," *Electronics Letters*, vol. 31, no. 3, pp. 184–186, 1995.

[33] M. R. Paiam and R. I. MacDonald, "Design of phased-array wavelength division multiplexers using multimode interference couplers," *Applied optics*, vol. 36, no. 21, pp. 5097–5108, 1997.

[34] P. Muñoz, D. Pastor, and J. Capmany, "Modeling and design of arrayed waveguide gratings," *Journal of lightwave technology*, vol. 20, no. 4, p. 661, 2002.

[35] J. W. Goodman, *Introduction to Fourier optics*. Roberts and Company Publishers, 2005.

[36] P. Muñoz, *Arrayed Waveguide Gratings: modeling, design and applications*. PhD thesis, Universidad Politècnica de València, 2003.

[37] F. Soares, K. Janiak, A. Seeger, R. Broeke, and N. Grote, "An inp-based generic integration technology platform," in *Photonics Conference (IPC), 2012 IEEE*, pp. 905–906, IEEE, 2012.

[38] P. Muñoz, D. Pastor, and J. Capmany, "Analysis and design of arrayed waveguide gratings with mmi couplers," *Optics express*, vol. 9, no. 7, pp. 328–338, 2001.

[39] J. den Besten, M. Dessens, C. Herben, X. Leijtens, F. Groen, M. Leys, and M. Smit, "Low-loss, compact, and polarization independent phasar demultiplexer fabricated by using a double-etch process," *IEEE Photonics Technology Letters, 14 (1)*, 2002.

[40] E. Kleijn, P. J. Williams, N. D. Whitbread, M. J. Wale, M. K. Smit, and X. J. Leijtens, "Sidelobes in the response of arrayed waveguide gratings caused by polarization rotation," *Optics express*, vol. 20, no. 20, pp. 22660–22668, 2012.

[41] L. Spiekman, M. Amersfoort, F. van Ham, A. Kuntze, J. Pedersen, P. Demeester, M. Smit, *et al.*, "Design and realization of polarization independent phased array wavelength demultiplexers using different array orders for te and tm," *Lightwave Technology, Journal of*, vol. 14, no. 6, pp. 991–995, 1996.

[42] K. Takada, H. Yamada, and Y. Inoue, "Optical low coherence method for characterizing silica-based arrayed-waveguide grating multiplexers," *Lightwave Technology, Journal of*, vol. 14, no. 7, pp. 1677–1689, 1996.

[43] K. Takada and K. Okamoto, "Frequency-domain measurement of phase error distribution in narrow-channel arrayed waveguide grating," *Electronics Letters*, vol. 36, no. 2, pp. 160–161, 2000.

[44] J. Soole, M. Amersfoort, H. Leblanc, N. Andreadakis, A. Rajhel, C. Caneau, R. Bhat, and M. Koza, "Use of multimode interference couplers to broaden the passband of dispersive integrated wdm filters," in *Integrated Photonics Research*, p. IMC4, Optical Society of America, 1996.

[45] J. Bolten, T. Wahlbrink, N. Koo, H. Kurz, S. Stammberger, U. Hofmann, and N. Ünal, "Improved cd control and line edge roughness in e-beam lithography through combining proximity effect correction with gray scale techniques," *Microelectronic Engineering*, vol. 87, no. 5, pp. 1041–1043, 2010.

[46] S. Pathak, D. Van Thourhout, and W. Bogaerts, "Design trade-offs for silicon-on-insulator-based awgs for (de) multiplexer applications," *Optics letters*, vol. 38, no. 16, pp. 2961–2964, 2013.

[47] W. Bogaerts, P. Dumon, D. Van Thourhout, D. Taillaert, P. Jaenen, J. Wouters, S. Beckx, V. Wiaux, and R. G. Baets, "Compact wavelength-selective functions in silicon-on-insulator photonic wires," *Selected Topics in Quantum Electronics, IEEE Journal of*, vol. 12, no. 6, pp. 1394–1401, 2006.

[48] P. Muñoz, D. Pastor, J. Capmany, D. Ortega, A. Pujol, and J. R. Bonar, "Awg model validation through measurement of fabricated devices," *Journal of lightwave technology*, vol. 22, no. 12, p. 2763, 2004.

[49] E. Kleijn, M. K. Smit, and X. J. Leijtens, "New analytical arrayed waveguide grating model," *Lightwave Technology, Journal of*, vol. 31, no. 20, pp. 3309–3314, 2013.

[50] "PhoeniX B.V, Solutions for micro and nano technologies." http://www.phoenixbv.com/.

[51] D. Taillaert, W. Bogaerts, P. Bienstman, T. F. Krauss, P. Van Daele, I. Moerman, S. Verstuyft, K. De Mesel, and R. Baets, "An out-of-plane grating coupler for efficient butt-coupling between compact planar waveguides and single-mode fibers," *Quantum Electronics, IEEE Journal of*, vol. 38, no. 7, pp. 949–955, 2002.

[52] F. Van Laere, T. Claes, J. Schrauwen, S. Scheerlinck, W. Bogaerts, D. Taillaert, L. O. Faolain, D. Van Thourhout, and R. Baets, "Compact focusing grating couplers for silicon-on-insulator integrated circuits," *Photonics Technology Letters, IEEE*, vol. 19, no. 23, pp. 1919–1921, 2007.

[53] D. Taillaert, H. Chong, P. Borel, L. H. Frandsen, R. M. De La Rue, R. Baets, *et al.*, "A compact two-dimensional grating coupler used as a polarization splitter," *Photonics Technology Letters, IEEE*, vol. 15, no. 9, pp. 1249–1251, 2003.

[54] H. Takahashi, I. Nishi, and Y. Hibino, "10 ghz spacing optical frequency division multiplexer based on arrayed-waveguide grating," *Electronics Letters*, vol. 28, no. 4, pp. 380–382, 1992.

[55] G. B. Beelen and H. F. Bulthuis, "Arrayed waveguide grating with reduced channel passband asymmetry," Feb. 17 2009. US Patent 7,492,991.

[56] A. Sakai, T. Fukazawa, and T. Baba, "Estimation of polarization crosstalk at a micro-bend in si-photonic wire waveguide," *Journal of lightwave technology*, vol. 22, no. 2, p. 520, 2004.

[57] S. Pathak, M. Vanslembrouck, P. Dumon, D. Van Thourhout, P. Verheyen, G. Lepage, P. Absil, and W. Bogaerts, "Effect of mask discretization on performance of silicon arrayed waveguide gratings," *Photonics Technology Letters, IEEE*, vol. 26, no. 7, pp. 718–721, 2014.

[58] M. Nakazawa, K. Kikuchi, and T. Miyazaki, *High Spectral Density Optical Communication Technologies*, vol. 6. Springer Science & Business Media, 2010.

[59] R. Nagarajan, M. Kato, D. Lambert, P. Evans, S. Corzine, V. Lal, J. Rahn, A. Nilsson, M. Fisher, M. Kuntz, *et al.*, "Terabit/s class inp photonic integrated circuits," *Semiconductor Science and Technology*, vol. 27, no. 9, pp. 94003–94007, 2012.

[60] C. Xie, P. J. Winzer, G. Raybon, A. H. Gnauck, B. Zhu, T. Geisler, and B. Edvold, "Colorless coherent receiver using 3x3 coupler hybrids and single-ended detection," *Optics express*, vol. 20, no. 2, pp. 1164–1171, 2012.

[61] M. Morsy-Osman, M. Chagnon, X. Xu, Q. Zhuge, M. Poulin, Y. Painchaud, M. Pelletier, C. Paquet, and D. V. Plant, "Analytical and experimental performance evaluation of an integrated si-photonic balanced coherent receiver in a colorless scenario," *Optics express*, vol. 22, no. 5, pp. 5693–5730, 2014.

[62] Y. Wan and R. Hui, "Design of wdm cross connect based on interleaved awg (iawg) and a phase shifter array," *Journal of lightwave technology*, vol. 25, no. 6, pp. 1390–1400, 2007.

[63] E. Bente and M. Smit, "Ultrafast inp optical integrated circuits," in *Integrated Optoelectronic Devices 2006*, pp. 612419–612419, International Society for Optics and Photonics, 2006.

[64] B. Gargallo and P. Muñoz, "Full field model for interleave-chirped arrayed waveguide gratings," *Optics express*, vol. 21, no. 6, pp. 6928–6942, 2013.

[65] L. Zimmermann, K. Voigt, G. Winzer, K. Petermann, and C. M. Weinert, "C-band optical 90-hybrids based on silicon-on-insulator 4×4 waveguide couplers," *IEEE Photon. Technol. Lett*, vol. 21, no. 3, pp. 143–145, 2009.

[66] F. Morichetti, A. Melloni, and M. Martinelli, "Effects of polarization rotation in optical ring-resonator-based devices," *Journal of lightwave technology*, vol. 24, no. 1, p. 573, 2006.

[67] R. Kirchain and L. Kimerling, "A roadmap for nanophotonics," *Nature Photonics*, vol. 1, no. 6, pp. 303–305, 2007.

[68] E. Pennings, G.-D. Khoe, M. K. Smit, and T. Staring, "Integrated-optic versus microoptic devices for fiber-optic telecommunication systems: a comparison," *Selected Topics in Quantum Electronics, IEEE Journal of*, vol. 2, no. 2, pp. 151–164, 1996.

[69] R. J. Lycett, D. F. Gallagher, and V. J. Brulis, "Perfect chirped echelle grating wavelength multiplexor: design and optimization," *Photonics Journal, IEEE*, vol. 5, no. 2, pp. 2400123–2400123, 2013.

[70] E. Ryckeboer, A. Gassenq, M. Muneeb, N. Hattasan, S. Pathak, L. Cerutti, J. Rodriguez, E. Tournie, W. Bogaerts, R. Baets, *et al.*, "Silicon-on-insulator spectrometers with integrated gainassb photodiodes for wide-band spectroscopy from 1510 to 2300 nm," *Optics express*, vol. 21, no. 5, pp. 6101–6108, 2013.

[71] L. G. De Peralta, A. Bernussi, S. Frisbie, R. Gale, and H. Temkin, "Reflective arrayed waveguide grating multiplexer," *Photonics Technology Letters, IEEE*, vol. 15, no. 10, pp. 1398–1400, 2003.

[72] J. Soole, M. Amersfoort, H. LeBlanc, A. Rajhel, C. Caneau, C. Youtsey, and I. Adesida, "Compact polarisation independent inp reflective arrayed waveguide grating filter," *Electronics Letters*, vol. 32, no. 19, pp. 1769–1771, 1996.

[73] D. Dai, X. Fu, Y. Shi, and S. He, "Experimental demonstration of an ultracompact si-nanowire-based reflective arrayed-waveguide grating (de) multiplexer with photonic crystal reflectors," *Optics letters*, vol. 35, no. 15, pp. 2594–2596, 2010.

[74] L. G. De Peralta, A. Bernussi, V. Gorbounov, and H. Temkin, "Temperature-insensitive reflective arrayed-waveguide grating multiplexers," *Photonics Technology Letters, IEEE*, vol. 16, no. 3, pp. 831–833, 2004.

[75] K. Okamoto and K. Ishida, "Fabrication of silicon reflection-type arrayed-waveguide gratings with distributed bragg reflectors," *Optics letters*, vol. 38, no. 18, pp. 3530–3533, 2013.

[76] Y. Ikuma, M. Yasumoto, D. Miyamoto, J. Ito, and H. Tsuda, "Small helical reflective arrayed-waveguide grating with integrated loop mirrors," *ECOC 2007*, 2007.

[77] K. Okamoto and H. Yamada, "Arrayed-waveguide grating multiplexer with flat spectral response," *Optics letters*, vol. 20, no. 1, pp. 43–45, 1995.

[78] B. Saleh and M. Teich, *Fundamentals of Photonics*. Wiley Series in Pure and Applied Optics, Wiley, 2007.

[79] K. Jinguji, N. Takato, Y. Hida, T. Kitoh, and M. Kawachi, "Two-port optical wavelength circuits composed of cascaded mach-zehnder interferometers with point-symmetrical configurations," *Lightwave Technology, Journal of*, vol. 14, no. 10, pp. 2301–2310, 1996.

[80] L. B. Soldano and E. Pennings, "Optical multi-mode interference devices based on self-imaging: principles and applications," *Lightwave Technology, Journal of*, vol. 13, no. 4, pp. 615–627, 1995.

[81] M. Bachmann, P. Besse, and H. Melchior, "General self-imaging properties in nxn multimode interference couplers including phase relations," *Applied optics*, vol. 33, no. 18, pp. 3905–3911, 1994.

[82] P. Besse, E. Gini, M. Bachmann, H. Melchior, *et al.*, "New 2x2 and 1x3 multimode interference couplers with free selection of power splitting ratios," *Lightwave Technology, Journal of*, vol. 14, no. 10, pp. 2286–2293, 1996.

[83] J. Leuthold and C. H. Joyner, "Multimode interference couplers with tunable power splitting ratios," *Journal of lightwave technology*, vol. 19, no. 5, pp. 700–707, 2001.

[84] S.-H. Jeong and K. Morito, "Novel optical 90 ^{circ} hybrid consisting of a paired interference based 2x4 mmi coupler, a phase shifter and a 2x2 mmi coupler," *Journal of Lightwave Technology*, vol. 28, no. 9, pp. 1323–1331, 2010.

[85] K. Okamoto and A. Sugita, "Flat spectral response arrayed-waveguide grating multiplexer with parabolic waveguide horns," *Electronics letters*, vol. 32, no. 18, p. 1661, 1996.

[86] C. Doerr, M. Cappuzzo, E. Chen, A. Wong-Foy, L. Gomez, and L. Buhl, "Wideband arrayed waveguide grating with three low-loss maxima per passband," *IEEE photonics technology letters*, vol. 18, no. 21-24, pp. 2308–2310, 2006.

[87] K. Okamoto, *Fundamentals of optical waveguides*. Academic press, 2010.

[88] "Fourier transform pairs." http://www.thefouriertransform.com/pairs/fourier.php.

[89] G. A. Wurtz, R. Pollard, W. Hendren, G. Wiederrecht, D. Gosztola, V. Podolskiy, and A. V. Zayats, "Designed ultrafast optical nonlinearity in a plasmonic nanorod metamaterial enhanced by nonlocality," *Nature nanotechnology*, vol. 6, no. 2, pp. 107–111, 2011.

[90] R. Stabile, A. Rohit, and K. Williams, "Monolithically integrated 8× 8 space and wavelength selective cross-connect," *Lightwave Technology, Journal of*, vol. 32, no. 2, pp. 201–207, 2014.

[91] S. Nakamura, Y. Ueno, and K. Tajima, "Femtosecond switching with semiconductor-optical-amplifier-based symmetric mach–zehnder-type all-optical switch," *Applied Physics Letters*, vol. 78, no. 25, pp. 3929–3931, 2001.

[92] X. Li, H. Xu, X. Xiao, Z. Li, Y. Yu, and J. Yu, "Fast and efficient silicon thermo-optic switching based on reverse breakdown of pn junction," *Optics letters*, vol. 39, no. 4, pp. 751–753, 2014.

[93] C. Gorecki, F. Chollet, E. Bonnotte, and H. Kawakatsu, "Silicon-based integrated interferometer with phase modulation driven by surface acoustic waves," *Optics letters*, vol. 22, no. 23, pp. 1784–1786, 1997.

[94] M. de Lima Jr, M. Beck, R. Hey, and P. Santos, "Compact mach-zehnder acousto-optic modulator," *Applied physics letters*, vol. 89, no. 12, p. 121104, 2006.

[95] M. Beck, M. de Lima Jr, E. Wiebicke, W. Seidel, R. Hey, and P. Santos, "Acousto-optical multiple interference switches," *Applied Physics Letters*, vol. 91, no. 6, p. 061118, 2007.

[96] M. Beck, M. de Lima Jr, and P. Santos, "Acousto-optical multiple interference devices," *Journal of Applied Physics*, vol. 103, no. 1, p. 014505, 2008.

[97] A. Crespo-Poveda, R. Hey, K. Biermann, A. Tahraoui, P. Santos, B. Gargallo, P. Muñoz, A. Cantarero, and M. de Lima, "Synchronized photonic modulators driven by surface acoustic waves," *Optics express*, vol. 21, no. 18, pp. 21669–21676, 2013.

[98] P. V. Santos *et al.*, "Modulation of photonic structures by surface acoustic waves," *Reports on progress in physics*, vol. 68, no. 7, p. 1639, 2005.

[99] C.-L. Chen, *Foundations for guided-wave optics*. John Wiley & Sons, 2006.

[100] M. de Lima Jr, F. Alsina, W. Seidel, and P. Santos, "Focusing of surface-acoustic-wave fields on (100) gaas surfaces," *Journal of applied physics*, vol. 94, no. 12, pp. 7848–7855, 2003.

[101] MATLAB, *version 8.4.0 (R2014b)*. Natick, Massachusetts: The MathWorks Inc., 2014.

[102] J. W. Eaton, D. Bateman, S. Hauberg, and R. Wehbring, *GNU Octave version 3.8.1 manual: a high-level interactive language for numerical computations*. CreateSpace Independent Publishing Platform, 2014.

[103] R. Kitamura, L. Pilon, and M. Jonasz, "Optical constants of silica glass from extreme ultraviolet to far infrared at near room temperature," *Applied optics*, vol. 46, no. 33, pp. 8118–8133, 2007.

[104] M. Smit, *Integrated optics in silicon-based aluminum oxide*. PhD thesis, Technische Universiteit Delft, 1991.

[105] N. Ismail, F. Sun, G. Sengo, K. Wörhoff, A. Driessen, R. M. De Ridder, and M. Pollnau, "Improved arrayed-waveguide-grating layout avoiding systematic phase errors," *Optics express*, vol. 19, no. 9, pp. 8781–8794, 2011.

[106] H. Takahashi, S. Suzuki, K. Kato, and I. Nishi, "Arrayed-waveguide grating for wavelength division multi/demultiplexer with nanometre resolution," *Electronics letters*, vol. 26, no. 2, pp. 87–88, 1990.

[107] R. Adar, C. H. Henry, C. Dragone, R. C. Kistler, and M. A. Milbrodt, "Broad-band array multiplexers made with silica waveguides on silicon," *Lightwave Technology, Journal of*, vol. 11, no. 2, pp. 212–219, 1993.

[108] K. Takada and S.-i. Satoh, "Method for measuring the phase error distribution of a wideband arrayed waveguide grating in the frequency domain," *Optics letters*, vol. 31, no. 3, pp. 323–325, 2006.

[109] H. Yamada, H. Sanjoh, M. Kohtoku, K. Takada, and K. Okamoto, "Measurement of phase and amplitude error distributions in arrayed-waveguide grating multi/demultiplexers based on dispersive waveguide," *Journal of lightwave technology*, vol. 18, no. 9, p. 1309, 2000.

[110] B. Soller, D. Gifford, M. Wolfe, and M. Froggatt, "High resolution optical frequency domain reflectometry for characterization of components and assemblies," *Optics Express*, vol. 13, no. 2, pp. 666–674, 2005.